Effect of Strain in General and Localized Corrosion Behavior of Steels

A Dissertation
Presented to
The Academic Faculty

by

Gaoxiang Wu

In Partial Fulfillment
of the Requirements for the Degree
Doctor of Philosiphy in the
School of Materials Science and Engineering

Georgia Institute of Technology
May 2019

EFFECT OF STRAIN IN CORROSION BEHAVIORS OF STEELS

Approved by:

Dr. Preet M. Singh, Advisor
School of Materials Science and Engineering
Georgia Institute of Technology

Dr. Arun Gokhale
School of Materials Science and Engineering
Georgia Institute of Technology

Dr. Matthew McDowell
School of Materials Science and Engineering
Georgia Institute of Technology

Dr. Faisal Alamgir
School of Materials Science and Engineering
Georgia Institute of Technology

Dr. Thomas Fuller
School of Chemical and Biomolecular Engineering
Georgia Institute of Technology

Date Approved: January 31st, 2019

ACKNOWLEDGEMENTS

To my parents, who raised me up and supported me unconditionally: I owe it all to you.

My dearest advisor, Dr. Preet M. Singh: your patience never wore out during our countless discussion; your knowledge, kindness and professionalism established a perfect role model for me. It was lucky for me to start my undergraduate research and continued to finish my PhD study in your group. You helped me foster an incredible love and gain solid knowledge in corrosion and materials science in general. For that, I will be forever grateful. In addition, I would like to express my gratitude to my committee members, Dr. Arun Gokhale, Dr. Faisal Alamgir, Dr. Thomas Fuller, and Dr. Matthew McDowell for challenging me and pushing me to perfect my work.

I would like to thank my mentor Dr. Robert Sanders: thank you so much for your mentorship since my undergraduate junior year. You have been such an adorable and knowledgeable person that I can look up to.

A very special gratitude goes out to the funding support provided by the paper science and engineering (PSE) fellowship and the renewable bio-products institute (RBI) member companies.

With a special mention to my group members, Liang He, Kasey Hanson, Kevin Chan, and Mahmood Jamshad for their feedback and help. Our friendship will last beyond school.

Finally, last but by no means least, also to everyone in the corrosion lab and everyone who helped me throughout my graduate study. It was a great honor to work with all of you during last four years.

Thanks for all your encouragement!

TABLE OF CONTENTS

LIST OF TABLES

LIST OF FIGURES

SUMMARY

Metallic structures in various chemical-processing industries as well as in other structural applications have shown accelerated corrosion in areas with strain/deformation. During manufacturing, assembly and even during service, strain is inevitably introduced to many metallic materials. Although pertinent prior research has concentrated on the stress corrosion cracking (SCC) and corrosion fatigue, but the effect of strain on other modes of corrosion behavior in different material/environment systems is not very well understood.

This present study focused on the influence of different forms of strain on general and localized corrosion behavior of steels. Both elastic and plastic strain were found to shift the open circuit potential (OCP) of carbon steel A569 to a more negative value in an acidic environment. Thermodynamically, this shift indicates a stronger tendency of general corrosion due to the presence of strain. Consequentially, both deformed tensile A569 specimens and cold-rolled A569 specimens exhibited an accelerated corrosion rate to different degrees. Influence and mechanism of deformation-influenced pitting corrosion was studied using austenitic stainless steel (SS) 304. Tensile strain, both elastic and plastic was found to promote pitting corrosion of stainless steel (SS) 304 in a chloride-containing aqueous environment. It was found that elastic strain promoted the pitting corrosion of SS304, by stabilizing the pit-growth process regardless of different surface treatments. This negative effect reached a limit at the yield stress of SS304. Increasing the tensile strain into the plastic range did not lead to further damage in the pitting potential of SS304. The plastically deformed SS304 experienced different extent of recovery in the pitting potential after the applied stress was released. This recovery ceased at a plastic stain level of ~9%. It was commonly observed that the localized areas associated with surface defects such as slip-lines were more prone to pitting attacks. Accumulating such surface defects were believed to continuously lower the pitting potential of SS304 until the maximum deterioration was reached at ~9% residual plastic strain. After re-polishing, the pitting potential of SS304 was fully recovered for both previously deformed tensile specimens and cold-rolled specimens. It indicated that pitting corrosion phenomena were extremely dependent on the surface condition. This also made it possible to alleviate the strain-facilitated pitting corrosion by manipulating the surface-finish of SS304. Apart from the negative effects of strain on general corrosion and pitting corrosion, strain was also found to improve the kinetics of re-formation of the passive films under stable-repassivation conditions, as studied by utilizing an electrochemical film-repassivation technique.

This thesis focused on developing a fundamental understanding of the role of deformation (elastic as well as plastic deformation) on active corrosion as well as localized corrosion behavior of metallic alloys, especially carbon steel and stainless steels. It has advanced the knowledge of effect of strain on corrosion behaviors of steel systems, thereby will help in preventing strain induced accelerated corrosion or failures in related areas.

CHAPTER 1. INTRODUCTION

1.1 Motivation

The main purpose of this project was to systematically investigate the role of elastic and plastic strain on corrosion mode and extent in carbon steels and stainless steels. Practical motivation for this study was based on a few deformation-related failure investigations of equipment made out of carbon steels and stainless steels in the pulp and paper mills. Preliminary investigations indicated that the deformation caused corrosion to accelerate in these failures, for example in heat-exchanger tubes where the stainless-steel tube area that had undergone a tube-expansion operation showed more severe corrosion than the unstrained tube areas. Fig. 1-1 showed a carbon steel plate serving in a black-liquor environment underwent accelerated active corrosion in the breaking strips where prior bending and shearing occurred. The resultant residual strain was thereby suspected to cause a much higher corrosion rate in these strip areas. There are many examples like this in chemical process plants and other structural applications, which makes this investigation very important in terms of our understanding of the role that elastic and plastic strain plays in the corrosion behavior of structural alloys.

Figure 1-1. Accelerated corrosion in the breaking strips where strain is concentrated.

Since deformation usually is associated with other significant changes in the microstructure, it is difficult to isolate the pure effect of strain on the associated chemical reactions. For an alloy/environment system where a protective passive film forms at the surface, the effect of strain can be very different than that for a system where the alloys are in their active corrosion state. Stainless steels contain at least 12% Cr, which helps it to form a passive Cr-rich oxide film on the surface. However, strain may also destabilize the passive film of various alloys in caustic environments, therefore causing early localized corrosion, such as pitting corrosion [1-3]. Stainless steels (SS) are known for their excellent corrosion resistance and mechanical properties in many industrial and structural applications such as infrastructures, transportation, chemical storage, and oil refineries [1]. A unique class of stainless steels is duplex stainless (DSS). It possesses almost equal amounts of ferrite grains and austenite grains. This gives rise to superior mechanical and corrosion properties to both ferritic stainless steel and austenitic stainless steel – higher toughness and weldability than ferritic stainless steel, and more resistant in stress corrosion cracking (SCC) and pitting corrosion than austenitic stainless steel [1]. The heterogeneous microstructure makes plastic deformation inherent in all DSS grades, because the ferrite and the austenite phases possess different crystal structures, chemical compositions and coefficient of thermal expansion. Upon various manufacturing processes, such as quenching and aging the differences between the two phases lead to the ferrite phase under compressive stresses, while the austenite phase is in tension. The knowledge developed on strain-influenced corrosion reactions can help gain useful insights on the interaction between the strain ferrite and austenite during different corrosion processes.

This study advances our knowledge of strain-associated corrosion/repassivation behavior of various metallic systems and can potentially help prevent similar failures in related areas. Furthermore, it will also establish a criterion for materials selection when building metallic structures. The total annual corrosion costs in the USA was about $276 billion in 2005-approximately 3.1% of the nation’s Gross Domestic Product (GDP) [4], therefore significant corrosion related cost for these metallic structures can be reduced from the understanding of the effect of strain on corrosion and developing mitigation strategies.

1.2 Objectives

The main objective of this proposed work is to gain a fundamental understanding of the effect of strain on different types of corrosion in selected alloy systems. This study concentrates on the dissolution reactions and does not include stress corrosion cracking. The specific technical objectives are:

- To assess the deformation-accelerated general corrosion (under activation control), especially in the alloy systems where passive film does not form or is not very stable, such as carbon steels in acidic environments;
- To establish the role of deformation on stability of passive film and repassivation kinetics under in-situ/ex-situ loading conditions;
- To study the characteristics of passive film in the presence of different types/extents of strain;
- To develop an electrochemical method to substitute the traditional scratch test in order to investigate the strain-influenced repassivation kinetics;
- To understand the interplay between the global strain and the localized strain during different corrosion processes in stainless steels.

Results from present study will help us assess the effect of strain/deformation on general corrosion, pitting corrosion and pit-repassivation kinetics of steels. Upon the development of a new method to study repassivation kinetics, the influence of strain on stable repassivation can hence be evaluated. This work will provide quantitative and qualitative analysis on strain-influenced corrosion-related behavior.

1.3 Organization of Upcoming Chapters

In the following chapters, a general review is given on activation-controlled general corrosion and localized corrosion in Chapter 2. The experimental procedures and materials used in this study are described in Chapter 3. The influence of strain on general corrosion is investigated in Chapter 4. In chapter 5, the role of strain on stable repassivation is explored and discussed. Chapter 6 presents the effect of elastic tensile stresses on pitting corrosion of stainless steel 304, and the associated mechanism are also explained in this chapter. Correspondingly, the influence of plastic deformation, including cold-rolling and plastic tensile stresses on pitting corrosion of SS304 is discussed in Chapter 7. A general summary and some recommendations for future research are described in Chapter 8.

CHAPTER 2. BACKGROUND

2.1 Activation-controlled General Corrosion

In chemical physics and physical chemistry, many branches were subdivided according to the nature and stimulants of reactions. A specific term referred as “mechanicochemistry” was classified to describe the effect of mechanical energy on chemical reactions. Corrosion is a special group of chemical reactions which deals with different types of metal oxidation reactions under the scope of materials degradation. The correlation of mechanical energy and corrosion is investigated and bridged in this thesis.

General corrosion is a corrosion reaction that generally takes place more or less uniformly on the surface of alloys’ in active state. It is sometimes referred as active dissolution or uniform corrosion. In the active state, the oxidation reaction is predominately driven by thermodynamics. Therefore, general corrosion is activation-controlled. Thermodynamically, one can expect that the mechanical energy provides an additional driving force to promote potential corrosion reactions. This is a fundamental guidance to help understand the mechnicochemical phenomena to be discussed within this study in both active state and passive state.

Electrochemical potential is a measure of metal’s oxidation tendency in corrosion. Different metals possess their inherent oxidation potentials, which is standardized and ranked in the electromotive force series (EMF series). However, pure metals are only used in very specialized areas, and alloys gains most industrial applications. Therefore, the electrochemical potential of a specific alloy is a function of its alloying elements, microstructure, surface treatment, and the environment. For example, magnesium (Mg) is often added in aluminum alloys (AAs), and Mg-enrichment on AA surfaces is commonly seen due to certain heat treatment or surface treatment [5]. Mg, being an active element according to the EMF series can preferentially be oxidized, causing a cathodic shift (or lower values) of electrochemical potential when blended as an alloying element. This can result in problematic corrosion hazards like galvanic corrosion or preferential dissolution of aluminum alloys [6, 7].

Traditionally the general corrosion can be combated by cathodic protection which suppresses the anodic half-cell reaction and control the general corrosion as indicated in the yellow cathodic protection regime in Fig. 2-1. There are two different ways to provide the cathodic protection to a structure; one by lowering the electrochemical potential of structural alloy by applied or impressed current; second method is to attach a more active metal or alloy which will preferentially corrode and polarize the structural alloy to a more negative potential which further suppresses the anodic reaction on the structural alloy. Thus, the active metal attached to the structural alloy is also called a sacrificial anode. These techniques are mostly applied in the areas where environments are very aggressive and economical materials like carbon steels are used. One risk of applying cathodic protection is the potential of charging hydrogen into the material being protected, and hydrogen retention can cause hydrogen embrittlement and hydrogen-induced stress cracking in many alloys [8-12].

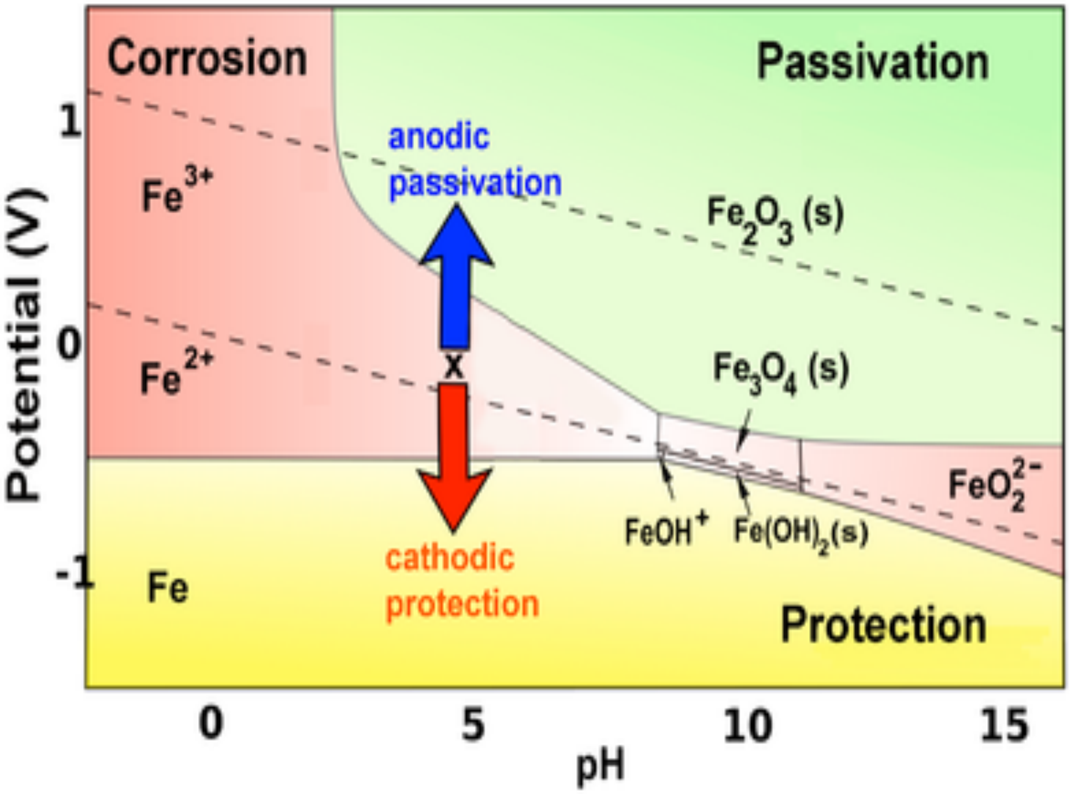

Figure 2-1. Fe Pourbaix Diagram.

2.1.1 Thermodynamics of Activation-Controlled General Corrosion

In thermodynamics, U is known as the internal energy, and differentiating U gives

$$dU = dQ - dW \qquad (2.1).$$

where Q is the amount of heat introduced to the system, W is work done by the system to the material system. When deformation is applied to the materials, additional strain energy is stored in the material as another source of the internal energy [13]. To simplify the derivation here, it is given a new term as "dW_{strain}". Eq. 1 can now be re-written as

$$dU = dQ - dW + dW_{strain}$$

$$= dQ - PdV + dW_{strain} \qquad (2.2).$$

G is known as the Gibbs free energy in thermodynamics, P is the atmosphere pressure and V is the volume of the material. All the deformation discussed in this thesis was performed in aerated conditions. Since the Gibbs free energy is defined as

$$G = H - TS = U + PV - TS \qquad (2.3),$$

where H is enthalpy, T is temperature, and S is the entropy. Differentiating G gives

$$dG = dQ + VdP - SdT - TdS + dW_{strain} \qquad (2.4).$$

Since the strain energy was all lumped into the dW_{strain} term, we can treat V as a constant. The entropy change during deformation processes, either elastic or plastic can also be neglected [13]. Assuming the process is reversible, dQ = TdS. Eq. 4 can be re-written as

$$dG = dW_{strain} \qquad (2.5).$$

It is also possible to have heat transfer involved at a later stage of work hardening. That could reduce strain energy stored in the material system, but here we only focus on the scenarios where elastic deformation increases the stored strain energy. Therefore, in such processes of metal deformation, if environment does a positive work to the material, dW_{strain} as a stored strain energy in metals,

$$dG_{metal} = \quad dW_{strain} \quad > 0 \qquad (2.6).$$

To put it in simple terms, strained metals possesses an elevated Gibbs free energy level. According to the Nernst equation,

$$\Delta G = -nFE \qquad (2.7),$$

where F is faraday’s number, and E is the reduction potential of reaction (2.1). This equation means that an electrochemical reaction which releases more energy possesses a lower potential. In other words, a strained metal can be more electrochemically reactive than the same metal without strain. Metallic materials and environmental parameters together determine whether the metal will be in the active or passive state. A very important criterion for activation-controlled general corrosion is pH. Pourbaix diagram demonstrated in Fig. 2-1, using Fe as an example, is used to determine the active/passive zone that the material falls into. Pourbaix diagram provides an important thermodynamics reference of stable phases in aqueous environments, although it gives no indication about the kinetics of the reaction.

A metallic material in a higher state of Gibbs free energy can be expected to drive a strong corrosion reaction. However, there are different forms of deformation/strain. Energy contribution of some representative deformation types are discussed next.

2.1.1.1 *Contribution of Elastic Stresses as Strain Energy*

In the elastic regime, stress, σ (either compression or tension) is proportional to strain, ε. It can be described using Hooke’s Law. For the simplified case of one-dimension:

$$\sigma_1 = E^*\varepsilon_1 \quad (2.8),$$

where E is the elastic modulus, also called the Young's modulus. Therefore, the resultant strain energy W_{strain} is given as

$$W_1 = \sigma_1^2 / 2E \quad (2.9).$$

Assuming there is multiple stresses σ_1, σ_2, σ_3 acting upon the solid metal, the strain can be modified as

$$\varepsilon_1 = [\sigma_1 - v (\sigma_2 + \sigma_3)] / E \quad (2.10),$$

$$\varepsilon_2 = [\sigma_2 - v (\sigma_1 + \sigma_3)] / E \quad (2.11),$$

$$\varepsilon_3 = [\sigma_2 - v (\sigma_1 + \sigma_2)] / E \quad (2.12),$$

where v is the Poisson's ratio. The total strain energy, W_{strain} [13] is

$$W_{strain} = W_1 + W_2 + W_3 \quad (2.13),$$

$$W_{strain} = \frac{1}{2E} [(\sigma_1^2 + \sigma_2^2 + \sigma_3^2) - 2v (\sigma_1 \sigma_2 + \sigma_2 \sigma_3 + \sigma_1 \sigma_3)] \quad (2.14).$$

The stored strain energy W_{strain} can be broken down into two components: one is resulted from the change of the shape of the solid; the other one is a consequence of the volume change [13]. As elucidated above that elastic stresses can be quantitatively calculated as strain energy, and this additional strain energy applied to the material can be transformed to a decrease of electrochemical potential through the Nernst equation. Hence, the influence of elastic strain can be quantitatively assessed.

2.1.1.2 *Contribution of Structural Defects to Strain Energy*

Structural defects or local plasticity like dislocations and twining can give rise to elastic strain stored at the atomic level. Structural defects are inevitably introduced into materials systems when plastic deformation occurs. The energy of formation for an edge dislocation is estimated to be ~8 eV [13], so any structural defect can be expected to increase the internal energy of a solid material system. However, no universal rule can apply to all materials when estimating this “atomic level” elastic strain energy due to plastic deformation, because different materials may have different deformation mechanism involving the interaction among structural defects. Dislocations as a common type of structural defects is the fundamental basis for many other structural evolutions. It introduces micro-strain in its vicinity and macro-strain to the material matrix. The evolution of dislocations during plastic deformation is elaborated here to depict a simplified picture of the plastic deformation process.

Plastic deformation causes residual stresses by inducing expansion or contraction of interplanar spacing. The residual stresses can be measured using X-ray diffraction (XRD). It is termed as macro-strain or macro-stress and can be understood as a form of global elastic strain energy. However, the stress field around a structural defect like a dislocation causes micro-strain. It represents a localized strain energy unlike the global strain energy that macro-strain possesses. These two elastic strain energy sources comprise the entire plastic deformation energy. Gutman [13] deduced that the difference of the chemical potential of a solid crystal $\Delta\mu$ as a function of dislocation density,

$$\Delta\mu = RT{*}ln\,\frac{N}{N_0}\,,$$

where R is the gas constant, N is dislocation density, and N_0 is the dislocation density at a reference state. This increase of chemical potential of the metal can be mainly attributed to the enthalpy increase due to the addition of new dislocations, since the associated entropy change for a metal plastic deformation process is negligible [13]. As a result, the Gibbs free energy increases by increasing dislocation density. A larger increase in the Gibbs energy can lead to a lower electrochemical potential according to the Nernst equation. A lower electrochemical potential usually leads to stronger active dissolution. This is experimentally evidenced by a dislocation etch spiral observed widely as Fig. 2-2 shown [14]. The dislocation concentrated with maximum strain undergoes an extremely fast dissolution during etching, while the spiral morphology forms as the dissolution slows down away from the core. However, the contribution of a single dislocation to the electrochemical change of the material matrix is relatively negligible in the global scale, since its associated volume fraction is extremely small.

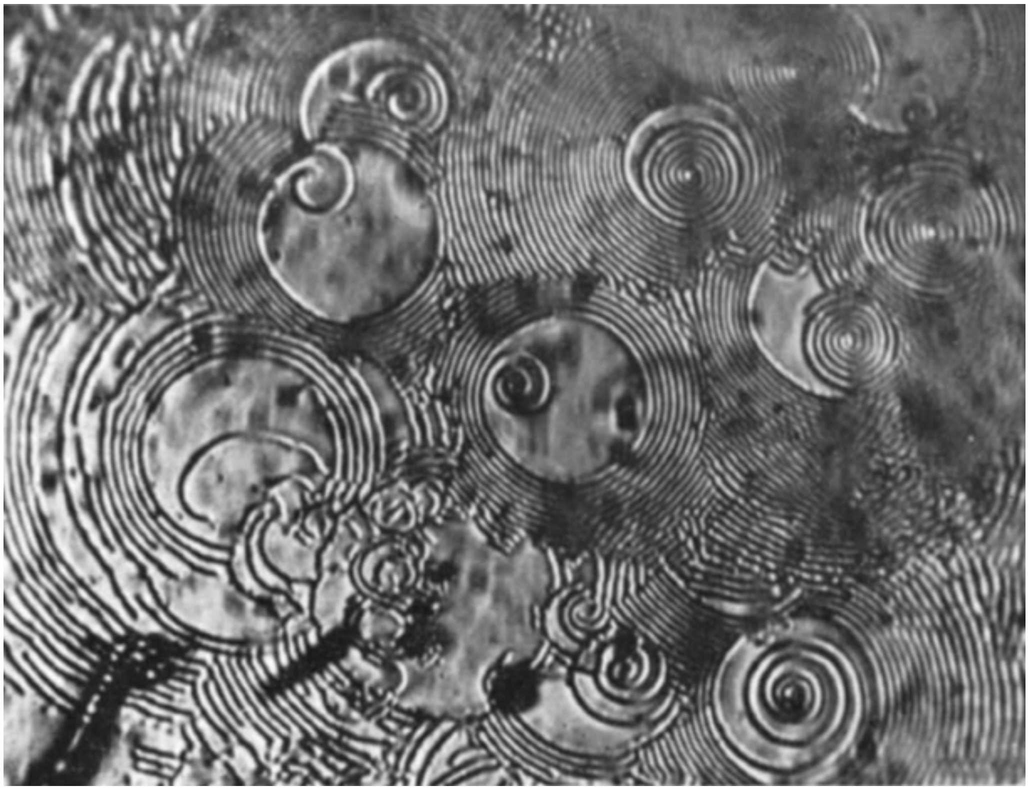

Figure 2-2. Dislocation etch spirals on a Si-Fe alloy [14].

Even though plastic deformation takes place by different means, such as compression, tension, bending and torsion, both micro-strain energy and macro-strain energy tie back to the stored strain energy thermodynamically. In electrochemistry, the thermodynamic driving force can be translated to reaction kinetics through the Butler Volmer equation when the reaction is under activation control. We will review reaction kinetics under the influence of both elastic strain and plastic strain next.

2.1.2 Kinetics of Reactions under Influence of Strain

One way to interpret the impact of the stored strain energy on corrosion kinetics is to assume a dependency of proportionality between the activation energy of corrosion reactions and the strain energy. For example, tensile stresses can be thought as a way to stretch a chemical bond, therefore accelerating re-formation of new chemical bonds. However, one weakness of this approach is that the expected result would be opposite if compressive stresses are applied.

One of the common ways to understand this strain-accelerated kinetics is to examine the Gibbs free energy change in the initial and final state of the reaction. For an irreversible chemical reaction like general corrosion to take place, the thermodynamic driving force, ΔG only depends on the difference of the Gibbs free energy between in the initial state and in the final state, regardless of the intermediate reaction compounds. A generic metal oxidation half-cell reaction can be written as

$$M - n\,e^{-} \Rightarrow M^{n+} \qquad (1).$$

If the initial state of the reactants is examined, it is expected that the stored strain energy should increases as stresses or deformation are introduced to metals. The strain energy should not alter the final state of the reaction. Therefore, the stressed/deformed metals possess a higher thermodynamic driving force, ΔG compared to the metals free of strain. In electrochemistry, the driving force, ΔG can be tied to the electrochemical potential through the Nernst equation,

$$\Delta G = -nFE \qquad (7),$$

where n is the chemical charge, F is the Faraday constant, and E is the electrochemical potential. The standard reduction half-cell potentials for different materials can be easily found in many referenced tables. At the equilibrium potential, the oxidation reaction is in equilibrium with the reduction reaction. Above the potential, the oxidation reaction dominates over the reduction reaction, and vise-versa. A deviation of the potential away from the equilibrium potential is referred as the overpotential. When an overpotential is applied to the material, one reaction will be enhanced and the other will be suppressed. This correlation is given by the Butler-Volmer equation [15]:

$$i_{net} = i_o \, exp \left(\frac{anF\eta}{RT}\right) - i_o \, exp \left(\frac{-(1-a)nF\eta}{RT}\right),$$

where i_{net} is the net current density at the applied overpotential, i_o is the exchange current density at equilibrium, a is the symmetrical coefficient (~0.5), n is the charge transferred, and η is the overpotential. The corrosion current density of an alloy/metal can therefore be calculated with some necessary assumptions and the measured potential value. According to the mixed potential theory [15], when an alloy/metal is in contact with an aqueous environment, two (or more) half-cell reactions start to polarize each other: an oxidation reaction by the metal, and a reduction reaction by the electrolyte on the metal surface. Such a mixed potential is resulted as shown in Fig. 2-3, which polarizes the half-cell reactions to an intermediate level between the two half-cell potentials. To construct such a diagram, we can assume the Tafel slope to be ~100 mV/decade. The interception points of the oxidation curves and the cathodic curve represent the corresponding dissolution current for a specific corrosion reaction. As discussed earlier that the stored strain energy lowers the electrochemical potential for the strained metals, this results in an increase in the metal dissolution in the same environment. Of course, this is an ideal case. Interferences do come into place to suppress this strain effect on metal dissolution to some extent, like electrolyte double-layer on the metal surfaces or corrosion product building up on the metal surfaces. Some of these interferences are also examined in Chapter 4.

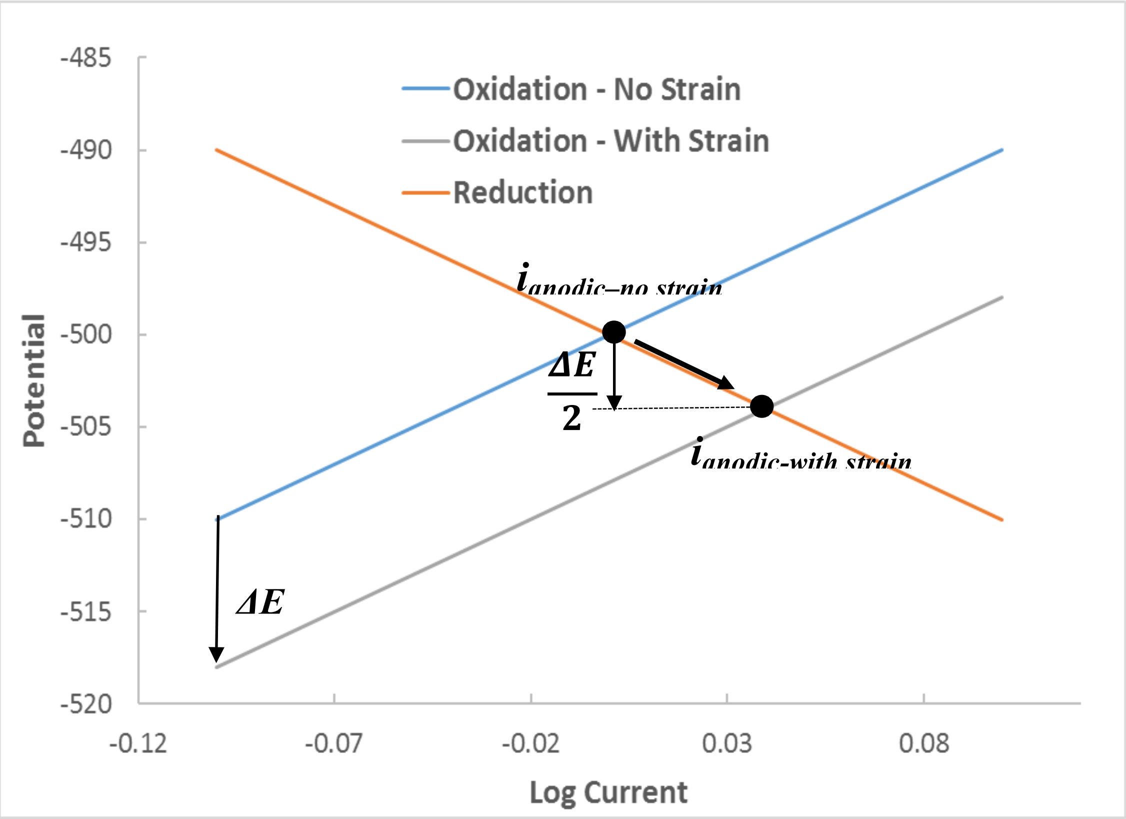

Figure 2-3. A representative linear polarization diagram.

2.1.2.1 Contribution of Elastic Stresses

Previously, it was concluded that the stored strain energy, W_{strain} increases the Gibbs free energy of the material. Let us examine how the strain directly changes the Gibbs free energy of the material on the microscopic scale. According to Gutman, if a metal is subjected to an excess elastic stress (σ), either compression or tension, it will lead to a chemical potential change of the material [13]. The new chemical potential can be written as

$$\mu = \mu_{\Delta P=0} + \Delta\ \sigma\ V_m \qquad (2.15),$$

where μ is the chemical potential, Δσ is the surface stress change with respect to the material free of stresses/pressure, and V_m is the molar volume of the material. Consequentially, Gutman derived that the electrochemical change, ΔE due to the presence of the applied strain/pressure is

$$\Delta E = - \frac{\Delta\sigma * Vm}{nF} \qquad (2.16).$$

It is noticed that Eq. 16 looks strikingly like Eq. 7 (the Nernst equation), since this excess chemical potential essentially contributes to the Gibbs free energy change of the corrosion reactions. Therefore, the accelerated dissolution current can be calculated if the change in surface stresses/pressure is known,

$$i_{a\text{-with strain}} = i_{a\text{-no strain}} * exp\ \frac{\Delta E}{2RT} \qquad (2.17),$$

where i_a is the anodic current, and R is the gas constant. This is already well-illustrated in Fig. 4 and the effect of the strain energy here is like applying an anodic overpoential to increase the anodic current. It is noticed in Eq. 17 that only ½ of ΔE is contributing to the exponential term. This is because the symmetrical reduction reaction on the same material typically stays unchanged, and thereby the new open circuit potential (OCP) is established at a lower level by ½ of ΔE.

Earlier experimental work also confirmed this accelerated dissolution trend due to elastic stresses. Johnston reported an accelerated dissolution rate of Cu under different elastic stresses in 0.1 M H_2SO_4 solution [16]. He used the concentration change of Cu^{2+} in the solution over different periods of time as a measure of dissolution rates of Cu under different applied elastic stress levels as Fig. 2-4 shown. A linear increase in dissolution rate was found as the stress level increased, indicating that the strain energy accelerated general corrosion or dissolution rate of Cu under activation control. The active dissolution rate of a high-strength martensitic steel (0.3%C, 1%Si, 0.9%Mo, 1%Cr, 0.45% Ni) was also measured in a base solution of 20% H_2SO_4 with/without 30 g/L NaCl by Gutman as shown in Fig. 2-5. As indicated in Fig. 2-5, an aluminum sample was also tested in a base solution of 1M NaCl and 1% HCl with/without 0.1% H_2O_2. The similar trend of increasing dissolution rate as a function of elastic stresses was again observed in Fig. 2-5.

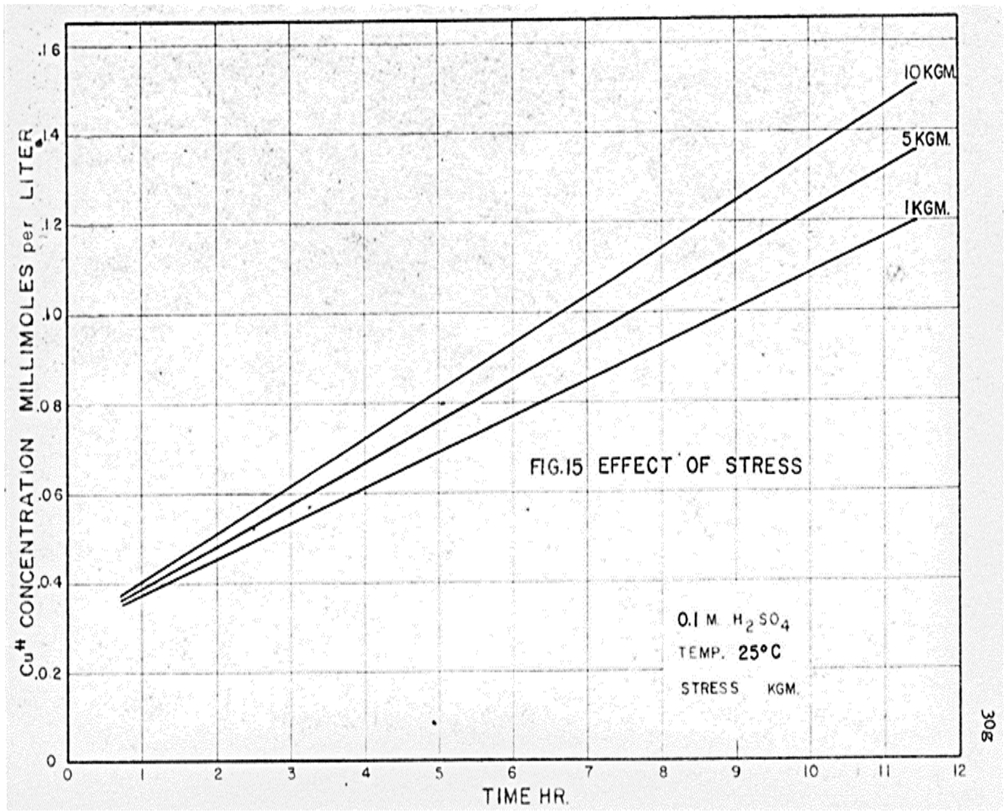

Figure 2-4. Effect of stresses on dissolution rates of Cu in 0.1 M H_2SO_4 solution [16].

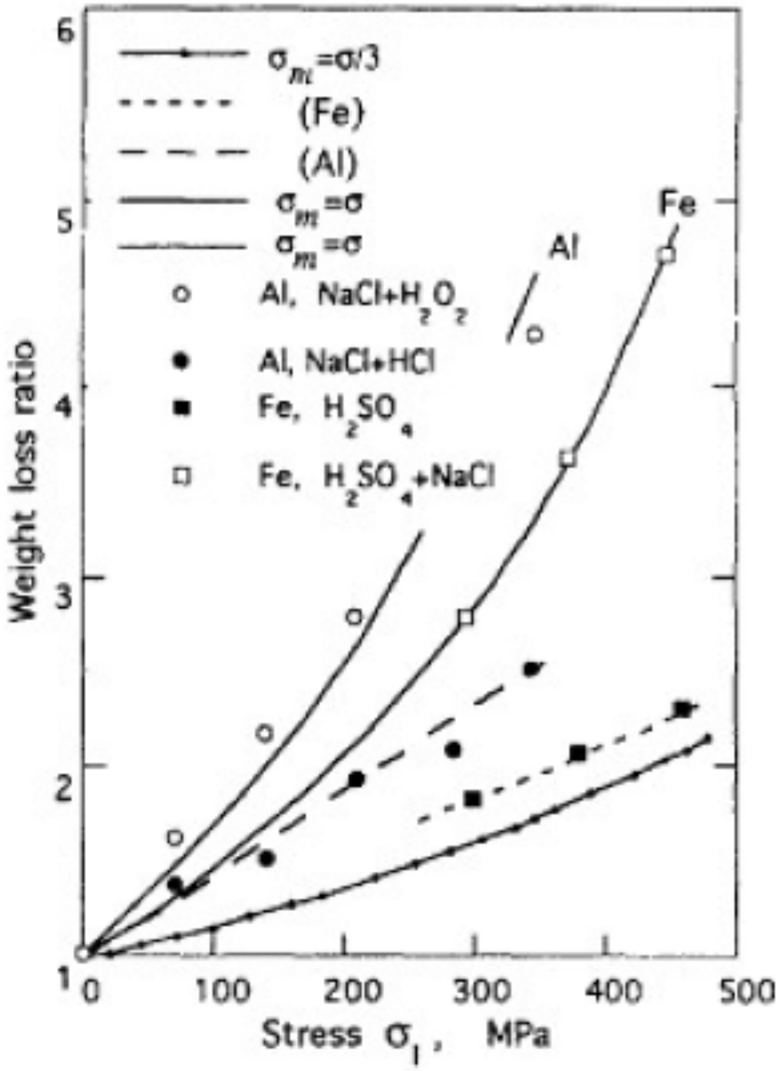

Figure 2-5. Effect of stresses on dissolution rates of a high-strength martensitic steel in different environments [13].

2.1.2.2 *Contribution of Structural Defects*

The discussion in this section follows the same guideline: an additional strain energy accelerates active dissolution. When plastic deformation takes place, the plastic strain exists in two forms: micro-strain and macro-strain as reviewed in Section. 2.1.1.2.

Let us review the process of plastic deformation at different stages. Dislocation interaction can cause resistance to further deformation by mechanisms like dislocation interaction and dislocation pile-up, thereby strain-hardening the material. Different stages of strain hardening in a single crystal can be manifested using Fig. 2-6 [13]. τ_0 is the critical shear stress to overcome the inertia on an entrained dislocation. τ_1, τ_2 and τ_3 corresponds to the shear stress at easy slip (stage I), strain hardening (stage II) and dynamic recovering (stage III). New dislocations can be generated throughout the whole plastic deformation process. Gutman explained the interaction of dislocations and its resultant influence on the stored strain energy [13]. At the easy slip stage, dislocations are being generated and tend to move towards the surface of the solid crystal, observed as slip-lines on the surface. In addition, relaxation of existing dislocation pile-ups may take place, so the rate of dissolution during this stage should not be accelerated much. At the next stage of strain hardening, while new dislocations are still being generated, dislocations start to slip across a set of planes, which causes pile-up of dislocations. The formation of dislocation pile-ups greatly increases the internal strain energy of a crystal solid. The electrochemical change ΔE around a dislocation pile-up was theoretically calculated by Gutman [13]

$$\Delta E = -\frac{N\Delta\tau R}{aR'nF} \qquad (2.18),$$

where N is the number of dislocations in a pile-up, $\Delta\tau$ is the excess shear stress that a pile-up exerts on its vicinity, "a" is the chemical activity of the material, $R' = kN_{max}$ (k is the Boltzmann constant and N_{max} is the maximum possible dislocation sites).

Consequentially, the strain energy associated with the elastic stress field around a dislocation pile-up significantly increases. Therefore, the active dissolution rate in this stage is monotonically increasing with the increase of the degree of the plastic deformation. At the last stage, the pile-up of dislocation starts to fail, and dislocations are re-grouped by cross-slip. As a result, dislocations are partially annihilated to form sub-boundaries, and the elastic dislocation field is weakened. During this stage, roughly 95% of the store strain energy is dissipated as heat [13]. Of course, this value may vary from one material to another, but the rule of thumb is that smaller-grain crystalline solids possess a higher fraction of the retained strain energy. This is because the dislocations tend to pile up at obstacles like grain boundaries. As a result, it can be expected that the effect of plastic deformation in the later stage on active dissolution is alleviated.

The theoretical analyses above may not be completely applicable to every metal or alloy, since different alloys may differ in various deformation mechanisms. For example, twining is very like to take place in FCC metals at a low degree of plastic deformation, and severe plastic deformation can induce martensitic transformation at room temperature in stainless steels like SS304 [17-23]. Therefore, the prediction of reaction kinetics of general corrosion or active dissolution should be subject to specific alloy/environment systems.

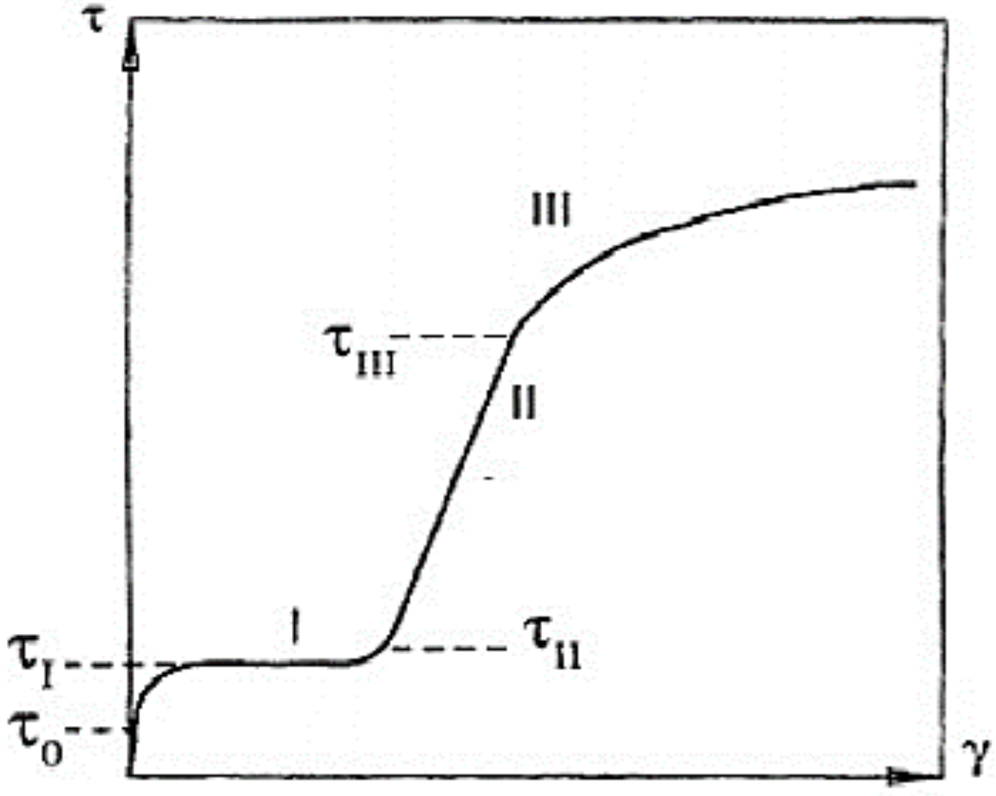

Figure 2-6. The hardening curve in a single crystal [13].

2.1.2.3 Crack Tip Dissolution for Stress Corrosion Cracking (SCC)

Stress corrosion cracking has caused many catastrophic failures in near neutral pH environments, for example, buried pipeline steel in ground water [24, 25]. It is widely accepted that the crack growth rate is mainly determined by the crack tip dissolution rate under the synergistic effect of hydrogen retention and strain [26, 27]. During stress corrosion cracking, the bare metal at the crack tip has a state of stress concentration where plasticity and stresses are intensified. Therefore, strain-enhanced general corrosion is analogous to the active dissolution of the bare metal at the crack tip during anodic-dissolution controlled SCC from the dissolution perspective. However, SCC can exhibit a more complex mechanism than simply metal dissolution. This is because SCC does not require a pure activation control, and crack growth involves other external contribution, such as film rupture at the crack tip leading to incremental crack growth. Nevertheless, the higher dissolution rate of X-65 carbon steel at the crack tip was still reported during stress corrosion cracking in a near-neutral chloride-containing solution [28]. Yaguchi and Toshio argued that the enhanced dissolution rate at the crack-tip had a dependency on local plastic strain during stress corrosion cracking [29].

2.1.3 Effect of Strain on Catalytic Activities for Reduction Reactions

All the discussion above assumed that the reduction reaction kinetics on the metal surfaces stays unchanged. However, the lattice strain has been reported to affect the catalytic properties of a metal nano-particle surface by altering the binding behaviour of adsorbates and modifying the catalytic activities [39]. According to the d-band theory, the metal d-band can hybridize with the bonding orbital of the adsorbate and form bonding and antibonding states [39, 40]. A higher d-band centre translates to stronger binding between the metal and the adsorbate, and a lower d-band centre has the opposite effect. This altered catalytic activity on strained metal surfaces could therefore be explained by a shift in the d-band centre of the metal nanoparticle due to the lattice distortion caused by strain. According to this theory [40], compression and tension have opposite effects on the shift in the d-band centre: a compressive lattice strain lowers the d-band centre, while an expanded lattice strain raises the d-band centre. As a result, the lattice distortion due to strain alter the ease of molecule-sorption energies. Depending on the nature of metal surfaces, the effect of strain on catalytic activities can also be different. In metal systems like Pt and Ni where adsorption of H onto the metal surface is energetically favorable and the subsequent recombination of H to form H_2 is energetically unfavorable, it was found that elastic compression enhanced the catalytic activity for the hydrogen evolution reaction on the surfaces of Pt and Ni, while tensile strain suppressed the H_2 evolution [41]. This was because compression between lattices lowered the energy barrier for the recombination of H to form H_2, while tension introduced the opposite effect. In some other metal systems like Cu, the energy shift for adsorption of H onto the metal surface is energetically unfavorable, and it is energetically unfavorable for the subsequent release of H_2. This made the first step the rate-limiting step. As a result, it was found that tension strengthened the H adsorption binding, therefore facilitating the first step, while compression had exactly the opposite effect on H_2 evolution [41].

It is then reasonable to believe that strained steel surfaces can have different catalytic activities on the reduction reaction when general corrosion takes place. This can establish a slightly different open circuit potential (OCP), therefore causing a potentially altered overpotential for the metal oxidation reaction. It will add some ambiguity when estimating the relative corrosion rate using the OCP shifts. The study of strain effect on the catalytic activities for the related reduction reaction on the metal surface is beyond the scope of this thesis. However, this issue is addressed later in the thesis when discussing the relative corrosion rate using the changes of OCP among specimens applied with different strain. However, evaluating the absolute corrosion rate using immersion tests still stand accurate, since weight loss measured before and after the immersion test directly reflects the absolute corrosion rate.

2.2 Passive Film and Passivity

Stainless steels can be catagorized into four main groups according to their crystal structure and microstructure: austenitic, ferritic, martensitic, and duplex (about 50% autennitic and 50% ferritic

). Among different grades of stainless steels, different alloying elements are added to achieve different engineering demands. For example, molebdenum (Mo) and nitrogen (N) are typically added for high corrosion resistant alloys. Stainless steels containing at least 12% Cr are passivated by forming a thin layer of Cr_2O_3-rich oxide film on the surfaces. This passive oxide layer is mostly amorphous and about 2-3 nm thick. The presence of passive film acts as a physical barrier to prevent bare metals from general corrosion especially in low pH and highly oxidizing environments. The application of stainless steels in highly corrosive environments is a perfect example where reaction kinetics rule over thermodynamics. The underlying mechanism of the highly corrosion resistant film is that the formation of the passive film is much faster than the dissolution of the film into the environment. Therfore, it becomes a diffusion barrier, governing the charge transfer across the film. This limits corrosion reactions on the metal surfaces regardless of the oxidation tendancy purely indicated by thermodynamics.

While metals are under passivation-control, passive film forms to slow down or prevent further oxidation. Even though passive films impart passivity to various alloys, the passivity still breaks down under specific circumstances. A typical active-passive behavior of a metal over a complete anodic polarization range is demonstrated in Fig. 2-7, in which the anodic oxidation reaction of metals is under activation-control (general corrosion occurs), transitions to passivation-control range beyond E_{pp} (protective passive film forms), and eventually enters the transpassive regime (passive film is no longer stable and starts to break down). It is worth noticing that the transpassive reaction for many alloy/environment systems may involve oxygen evolution, along with or instead of oxide film dissolution/breakdown. It is different from the pitting breakdown which usually leads to an exponential increase in current at a very short potential range. Therefore, passivity can break down at appropriate potentials and environments. One important consequence of breakdown of passivity is localized corrosion, such as pitting corrosion. The influence of strain on pitting corrosion will be systematically addressed later in this thesis.

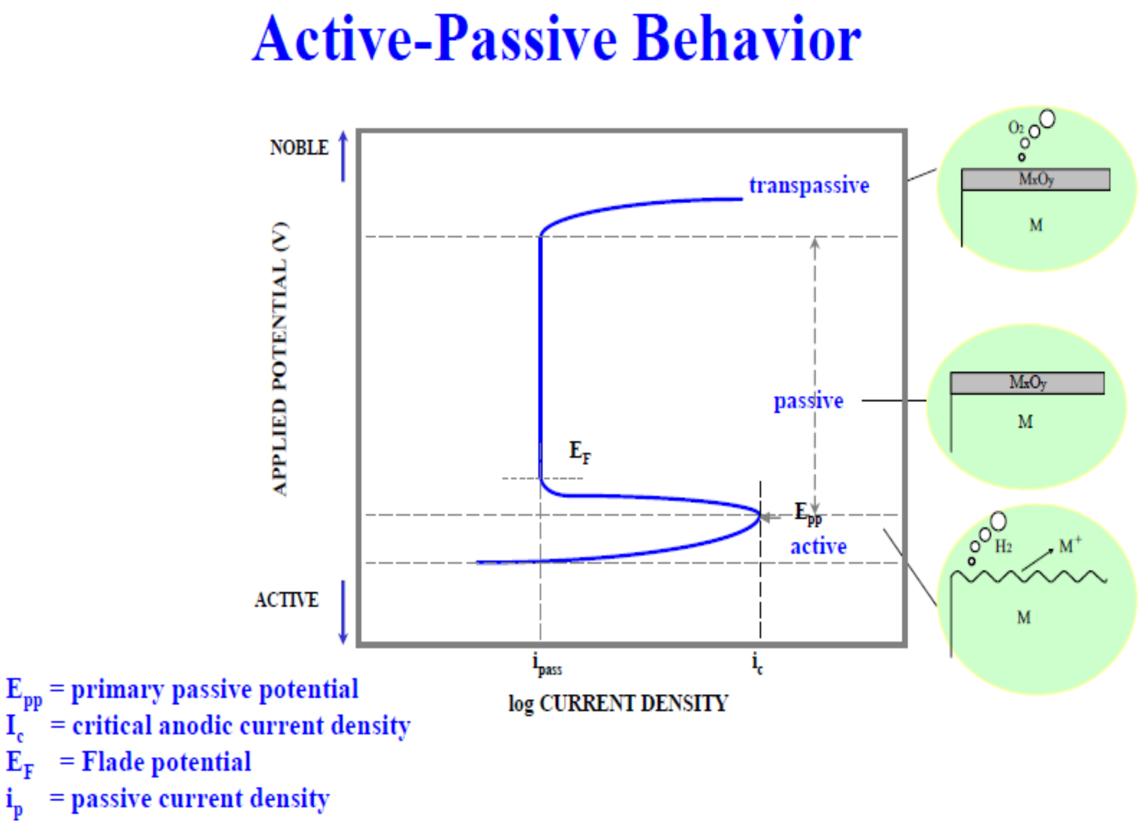

Figure 2-7. A typical active-passive behavior of metals.

2.2.1 Characteristics of Passive Film

The three paramount characteristics of passive film that affect its behavior are chemical composition, structure, and thickness [33]. The passive film functions as a semiconductor when the alloy is under passivation control. This gives the passive film some dieletric properties that can be interesting to investigate. All these properties are correlated to chemical composition, strucure and thickness of the surface film.

2.2.1.1 Surface/Film Chemical Composition

Chemical composition of the passive film on metal surfaces is usually investigated by the surface analysis methods like X-ray photoelectron spectroscopy (XPS), Near Edge X-Ray Absorption Fine Structure (NEXAFS), and Auger electron Spectroscopy (AES) [34-37]. The challenge of these ex-situ techniques is to preserve the native surface conditions of passive films without oxidizing it in the air. Therefore, sample transfer was carried out, using vacuum containers. Most passive films formed on alloys in aqueous environments are oxides or hydroxides of active elements in the alloy. Passive films can be amorphous or crystalline. Alloying elements, microstructure and surface treatments are three major factors that affect the chemical composition of a passive film.

In stainless steel systems, alloying elements like chromium (Cr), molybdenum (Mo) and nitrogen (N) are added to stainless steels to improve their pitting resistance. Stainless steels have at least 12% Cr, and the development of corrosion resistant stainless steels were all built on this common principle. As for Mo, it has a complex but beneficial effect on the active/passive behavior of steels [38-40]. For active dissolution/general corrosion, it forms some Mo-compounds to inhibit further oxidation reaction. When passivity is established, the enrichment of Mo near metal surfaces leads to a better corrosion resistance of the passive films [40-42]. When the passive film breaks down and pitting take place, there are various models/mechanism developed to explain the role of different Mo-compounds to inhibit the pitting corrosion in different environments [41, 43]. In addition, the interaction between Mo and N was discussed in detail by Lu and Clayton [44-48]. The beneficial effect of N on improving pitting resistance of stainless steels was also widely studied, and different mechanisms were proposed [49, 50]. For example, one mechanism claimed that N caused the formation of ammonia/ammonium ions, thereby increasing pH in pit solutions during pit growth through the reaction below [51]:

$$N^{3-} + 4H^{+} \rightarrow NH_4^{+} \qquad (2).$$

In addition, N as a less expensive material makes it a more commercially feasible choice as an alloying element. Pitting resistance equivalent number (PREN) has been empirically derived to assess the pitting resistance of different alloys based on their chemical compositions [41]. A typically used version of this PREN formula is given as

$$PREN = Cr + 3.3Mo + 16N \qquad (2.19).$$

Even though the passive films can be as thin as 2-3 nm, the chemical profile of each individual element can vary drastically along the depth. Enrichment of certain elements can often be achieved by different heat/surface treatments and diffusivities of different alloying elements to establish passivity on the metal surfaces.

Microstructure also plays an important role in the chemical composition of passive films. To be more specific, microstructure can potentially cause inhomogeneity of the surface chemistry. The inhomogeneity of surface chemical composition thereby leads to the formation of galvanic couple that may further result into the preferentially dissolution of the active phase, which gives rise to pit initiation and growth. For example, formation of carbides like CrC_{23} consumes Cr around the carbide, which creates an anodic surrounding since a Cr-depleted zone is typically developed around CrC_{23} [52, 53]. This galvanic coupling provides potential pit initiation sites and provokes pitting corrosion at lower potentials. Intermetallics also inhibit pitting resistance by upsetting the homogeneity of surface chemical composition. For example, sigma phase in stainless steels contains high Cr content. This creates local galvanic couple analogous to the CrC_{23} case [53-56].

Surface treatment is another practice that is used to alter the chemical composition of the passive film to improve corrosion resistance of stainless steels. For example, pre-oxidizing or pre-anodizing can enhance and stabilize Cr and Mo content in the surface film, therefore improving pitting resistance of steels. Pre-oxidizing is typically achieved by using highly oxidizing agents, like high-concentration nitric acid. Pre-anodizing is usually performed by using electrochemical techniques. This technique is more popular for aluminum alloys, since a thick oxide film can easily form on Al. For example, one can grow a thick oxide film of several micrometers on specific aluminum alloys by imposing a positive current or voltage through the alloy to be anodized. A very refined surface finish can be achieved by tweaking the anodizing technique, such as pulse-anodizing [57].

2.2.1.2 Structure of Passive Film

The structure of passive film plays a crucial role in materials' corrosion resistance. Both in-situ and ex-situ techniques can be employed to study properties/structure of passive films. Ex-situ techniques typically involve post-analysis using TEM. There are two different types of in-situ techniques: in-situ scanning tunneling microscopy (STM) and EIS [39]. McBee and Kruger investigated the structre of the passive films on Fe-Cr alloys and found that passive films could be either amorphous or crystalline depending on Cr concentrations [58]. Ryan et al. [59, 60] confirmed their findings, and further elucidated that the passive film for Fe-Cr alloys was mainly amorphous for 12%~19% of Cr. Below 12%, it was crystalline both in borate buffer sulution and in an acid solution.

Due to the dieletric nature of passive films, point defect model (PDM), schematically shown in Fig. 2-8, become a very important tool used to understand the structure and stability of passive film [61]. PDM assumes that the electric field across the passive film remains unchanged throughout the growth of the passive film in the passive state. Reaction (2) and (5) describe the generation and anihhilation of metal interstitial vacancies, M_i^{x+}. Reactions (3) and (6) correspond to the growth of passive film. Reaction (3) indicates the oxidation of a bulk metal atom, creating a Schottky pair, $V^{x'}_M/V^{\cdot\cdot}_o$ and filling in the cation vacancy. Reaction (6) describes the annihilation of oxygen vacancies in the oxide/solution interface. According to PDM [61, 62], the inner passive layer (next to metal) and outer passive layer (next to solution) contain different ionic defects (vacancies and interstitials). The net flow of ionic defects produces the passive current. With a p-type passive film, the metal vacancy generation reaction (4), $M_M \rightarrow M^{\delta+}(aq) + V^{x'}_M + (\delta-x)e'$, is dominant. $V^{x'}_M$ here is a electron acceptor as it is accompanied with electron holes, $(\delta-x)e'$. The passive current of p-type film is exponetially correlated to the applied potential, yet the passive current if n-type film has no dependency on the applied potential [61]. The metal vacancy generation indicated as reaction (4) and the metal vacancy annihilation indicated as reaction (1) reach an equilibrium. N-type film is dominant by the oxygen vacancies (electron donor) generated in reaction (3).

A number of researchers have demonstrated the effect of strain on the stability of passive film of both carbon steels and stainless steels [3, 63-67]. Kumar et al. found strain destablized the passive film of stainless steels 304L and 316L in a 0.1 M NaCl solution [3]. They argued that the residual stress destabilized the passive film, leading to the changes in polarization behavior. Several authors studied the deformation-influenced passive film structure of austenitic stainless steels and duplex stainless steels in Cl-containing environments, and found that the density of donors ($V^{\cdot\cdot}_o$) and acceptors ($V^{x'}_{M}$) both increased in the presence of deformation [3, 63, 68]. Yoon and Lee suggested that the corrosion resistance of the passive film decreased with the increase in density of acceptors and donors [69]. However, Lv et al. found that plastic deformation refined the microstructure of 2099 aluminum alloy, thereby resulting in a decrease in thr acceptor density and an improvement in alloy’s corrosion resistance [70].

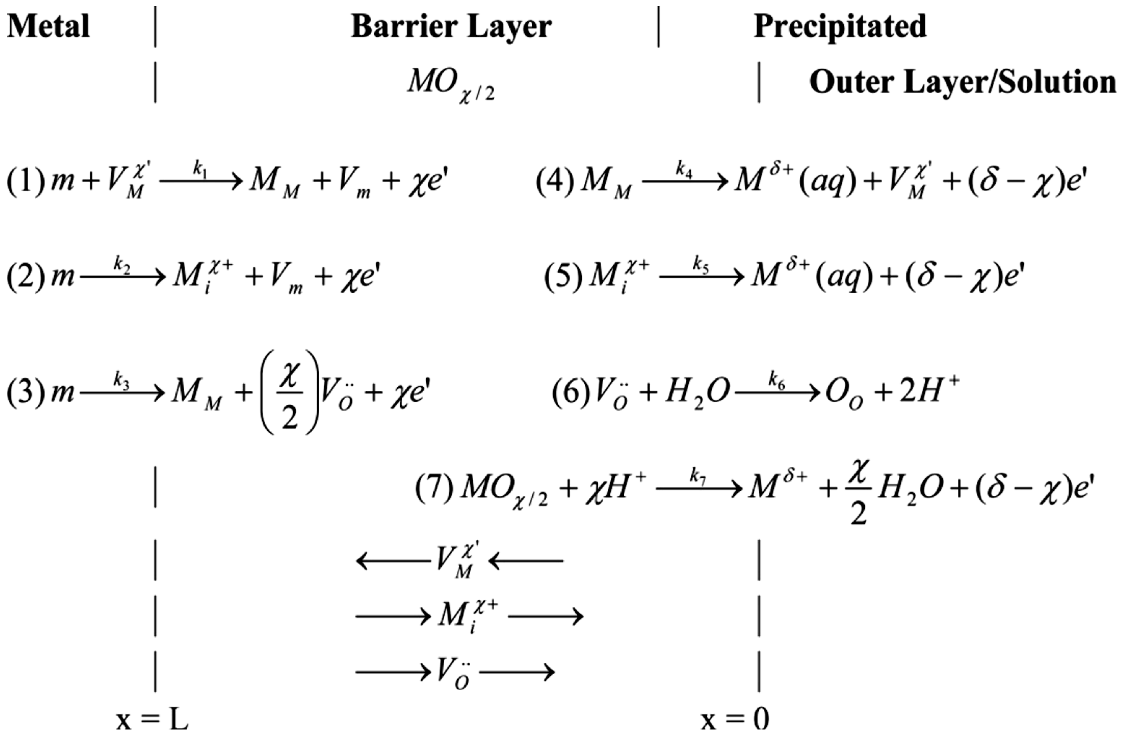

$$(1)\, m + V_M^{\chi'} \xrightarrow{k_1} M_M + V_m + \chi e' \qquad (4)\, M_M \xrightarrow{k_4} M^{\delta+}(aq) + V_M^{\chi'} + (\delta - \chi)e'$$

$$(2)\, m \xrightarrow{k_2} M_i^{\chi+} + V_m + \chi e' \qquad (5)\, M_i^{\chi+} \xrightarrow{k_5} M^{\delta+}(aq) + (\delta - \chi)e'$$

$$(3)\, m \xrightarrow{k_3} M_M + \left(\frac{\chi}{2}\right) V_{\ddot{O}} + \chi e' \qquad (6)\, V_{\ddot{O}} + H_2O \xrightarrow{k_6} O_O + 2H^+$$

$$(7)\, MO_{\chi/2} + \chi H^+ \xrightarrow{k_7} M^{\delta+} + \frac{\chi}{2} H_2O + (\delta - \chi)e'$$

Figure 2-8. Schematic of Point Defect Model (PDM) [61].

2.2.1.3 Thickness of Passive Film

Thickness of a passive film appears to be particularly important for corrosion applications in the early stage of passive-film formation. There are various techniques to assess the thickness of a passive film. Again, these techniques can be categorized into in-situ techniques and ex-situ techniques. In-situ techniques typically utilize some simulation/modeling by treating the passive film as a circuit in an EIS measurement. For example, a simple Randles circuit as shown in Fig. 2-9 is often used directly or tweaked to model the behavior of the passive film based on EIS measurements. Based on this simplistic model, thickness, d_{film}, of the passive film can be calculated as [71, 72]

$$d_{film} = \frac{\varepsilon \varepsilon_0 A}{C},$$

where ε is the relative permittivity, and ε_0 is the permittivity in vacuum, A is the cross-section area and C is the capacitance calculated using the Randles circuit. It is noted that these parameters could be temperature-dependent, so it requires some caution when using this method to determine film thickness.

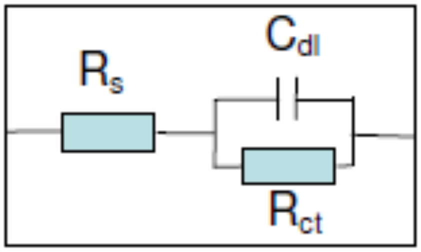

Figure 2-9. A simple Randles circuit schematic [73].

As for ex-situ techniques for thickness assessment, samples are carefully prepared and preserved in vacuum. Information on the depth profile by using the chemical composition is usually measured using XPS or AES analysis of film while removing the film layers by sputtering. By examining a depth profile of chemical composition near the surface, the thickness is often determined at the intersection point where the oxygen profile crosses the Fe^{2+} profile.

Numerous researchers have investigated the physical structure of the passive film under the influence of strain. Lv and Luo suspected that the band gap of the passive film was reduced due to strain [2]. Vignal and Manchet reported that the thickness of passive film of duplex stainless steels UNS S32202 in chloride-containing environments decreased due to local plasticity [74]. Based on the pertinent prior work, it can be summarized that strain may lead to a more defective and thinner passive film, therefore weakening the corrosion resistance of stainless steels.

2.2.2 Environmental Influence on Passivity

Stability of passive films on stainless steels is subject to intrinsic material-engineering designs as discussed in the previous section, as well as on the environmental factors, such as potential, pH, and aggressive anions in solutions.

Firstly, both the thickness and the chemical composition of passive films can be altered by the applying a potential at which the film grows. Fig. 2-10 shows the passive film thickness of dependency on the applied potential in 0.5 M H_2SO_4 for both Ar-sputtered and pre-activated Fe-15Cr specimens [75]. In the passive regime, the thickness of passive films is linearly proportional to the applied potential. It was noticed that pre-activated specimens had lower values of film thickness because Cr was accumulated on the surface during the pre-activated active dissolution in an acid solution. No passive film was stable in the active region and in the transpassive region as indicated by the dropping thickness as the potential went outside the passive range. The passive film on Fe-15Cr specimens consisted of both oxides and hydroxide, with the hydroxide closer to the electrolyte. Results indicate that the thickness of the film increase mainly came from the oxide portion, indicating the rate-limiting process in this system was taking place across the metal/film interface [75]. It was also reported in the same paper that Cr-enrichment is more dominant at the lower potential range of the passive region. The Cr content tended to decrease in the higher potential range, since the stability of Fe at higher potentials increased. In addition, it was also reported that the thickness of the film had very minimal growth from 20 minutes to 20 hours. This meant that the film growth kinetics was very fast in the early stage and slowed down with time.

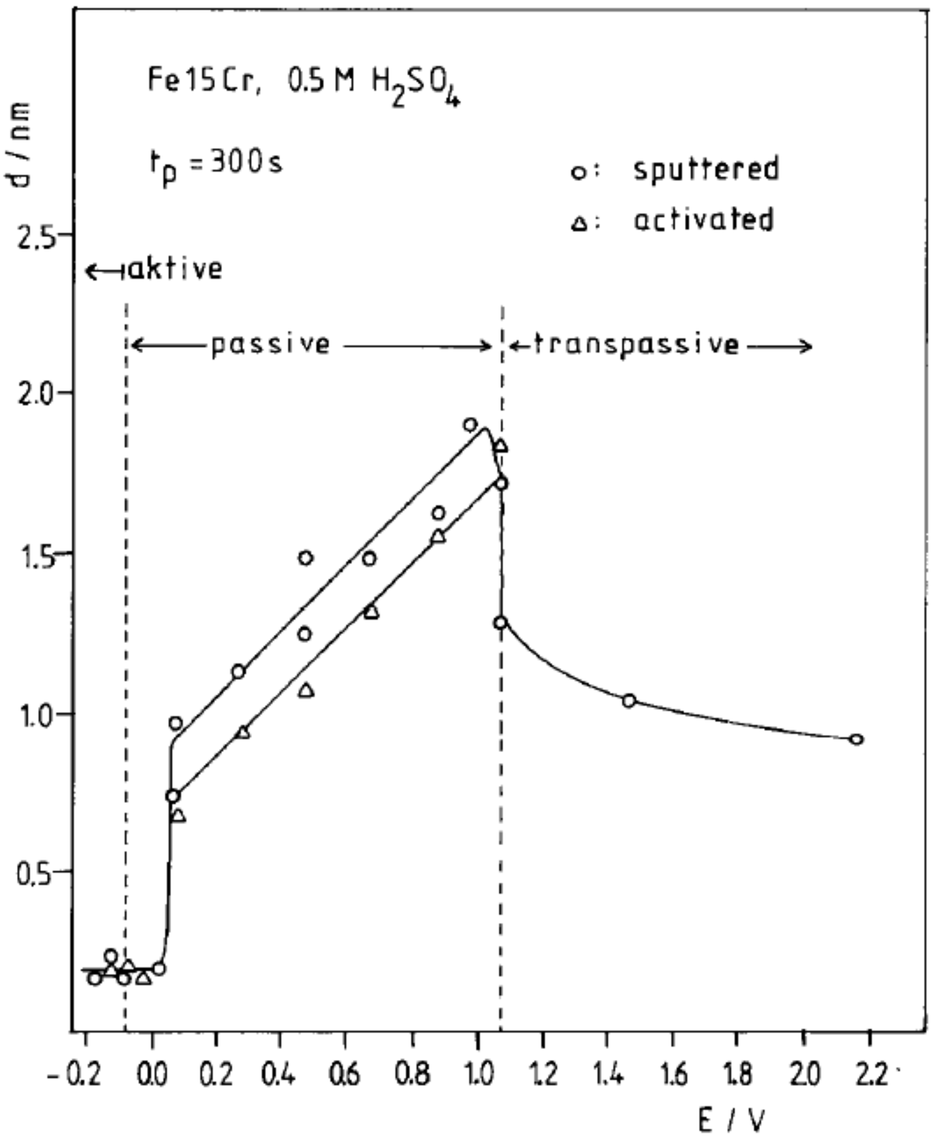

Figure 2-10 Thickness of passive film formed on 0.5M H_2SO_4 for 300 seconds on a Fe-15Cr alloy surface with the increasing applied potential [75].

Aggressive anions like chloride, sulfate, and thiosulfate also impede the passivity of passive films according to the penetration model and the adsorption model [76-81]. These anions can facilitate either the pit initiation and/or the pit growth, thereby destabilizing the passive film. For example, Cl^-, can be adsorbed onto the passve film, and replace oxide or hydroxide to loosely bond with metal cations, therefore destablizing the passive film and promoting a pit initiation. This is supported by the observation of Cl^- in the passive oxide layer using techniques such as X-ray photoelectron spectroscopy (XPS) and X-ray Absorption Spectroscopy in various alloy systems [34-37]. A detailed review on the influence of caustic anions on passivity will be manifested in the section of pitting corrosion.

In addition, pH also imposes an important environmental impact on the stability of passive films. The main effect of a lower pH is that it causes a higher dissolution rate of passive films. Therefore, a lower pH leads to a thinner passive film. The pH effect was well demonstrated in stainless steel systems by Strehblow et al [75, 82]. It was found that the passive film in a Fe-Cr alloy was significantly thicker in a basic environment than in an acidic environment [83]. A simple rationale for the thickness-dependency on pH is that the oxide dissolution rate to electrolytes is higher at lower pH than in higher pH vlues. It is also reflected on the Fe Pourbaix diagram as shown in Fig. 2-1 that the passivation potential range is cut narrower as the pH decreases.

2.2.3 Rupture and Evolution of Passive Film upon Yielding

Since the passivity/stability of passive films determines the corrosion resistance of stainless steels, it becomes intriguing to investigate the evolution of passive films during deformation. There was no evidence of the passive film being ruptured or destabilized in the regime of elastic deformation [84], however it is widely reported that passive film ruptured during plastic deformation [84-88]. The phenomena of the passive film rupture can be further associated with the stress corrosion cracking (SCC) mechanism. According to Engseth and Scully [86], film-rupture upon yielding can facilitate cracking with an appropriate combination of materials, potential and environments. The synergy of these three factors results in stress corrosion cracking when the repassivation rate is in an optimum range: too fast repassivation could not accumulate sufficient corrosion damage to increment an additional crack growth; too slow repassivation gives rise to localized corrosion, rather than cracking. In addition, SCC is highly potential dependent and typically causes a quasi-cleavage fracture surface. Upon examination of the fracture surfaces from a tensile tests in 4M NaCl at 50 ^{o}C under different potentials as shown in Fig. 2-11, Kwon [87] found that SCC-dominant fracture occurred right above the repassivation potential, -250 mV. Therefore, the fracture surfaces developed at -210 mV and -230 mV demonstrated SCC-type fracture morphology, while the one developed at -110 mV, which was right below its pitting potential appeared as a severe dissolution-mode fracture. Kwon argued that the potential range needed to be in an appropriate range – between the repassivation potential and the pitting potential, but closer to the repassivation potential, to favor the SCC attack. In such a narrow potential window, repassivation was suppressed just enough to cause corrosion damage to facilitate crack growth, but not so much that it resulted into the dissolution-mode fracture.

Apart from the SCC perspective, it is known that the steels with a passive film on the surfaces plastically deform upon yielding. Much work used the mechanical straining techniques to investigate the film rupture during plastic deformation [84, 86, 88]. During this process, the passive film ruptures at slip steps as slip migrates to surfaces. Analogously, scratch test is an electrochemical technique to physically rupture the passive film at an applied potential and following the resultant current to understand the kinetics of film repair. Using this technique, it has been widely reported that a local breakdown of passive film can potentially lead to pitting corrosion in aggressive environments, such as in a $Cl^- + S_2O_3^{2-}$ environments [89, 90]. Therefore, ruptured passive films can either repassivate or initiate pitting corrosion. This may also apply to the films ruptured due to plastic deformation.

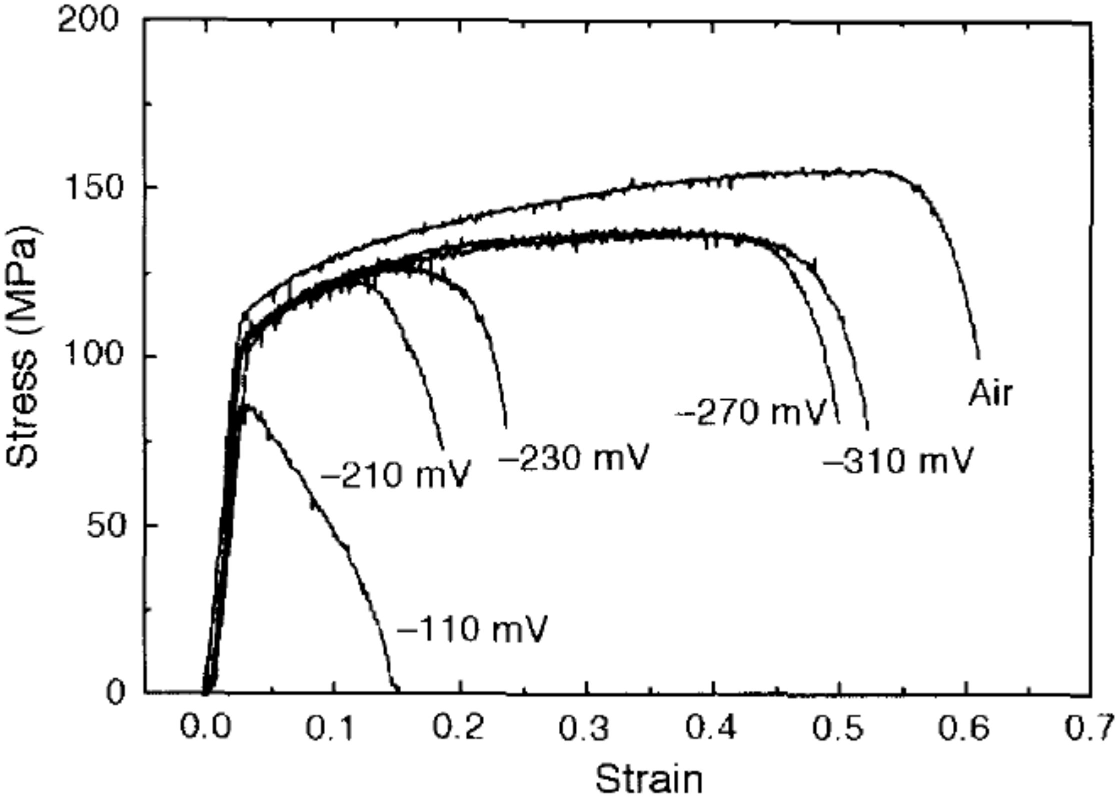

Figure 2-11. Effect of applied potential on the tensile test for stainless steel 304 in 4M NaCl at 50 °C [87].

Continuous yielding by applying a constant strain rate has also been reported to destabilize the passive film [84]. Anodic current of iron was found to increase as plastic deformation took place at a constant strain rate in 1M H_2SO_4 as Fig. 2-12 shown [84]. The increased anodic current did not rise as individual spikes. Instead, it reached a steady state gradually. Since film rupture and film repair typically are indicated as current spikes, the author argued that the increase in the anodic current was likely ascribed to the defective structure of the plastically deformed film. The impedance data corresponding to each strain level also confirmed that the film resistance decreased as the strain level increased. The author proposed a film thinning model to explain the destabilized passive film during plastic deformation.

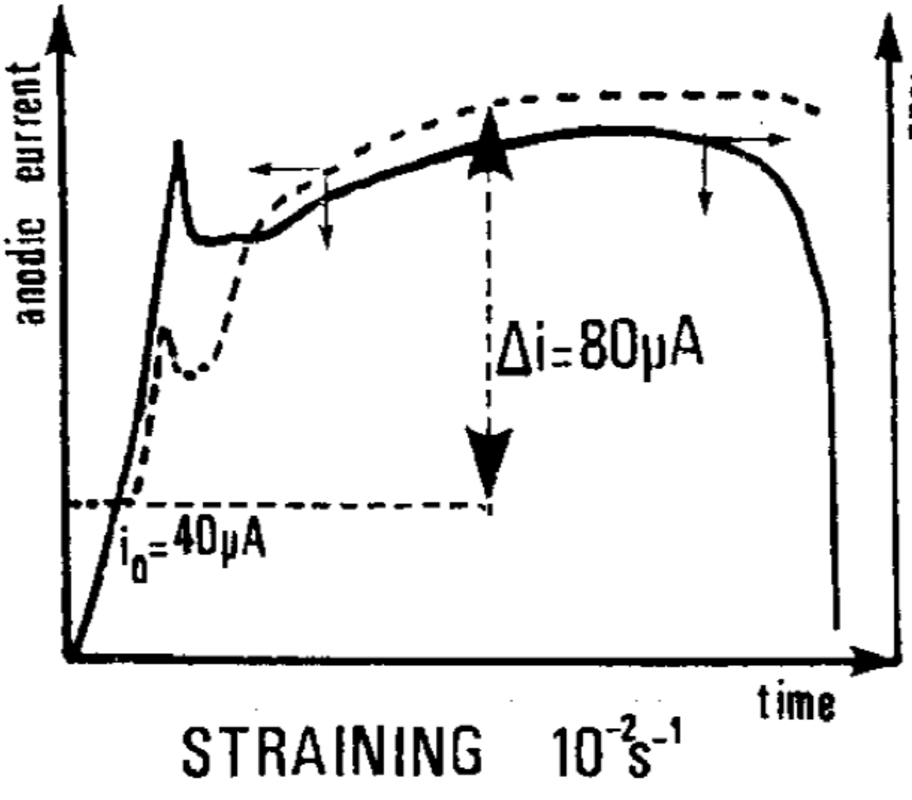

Figure 2-12. Anodic current of iron as a function of time during a straining process in H_2SO_4 at 25 °C [84].

On the contrary to the observation of destabilization of passive films on stainless steels, Lv Jinlong found that a prior cold-rolling process refined the structure of grains and precipitates in the Al-Li aluminum alloy 2099 [70]. The resultant alloy possessed a lower value of electron work function, and this facilitated the formation of a passive film with a lower concentration of acceptors, as measured by using Mott-Schottky tests. Therefore, it led to a better polarization performance in a borate buffer solution.

To summarize the evolution of passive films under the influence of plastic deformation, the film is ruptured and likely destabilized during the plastic deformation. This can result in an increased suceptibility of materials to various types of corrosion, such as SCC and pitting corrosion. However, some plastic deformation can essentially refine microstructure in some material/environment systems, especially with second-phase particles present in the microstructure. In such cases, plastic deformation may have a beneficial effect on the corrosion performance of alloys.

2.3 Pitting Corrosion

Pitting corrosion is a complex but an important issue for material degradation which is responsible for many corrosion failures. Pitting corrosion typically involves pit initiation stage, metastable pitting, and pit growth stage. In reality, pitting corrsion of stainless steels mostly takes place in neutral to acid solutions containing aggressive anions, such as Cl^-.

This makes the prevention of pitting corrosion of a great importance for the marine and some chemical processing industries [15]. In contrast to general corrosion, pitting corrosion results from the localized breakdown of passive film and occurs at discrete sites on metal surfaces. The localized attack starts on the surface, and can penetrate into the metal to very significant depths or even through-thickness failures for thin sections. Pitting corrosion is typically initiated by inhomogeniety of microstructure which causes passive film breakdown preferentially and local electrochemical cell formation which creates localized anodic/cathodic couples. Active pits can perforate through a metallic surface or become stress-concentration sites for stress corrosion or corrosion fatigue cracks to initiate [33, 91].

The pitting corrosion mechanism can be understood as a micromodel of the differential aeration cell [15]. According to this analogy, local film breakdown and pit growth creates the deaeration and the acidification inside the pit, which makes the pit a localized anodic zone. Yet, the perimeter of the pit becomes a localized cathodic zone through reduction of dissolved oxygen. The initiated pit creates a sheltered area, limiting the mass transport between the pit interior and the exterior solution. Analogously, pit growth is a localized active dissolution process, but limited by diffusion of ions between the pit interior and the exterior solution. In addition, many other factors can affect the growth rate of a pit. For example, it is proposed that with a proper $Cl^-/S_2O_3^{2-}$ ratio, thiosulfate ion can accelerate pit growth by enhancing anodic dissolution within the pit [92].

2.3.1 Pit Initiation

According to the adsorption model developed first by Kolotyrkin [93] and Hoar [94] for pit initiation, aggressive anions, for example, Cl^-, can be adsorbed onto the passve film, and replace oxide to loosely bond with metal cations and form complex compounds. This can greatly destablize the passive film and promote pit initiation. This model argues that the localized complex compounds are formed that promotes transport of metal cations across the interface between the oxide passive layer and the electrolyte. As a result, it causes thinning of passive films [95]. It then enhances the chance of breakdown of the passive films. Observations of Cl^- in the passive oxide layer using techniques such as X-ray photoelectron spectroscopy (XPS) and X-ray Absorption Spectroscopy in various alloy systems well supported this model, [34-37]. From the perspective of PDM, it is argued that the pit initiation is due to the accumulation of cation vacancies generated at the passive film/solution interface and transported to the metal/passive film interface, which eventually results in the localized breakdown of passive films [33]. Once a pit is initiated, it can be repassivated as a metastable pit, or it can continue growing as a stable pit. More details regarding the repassivation will be discussed in the next section.

As introduced in Section. 2.2.1.1, the microstructural inhomogeneity can promote pit initiation. One important deformation-influenced pit-initiation phenomenon is related to the presence of MnS inclusions. The MnS inclusion is one of the most common type of inclusions which can act as crack initiation sites [96] or pit initiation sites [97-99] in steels. Even though various mechanisms have been proposed to understand the MnS-promoted pit initiation, the consensus involving preferential dissolution of MnS as an initial step has been reached [97-99]. The MnS inclusion causes inhomogeneity of passive-film composition, where the passive film covering the local MnS area forms a Cr-depleted zone and thereby less protective. This gives rise to the preferential dissolution of MnS. One of the most accepted mechanism explains the further pit-initiation process as formation of crevice/trench between inclusion and material matrix. As MnS is dissolved into a corrosive environment, this creates a crevice structure adjacent to the inclusion. In addition, the dissolved S-containing products further enhance metal dissolution. Hydrolysis of the dissolved metal cations lowers the pH in this occluded crevice, further accelerating metal dissolution inside this geometry. This pit-like solution can be well sustained, because the crevice structure is relatively small, limiting ion transport between the crevice and the exteriors. The MnS inclusion is relatively large – at least in the micrometer level, and deformation often imparts some detrimental morphology changes to make it more prone to pit initiation. Cold-rolling can deform inclusions into stringers, and this enhances the chance of forming a crevice-like structure between inclusions and material matrix. Therefore, cold-rolling has been widely found to facilitate pit-initiation in aggressive environments for inclusion-containing stainless steels [97, 100]. Pits were found to preferentially initiate in trench areas between the MnS stringers aged in the air for different time periods and the material matrix as Fig. 2-13 shown [97]. It was found that aging the steel in the air for longer time helped to mitigate the susceptibility of the MnS stringers to pit initiation as a more protective oxide film formed to cover the MnS stringers. However, the negative effect of MnS straingers does not always hold true. A large degree of cold-rolling can fragment large MnS inclusions, so that inclusions possessing a refined morphology start to become less prone to pit initiation [100]. To put it simple, the susceptibility of inclusion to pit initiation depends on its chemical composition, morphology and size.

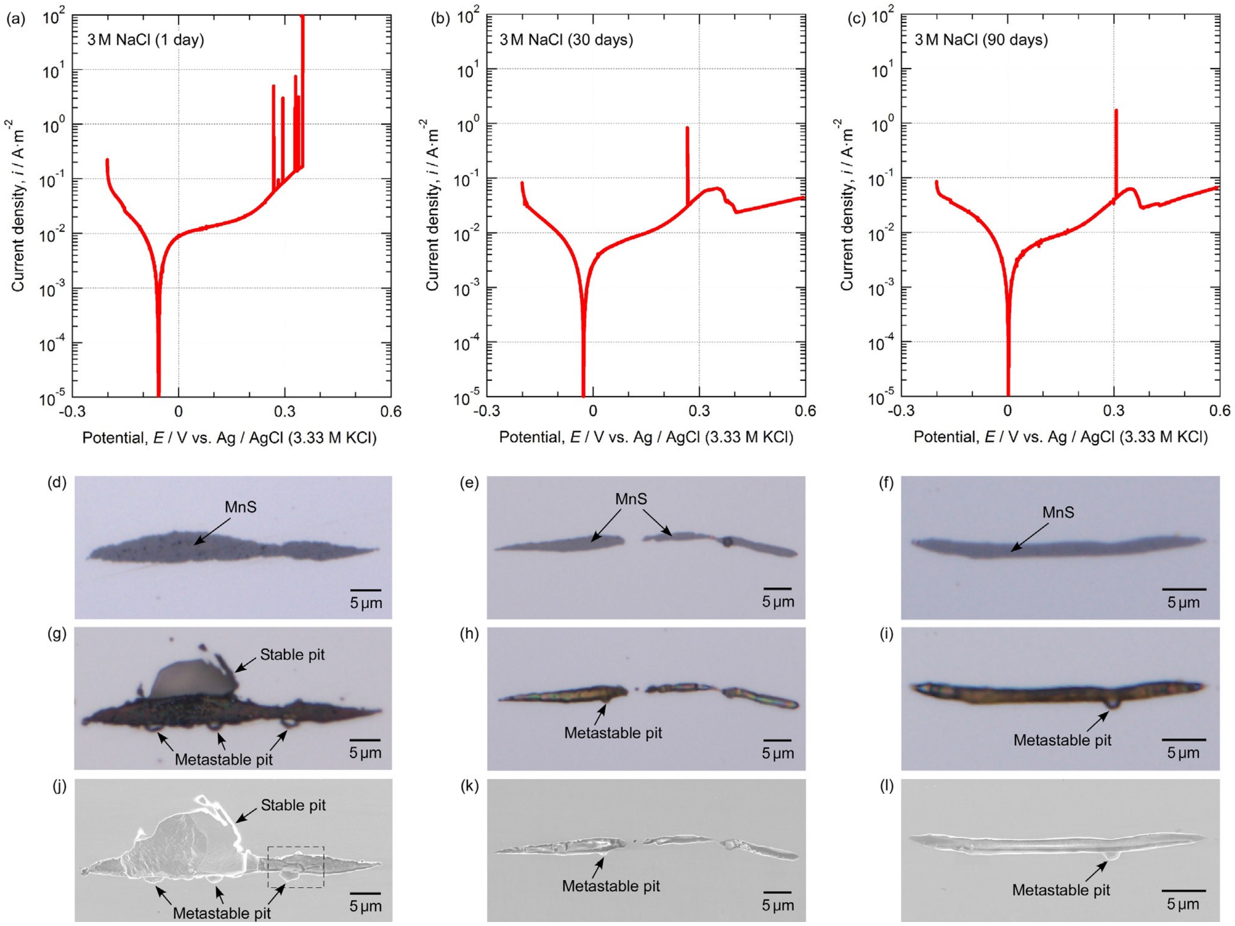

Figure 2-13. Preferential pit initiation near MnS inclusions in SS 304 aged in the air for 1 day, 30 days and 90 days from left to right respectively [97] .

With advanced modern steel making technologies, S content and other impurities are minimized in stainless steels. This makes MnS and other inclusions in the steels very rare and far less significant for pitting corrosion. It was then argued that local plasticity can promote the pitting corrosion. Plastic deformation such as cold-rolling in stainless steels can introduce a very significant amount of dislocations, twinning, and possible martensitic transformation in some alloy systems [2, 17, 20, 21, 23, 70, 101-104]. The additional strain energy due to cold-rolling are stored as internal stresses and these microstructural features. Thermodynamically, high-energy concentrated areas can act as anodic sites while the bulk material remains cathodic [105]. Gutman had theoretically calculated the potential changes as a function of deformation in the activation-controlled corrosion state [13]. Numerous researchers have shown the influence of martensitic transformation on pitting corrosion of stainless steels [2, 17, 21, 23]. No conclusive evidence has been demonstrated to show that the martensite had a direct effect on pitting corrosion, since the presence of martensite in austenitic stainless steels is always coupled with the presence of dislocation and twining. Twining structure in the steel was shown to exhibit lower potentials than the matrix materials in a 3.5 wt% NaCl solution, which could lead to potential difference in the galvanic couple formed between the twinned structure and the bulk metal [106].

2.3.2 Repassivation and Metastable Pitting

Repassivation behavior of an alloy is vital in the steel systems where the stability of the passive film is subject to many external factors, such as physical disturbances like erosion or electrochemical disruption. Repassivation can be referred in different scenarios: repassivation of an early pit and repassivation of a ruptured/broken film. For both cases, a fast repassivation kinetic prevents possibilities of developing a stable pit.

The causes for the rupture of passive films can generally be classified into two types: mechanical and chemical. Chemically, many environmental factors can destabilize passive films and cause local breakdown of the passive film, like chlorides and sulfides. Local breakdown of passive film exposes bare metals to the environment, making it locally anodic to the rest of the surface. This can give rise to pit initiation. Mechanically, passive films can be ruptured due to physical disruption or deformation. For example, many flowing chemical processes contain very hard particles. These chemical environments may not be aggressive enough to cause any damage to the passive films of metals, but collisions of hard particles onto metal surfaces can be strong enough to rupture the passive film. Two common techniques are typically used to simulate the breakdown of the passive film and study repassivation: scratch tests and mechanical straining. Scratch tests involve physically scratching the metal surface to cause film rupture by using a diamond scriber. Yushu Wang investigated the stability of passive films of various stainless steels in cautious chloride + thiosulfate environments by using scratch tests [90]. He found that thiosulfate inhibited film repassivation, resulting to premature metastable pitting and stable pitting. Another technique was introduced in Section 2.2.3 by straining the materials, so surface defects like slip steps migrate to the surface to cause film rupture. A failed repassivation can lead to occurrence of metastable pits and stable pits.

On the other hand, the pit-repassivation phenomena have been well studied in the past. A repassivated pit is referred as a metastable pit. Pit-repassivation of an alloy usually takes place where the passive film is unstable. Metastable pits are indicated by anodic current transients in a potentiostatic tests. Typically, the current transients show a positive correlation of current, I, and square root of time, $t^{1/2}$ at low potentials [91]. At high potentials, the correlation trends toward I ~ t or I ~ t^2 [91]. It was also observed that pits developed at low potentials often propagate with a pit cover at least at the early stage, referred as lacy pits [107]. However, more pits were observed at high potentials, probably due to the resultant high current at high potentials. In the growth of a lacy pit, dissolution inside an undercut pit cavity was usually observed with a porous passive film covering the pit opening [107]. This porous cover acts as a diffusion barrier, preventing pits from repassivating. Frankel et al. discovered that the current density of a pit with a pit cover in stainless steels increases as r_{pit}^2, where r_{pit} was defined as the radius of the pit [108]. The author further suggested that the current density was constant during pit growth and increased with applied potentials. It can be concluded that the pit growth under a pit cover was ohmic controlled. As a metastable pit grows, the pit cover often breaks down, and therefore pits have better chances to repassivate. Frankel et al. also investigated the kinetics of metastable pitting in chloride-containing environment environments and found that the metastable pitting can take place at a potential as low as -210 $mV_{(SCE)}$ in near neutral to acidic conditions [108]. It was also found that breaking of the pit cover did often lead to repassivation of a pit. Not all metastable pit occurrence involves the presence of a pit cover. Williams et al. established a criterion using I/r_{pit}, and applied this ratio to predict the stability of pits [109]. He found that pits usually grow stably when $I/r_{pit} > 40$ mA/cm, and repassivated below this value. The rationale behind this approach was that a high I/r_{pit} ratio indicated a lower pH inside the pit solution, help to sustain active dissolution during pit growth. As argued previously, the strain energy is suspected to accelerate the active dissolution by providing an additional driving force. This can lead to more prominent metastable pitting occurrence and higher possibility of stable pitting. Feng et al. found that metastable pits possessed longer survival time which resulted into secondary metastable pits on deformed SS304 in 0.05 M NaCl solution at 0.1 $V_{(SCE)}$ [110].

2.3.3 Stable-Pit Growth and Salt Film Stability

During the pit-growth stage, the cathodic reaction involving hydrogen revolution still take place inside the pit, but only contributing less than 5% of the overall cathodic reaction [111, 112]. Hence, it is reasonable to treat an entire pit as an anodic site, and the surrounding areas as an cathodic site. Once an initiated pit survives to reach the stable growing stage, hydrolysis of metal chloride products inside the pit leads to a drop in pH and migration of anions like Cl^- ions inside the pit which further accelerates the active dissolution inside the pit on alloys that show an active-passive behavior. This is called autocatalystic effect of Cl^- during pit growth. The resultant pH inside the pit can easily reach 0-2 for stainless steels [113, 114]. This localized acidification model was first proposed by Hoar in 1937 [115] and developed by numorous researchers [116, 117]. It was implied that a low pH needed to be maintained to sustain active dissolution within a pit cavity for stable-pit propagation. Based on this generic model, Galvele further developed an acidification model to model the pit growth process [118]. This model assumed that all metal surface films were defective, and the film defects like cracks could help initiate a pit. Since the hydrolysis reaction of metal cations inside a pit can result in a low pH for the solution inside the pit, Galvele calculated this the minimum degree of acidification through this hydrolysis to allow sustainable active dissolution according to metals' active-to-passive transition behavior. In this model, the ion diffusion/transport was assumed to be gorverned by the Fick's 1st law. It meant that the driving force for diffuison from the pit interiors to the electrolyte was simply dertermined by the concentration difference across the pit opening and the depth of the pit, x. Since the concentration difference can be tied back to the dissolution current of the pit, i_{pit}, therefore Galvele used $i * x$ as a criterion to determine if the acidification was strong enough to sustain a stable pit. This model was then further modified to account for the influences of potentials, concentrations of metal ions and chloride ions [119-123]. It is worth mentioning that a potential drop is possible from the pit bottom to the top, because IR drop can be significant in most pit-growth processes [114].

However, the acidification model did not provide sufficient insights to explain many other experimental observations in stainless steels [113]. It was found that the metal dissolution inside pits was often not under activation control. Instead, many researchers discovered that the diffuison barriers such as pit covers and salt films often controlled the diffusion process across the pit opening. A pit cover plays an important role during the early pit initiation stage. A key factor in the survival of a metastable pit to become a stable pit depends on whether it succeeds to retain a salt film after the pit cover breaks away [108, 124, 125]. A salt film can form near a corroding pit surface [114], comprised of metal hydrolysis products including metal hydroxides and metal chlorides. According to Belk and Alkire, pit solutions can become saturated and the salt film can form within $10^{-8} – 10^{-4}$ seconds of pit initiation [126]. While a salt film is stable and complete, the chemistry inside the pits should gradually stabilize. During the pit growth stage, it is commonly believed that a salt film is precipitated within the pit, which functions as a physical barrier and governs the diffusion process across the film[114, 126]. Therefore, the active dissolution inside pits during the pit growth stage are typically diffusion-controlled, rather than activation-controlled [108, 114, 124, 125]. This means that the dissolution inside a stable pit is independent of applied potentials.

Depending upon specific circumstances, the salt film can become unstable and break down especially during repassivation. This allows the activation-controlled active dissolution mode to take over until the pit interiors are completely repassivated. The repassivation mechanism following the formation of a salt film involves [113]: (1) alleviating pit current by thickening the salt film and depositing a passive layer underneath the salt, and (2) dissolution of the salt film and leaving the passivated layer on a metal surface.

The morphology and geometry of pits are often potential-dependent. Stable pits with flat walls were typically developed at low potentials [116, 127, 128], whereas high potential (significantly higher than pitting potential) resulted into hemispherical pits with dull or polished interiors [112, 116, 117]. In addition, stable pits typically possess a larger ratio of depth over diameter compared to metastable pits, since such geometries facilitate the trapping of pit solutions, hence hindering ion transport and sustaining a low pH.

2.3.4 Stochastic Nature of Pitting Corrosion

Pitting events are stochastic in nature, and the associated characteristics such as frequency and survival time are a function of materials and environments. Therefore, statistical approaches were developed to study pitting corrosion. Williams et al. [129] modeled the pitting process, and predicted the rate of stable pitting as:

$$f = A^*\lambda^*\exp(-\mu^*\tau_c),$$

where A is the area, λ is the randomly pit-initiation frequency, μ is the repassivation frequency and τ_c is the critical survival time for stable pitting. This model agreed well with experimental data by Balkwill [130]. This prediction went off significantly as materials were exposed in the test environment for longer time. This is because the passive film gradually stabilized as immersed in the test solution for longer time and the frequency of pit initiation decreased as a result. Yet, this proposed model did not account for the time-dependent stability of passive films. Another reason that may cause the decreased pit-initiation frequency was that there may be limited pit-initiation sites. The number of pit initiation sites were decreasing as the pitting process proceeded. Along with the similar statistical approach, new statistical models were developed to account for the influences of potential, scan rate, chloride concentration and so on [108, 131-138].

2.4 Gaps in Understanding Strain-influenced Pitting Behavior

So far, we have reviewed the potential influences of strain on corrosion reactions both under activation control and under passivation control. Even though much prior work has been done on associated topics, many pieces of knowledge are still missing in the general picture of interaction between the strain and different types of corrosion behavior. The ultimate goal of the present study was to fill in these knowledge gaps, and provide a systemactic and conprehensive understanding of the strain-influenced corrosion activities in various alloy/environment systems.

First of all, the strain-accelerated general corrosion, which is under activation control needs to be investigated over a complete deformation spectrum, including both elastic deformation and plastic deformation. Pertinent prior study was available in different alloy/environemt systems as discussed in section 2.1.2, but further connections is still waiting to be developed in steel systems over a broad investigation of different deformation types and mechanism. Thermodynamically, potential as an indicator of metal-oxidation tendancy has been overlooked in the past. Quantitative experimental evidences are still missing to confirm strain as an additional driving force for the accelerated dissolution in the cases where different forms of strain/stresses are either applied or are present as residual strains in steels. Hence, links can be made between reaction kinetics and thermodynamics in the setting of industrial applications.

Secondly, when steels are under stable passivity conditions, repassivation kinetics needs to be explored to investigate the role of strain in such a process. As discussed earlier, the traditional scratch test to study repassivation behavior of an alloy involves physically rupturing the film which creates local plasticity. This local plasticity becomes another ambiguity added to the original strain/deformation in the alloy systems. Therefore, an new method is needed to study the repassivation kinetics without physically rupturing the film. An alternative way to study repassivation is to employ an electrochemical method, which reduces the oxide film and exposes the bare metal by applying an proper negative potential in an appropriate pH range for sufficient time.

Lastly, the effect of strain on pitting corosion and pit-repassivation kinetics requires a systematic investigation over various types/mechanism of deformation/strain. No work has addressed the influence of elastic stresses on pitting behavior of stainless steels before. Therefore, the associated effect and mechanism need to be explored. Numerous reserachers have studied the effect of plastic deformation on pitting corrosion, achieved mainly by using tensile deformation and cold-rolling [1, 3, 23, 100, 102, 104, 106, 139-143] . However, some of these prior results contradicted with one another, and a generic governing mechanism is lacking. In addition, no study explicitly discussed the contribution of the elastic portion of stresses when in-situ plastic deformation is applied. With the results and findings of this thesis, the above-mentioned knowledge gaps will be bridged and the associated contradictions/ambiguities in prior work will be resolved.

CHAPTER 3. MATERIALS AND METHODS

3.1 Materials

Two iron-based alloys were selected for different purposes of testing: carbon steel A569 and austenitic stainless steel (SS) 304. The activation-controlled general corrosion was studied using CS A569. Stable repassivation investigation was also performed on CS A569 in alkaline solutions. SS 304 was selected to study the effect of strain on localized corrosion, pitting corrosion and pit repassivation. Below are the chemical compositions of the three steels.

Table 3-1. Chemical composition of carbon steels A569 and SS 304.

Element (wt%)	Fe	Mn	C	P	S	Si	Mo	Cr	Ni
A569	Bal.	0.26	0.06	0.014	0.04				
SS304	Bal.	1.72	0.056	0.03	0.001	0.21	0.36	18.34	8.1

3.2 Deformation Techniques

The deformation techniques utilized in this study can be categorized as in-situ techniques and ex-situ techniques. The in-situ loading technique employed a slow strain rate test (SSRT) machine. To be connected to the SSRT rigs, flat tensile specimens were machined with a narrow gauge, where the corrosion tests were performed. A schematic of a representative tensile specimen is shown in Fig. 3-1. The top and the bottom of the specimen were connected to the SSRT rigs through non-conducting ceramic pins. Tensile sample was electrically isolated from the test-rig. To perform electrochemical tests on these tensile specimens, a three-electrode system was assembled as shown in Fig. 3-2 [73]. As color-coded in Fig. 3-2, the tensile specimen (blue) was the working electrode; the saturated calomel electrode (green) was the reference electrode; and the counter electrode (a platinum plate) was color-coded as yellow. Air was bubbled in and out of the system through the gas inlet and outlet.

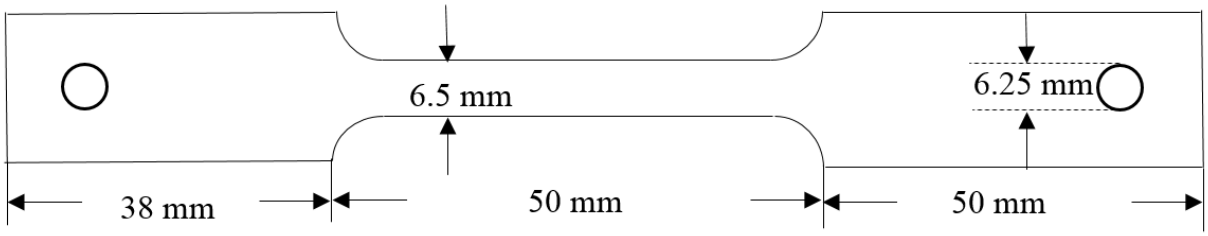

Figure 3-1. A schematic of the CS A516 tensile specimen.

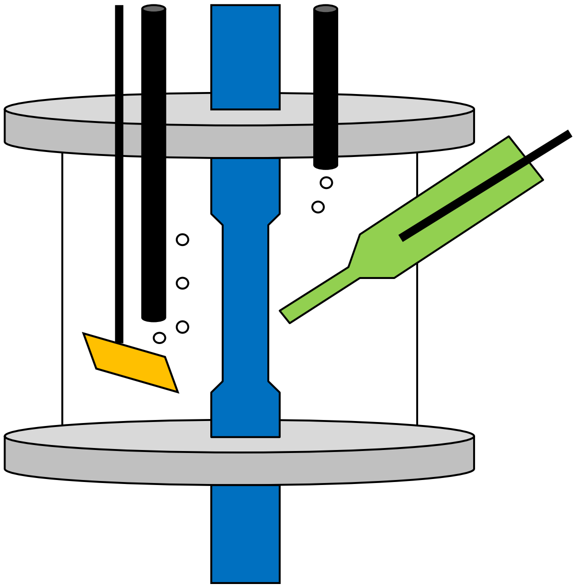

Figure 3-2. A schematic for the experiment setup of SSRT.

As an in-situ deformation technique, the SSRT machine was programed to apply a constant strain level to the specimens and to hold the strain level throughout the tests. To determine the regimes for elastic deformation and plastic deformation, a tensile test was performed on both CS A569 and SS304. Fig. 3-3 and Fig. 3-4 shows the stress vs strain curves for CS A569 and SS304 in as-annealed conditions, respectively. With the help of the mechanical behavior data shown in the two graphs, stresses/strain in further tests could be precisely controlled in either elastic or plastic range. More analyses on the mechanical behavior of CS A569 and SS304 would be presented in the upcoming chapters when their associated corrosion performance is discussed.

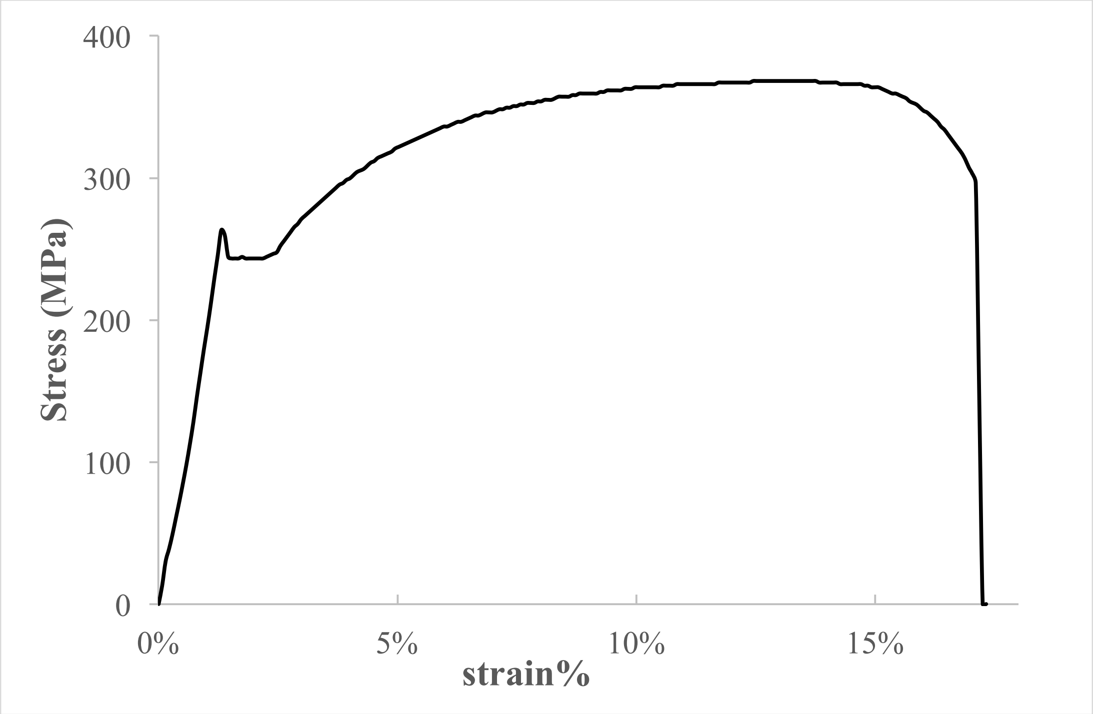

Figure 3-3. Stress vs. Strain curve for CS A569.

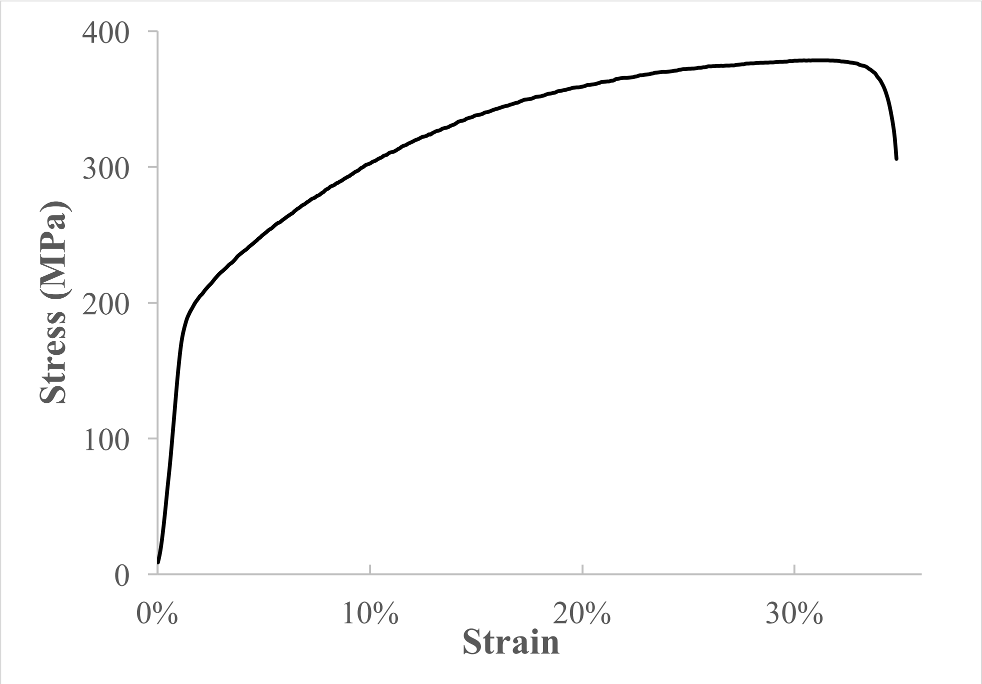

Figure 3-4. Stress vs. Strain curve for CS A569.

As for ex-situ deformation techniques, both SSRT setup and cold-rolling were used. With SSRT method, specimens were deformed to selected strain levels in the plastic range as indicated in Fig. 3-3 and Fig. 3-4. The strain was held at the specific strain level for 10 minutes and then the sample was unloaded. The resultant surfaces were carefully preserved for further electrochemical testing. Cold-rolling was the other ex-situ deformation technique utilized in this thesis. During a cold-rolling process, samples were rolled through two cylindrical wheels to obtain a reduced thickness. The final thickness of the samples can be accurately controlled by controlling the gap distance between the two wheels as depicted in Fig. 3-5.

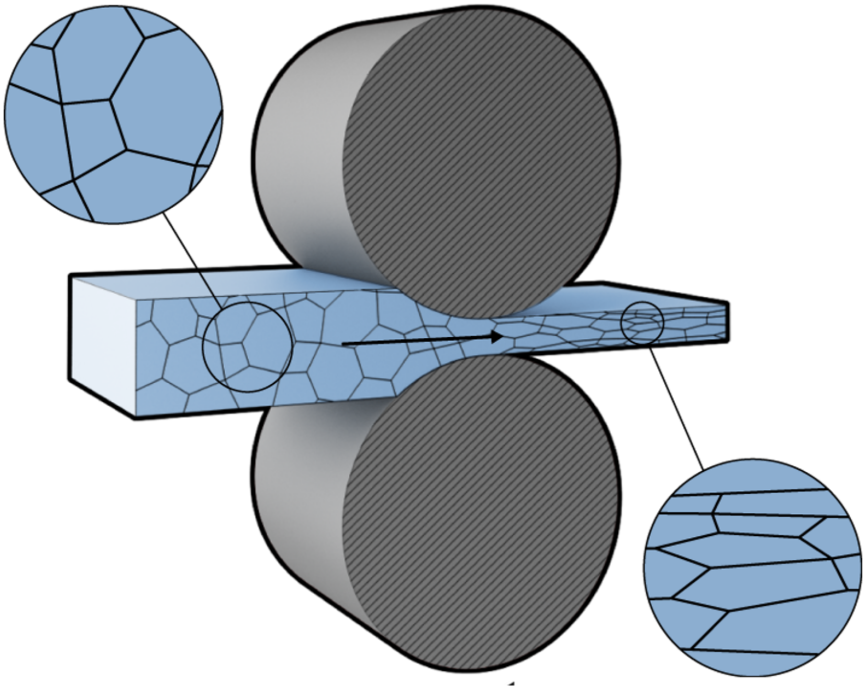

Figure 3-5. A schematic of a cold-rolling process.

All the cold-rolled specimens were mounted in an epoxy mold and polished to 2000 grit prior to any electrochemical test. Precautions were taken to minimize surface cold-work introduced during the preparation and polishing of specimens for corrosion tests. A punched electroplating tape was applied to the sample surfaces, leaving a hole of 5 mm diameter as the testing surface. For all the tensile specimens, the gage was polished to 2000 grit finish. All the specimens were carefully insulated from rest of the test rig and cell by using a polyurethane spray, purposely leaving a hole of 5 mm diameter as the testing surface.

3.3 Activation-Controlled General Corrosion Tests

Carbon steel A569 were selected for general corrosion tests. As-received CS A569 samples were annealed at 850 ^{o}C for 1 hour to remove residual stresses and then water-quenched. Both SSRT and cold-rolling were used to apply different levels of stresses/strain to the carbon steel specimens prior to the general corrosion test.

Based on the different deformation techniques used, sample preparation was also adjusted to better preserve the surface conditions after deformation. The sample preparation for cold-rolling followed a sequence: cold-rolling, mechanical polishing up to 2000 grit, ultrasonic cleaning in ethanol and applying insulation on the non-testing area. The sample preparation for tensile samples followed the following sequence: mechanical polishing up to 2000 grit, ultrasonic cleaning in ethanol, applying insulation on the non-testing area and applying tensile stresses/strain using SSRT. The reason that cold-rolled samples needed to be polished after deformation was because the impurities and debris were imbedded onto the sample surfaces after cold-rolling. These surface imperfections could interfere with the corrosion tests, therefore had to be removed using polishing.

Two methods were selected to assess the rate of general corrosion for CS A569: immersion test and linear polarization resistance (LPR) test. For the immersion test, the specimens were immersed in a 2 M sulfuric acid for 24 hours. The sulfuric acid solution selected for these tests allowed the materials to completely break down the native oxide film on the surface, because the oxide layer was unstable in low pH conditions. Once the bare metal was exposed to the acid solution, the metal oxidation reaction took place,

$$Fe - n\,e^{-} \rightarrow Fe^{n+},$$

where n is the number of electrons transferred in this reaction. The weight of each specimen was measured before and after the test, and the weight loss was calculated after the test.

For the linear polarization resistance (LPR) test, the three-electrode system was used. The potential was scanned 10 mV below and above the open circuit potential (OCP) with a scan rate of 0.125 mV/s. A typical linear LPR curve is demonstrated in Fig. 3-6. The slope of the curve can be calculated using software like Excel. The slope, $\frac{dE}{di}$ is a function of corrosion current i_{corr} [15]:

$$\frac{dE}{di} = \frac{\beta_a * \beta_c}{2.3 * i_{corr} * (\beta_a + \beta_c)}, \qquad 3.1$$

where E is the potential applied to the metal, i is the current density resulted from the applied potential, i_{corr} is the corrosion current density, and β_a, β_c are the anodic Tafel slope and the cathodic Tafel slope, assumed to be 100 mV/decade. In doing so, the corrosion current density, i_{corr} can be calculated. This calculated corrosion current density can further be converted to corrosion rate, R in the unit of mil per year (mpy) using the equation below [15]:

$$R = 0.129 * \frac{M * i_{corr}}{n * \rho}, \qquad 3.2$$

where M is the molar mass of the metal, n is the charge of the metal cation, and ρ is the density of the material.

Since LPR is not a destructive method and does not require long testing time, it becomes a feasible in-situ technique to evaluate the rate of general corrosion compared to the immersion test.

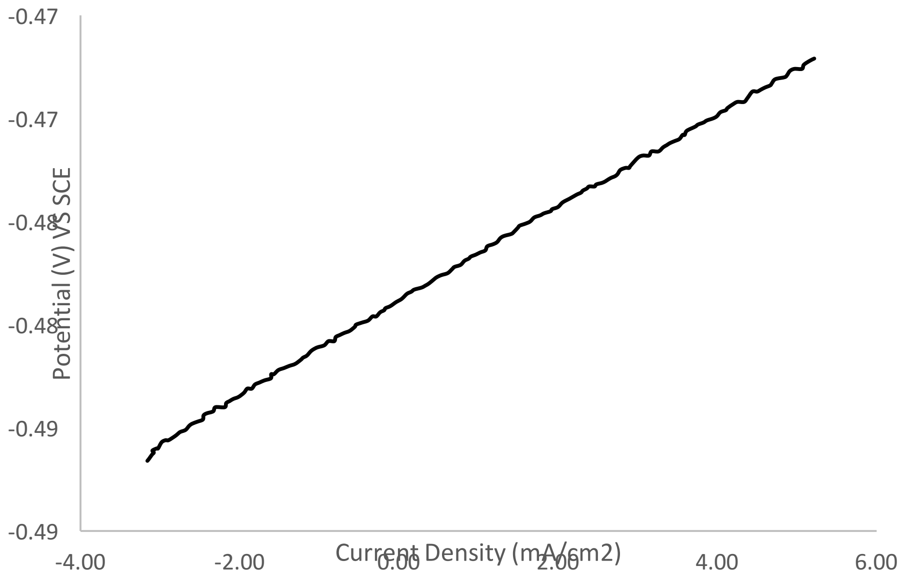

Figure 3-6. A typical current response as a function of potential in a LPR test.

3.4 Stable Repassivation Tests

As discussed earlier, an electrochemical method was used to reduce surface oxide layer so that repassivation behavior could be investigated on bare metal. In this method, the specimen was reduced at -1V$_{(SCE)}$ for three hours, and immediately anodically polarized at a well-passivated potential. A chronoamperametry tests were used to monitor the repassivation current since this technique is more sensitive to short-time data acquisition. To better analyze the repassivation currents, Lillard's model was utilized to simulate the repassivation kinetics. Lillard's model [144] was developed by R.S. Lillard, and it breaks down repassivation current I_{total} into dissolution current I_{diss} and film passive current I_{film}, as is given by the following equation.

$$I_{total} = I_{diss} + I_{film} = (1 - \Theta) * I_{bare} + \Theta * A * t^{-b} \quad 3.3$$

where I_{bare} is the very initial dissolution current of bare metal roughly taken as the first current recorded, Θ is fraction of surface covered by a passive film, $\Theta = 1 - \exp(-k * t^{-n})$, and A, b and n are constants which need to be computed by a computer program accordingly. A matlab code was written to fit the repassivation currents, and hence fraction of completion Θ vs time plot could be further derived.

3.5 Cyclic Potentiodynamic Polarization Tests

One of the most common electrochemical techniques to assess the pitting resistance of alloys is the cyclic potentiodynamic polarization test. Stainless steel 304 was used for all studies of pitting corrosion in this thesis. In the cyclic polarization tests, a three-electrode system was used to control the potential and to monitor the current response. The potential of the alloy was scanned over a range given by the user in a specific environment and temperature. The applied potential is essentially the thermodynamic driving force for an electrochemical reaction, while the resultant current reflects the kinetics of the electrochemical reaction at a given potential. Fig. 3-7 demonstrates a typical cyclic potentiodynamic polarization curve [145].

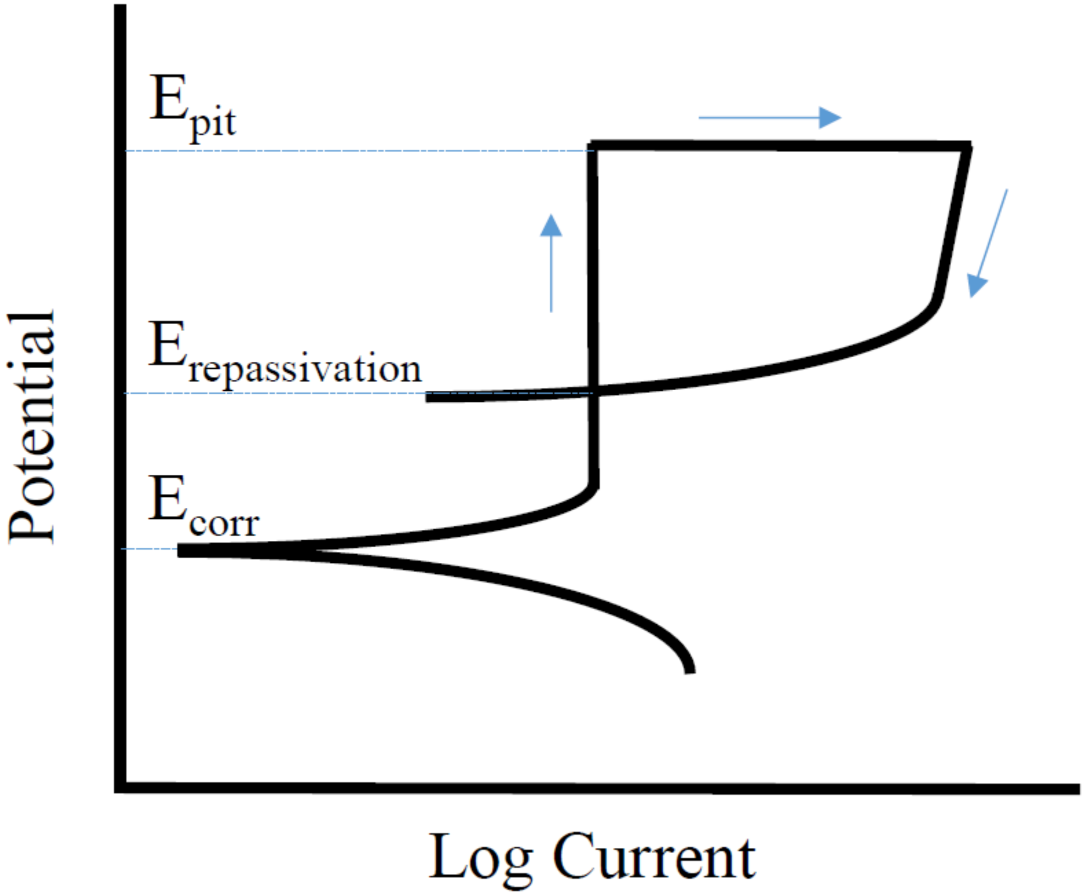

Figure 3-7. A typical cyclic potentiodynamic polarization curve for a metal exhibiting passivity [90].

As the potential is scanned in forward direction (+ve direction), the corresponding current enters a cathodic regime first and then a short range of activation-controlled anodic regime, separated by the corrosion potential, E_{corr} as indicated in Fig. 3-7. It is followed by an active-passive transition, where the passive film forms at the metal surface and the reaction starts to stabilize at a relatively small current value. Upon further increase in the applied potential, the passivity eventually breaks down indicated by a sudden increase of current at the pitting potential, E_{pit}. A pitting event takes place at this potential because of the localized breakdown of passivity. Once the current reaches a set limit, the potentiostat is programmed to scan the potential backwards (-ve direction) until it intercepts with the forward scan curve or the passive current value at the repassivation potential, $E_{repassivation}$.

3.6 Potentiostatic Polarization Tests

Different from the potentiodynamic test, the potentiostatic test applies a constant potential to the materials to stimulate any electrochemical reaction at that potential value. Therefore, the potentiaostatic test can determine the stability of the materials at a given potential over a long period of time. A carefully designed series of potentiostatic tests at different potentials were utilized to satisfy unique testing purposes.

3.6.1 Stability of Metastable Pitting to Stable Pitting Transition

In this set of tests, a potential was carefully selected to evaluate the stability of metastable pitting to stable pitting transition. Therefore, this selected potential was in the passivation range, slight closer to the pitting potential. By applying this constant potential to SS304 strained to different levels, characteristics and details on the transition from metastable pitting to stable pitting were revealed by using strain as a variable. Multiple tests were done under the same test conditions, and further statistical analyses was done to check the reproducibility of results from these tests.

3.6.2 Pit-Repassivation Kinetics

A single pit was induced by applying a (+)300 $mV_{(SCE)}$ to the SS304 sample. Current was stopped at +40 uA for the 304 specimens with different applied stresses/strain levels as shown in Fig. 3-8. The steep anodic current transient represented that a pit had initiated. Two sets of experiments were proceeded immediately following the pit initiation. The first one was potentiostatic tests at +250 $mV_{(SCE)}$ to determine the stability of pits developed under different stresses/strain as indicated in Fig. 3-9. This experiment allowed the initiated pit to repassivate or grow when a lower constant potential was applied to the sample. In the second experiment, following the pit initiation a reverse polarization test was performed by changing the potential from +300 $mV_{(SCE)}$ to 0 $mV_{(SCE)}$ at a scan rate of 5 mV/s as indicated in Fig. 3-10. This allowed the initiated pits to undergo repassivation over a large potentiodynamic range. By comparing the results from these two versions of pit-repassivation experiments, important insights could be gained by understanding the pitting behavior of SS304 in the transition between metastable pitting and stable pitting under the influence of stresses/strain.

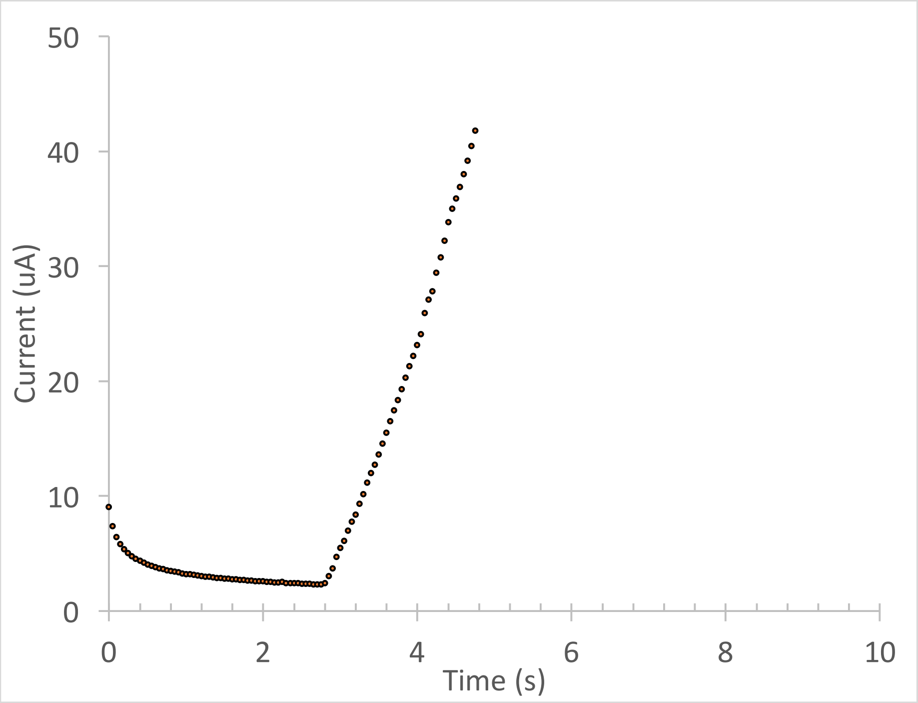

Figure 3-8. A representative current transient during the pit initiation test in 0.1 M NaCl at 50 °C.

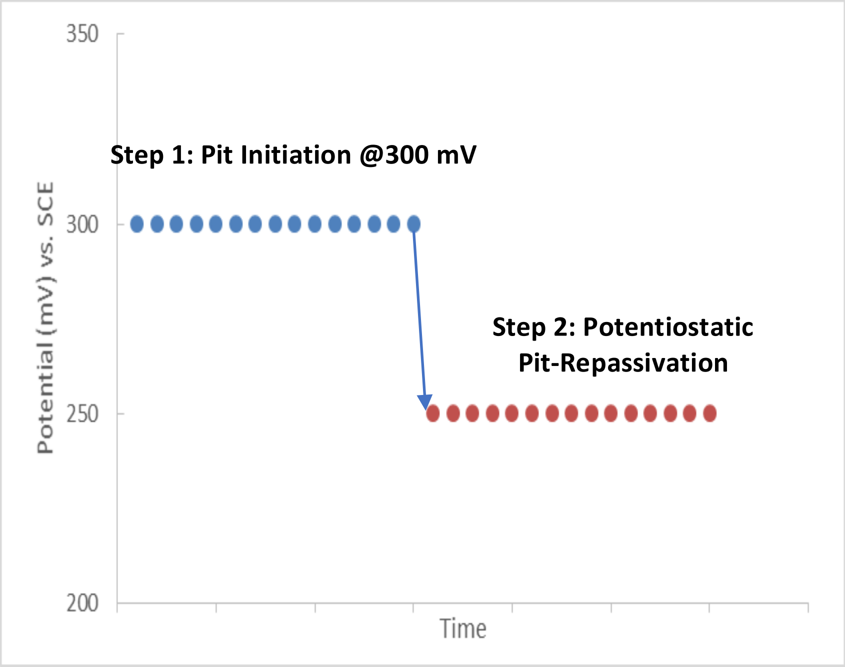

Figure 3-9. Potentiostatic pit-repasivation.

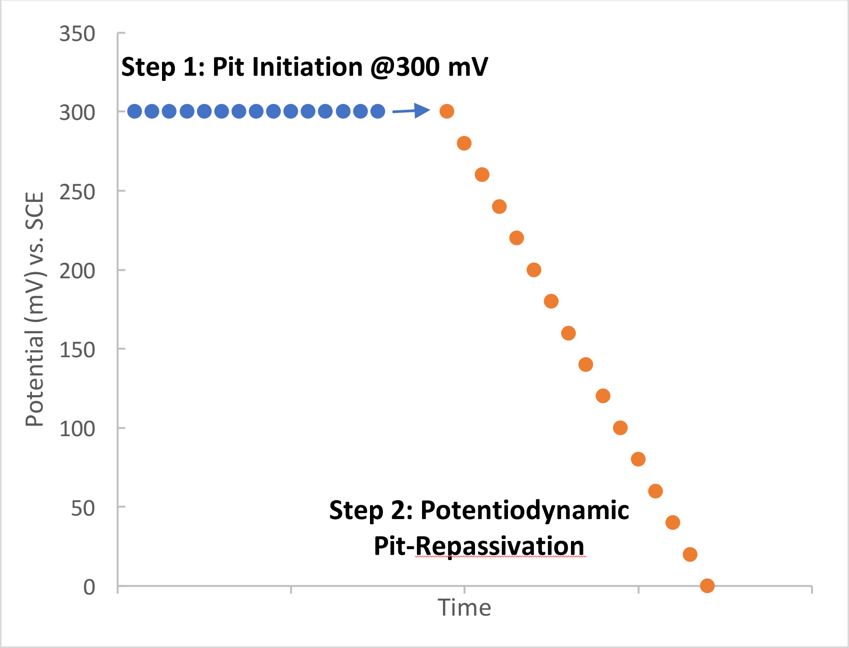

Figure 3-10. Potentiodynamic pit-repassivation.

To confirm the initial formation of the pit at (+)300 mV$_{(SCE)}$, the pit profile was determined by using a non-contact laser profilometer. Once the pitted surfaces were obtained through applied potential, surfaces were ultrasonically cleaned with acetone, and then profilometry measurements were performed. All profilometry scans utilized a dual-frequency optical measurement (200Hz and 1000HZ) to obtain 3-D pit geometries with a resolution of 0.3 um. To avoid interference between multiple pits during the pit growth stage, only the data generated from the surfaces with a single-pit in the exposed surfaces were selected. The resultant 3-D pit geometries were shown in Figure 3-11.

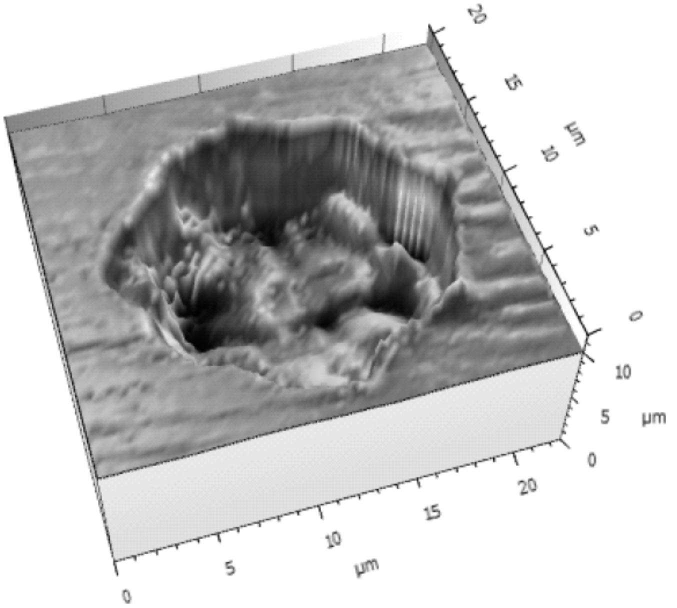

Figure 3-11. 3-D 40uA-pit geometries developed at +300 mV$_{(SCE)}$ over different stress/strain levels.

Cylindrical pits were developed and the diameter to depth ratio for cylindrical pits was around 1.5. The volume of the pit was also calculated to be roughly 1,110 um^3. This 3-D geometry was very reproducible over different applied stress/strain levels. This suggested that the amount of metal corroded inside the pits on two different samples was relatively close. Therefore, the low pH inside the pits caused by metal cation hydrolysis should also be similar in these two cases. It ensured that the further pit growth step was proceeded in similar 3-D geometries and chemical environments.

3.7 Surface/Materials Characterization

Etching was used to reveal the microstructure of alloys. Depending on the alloy and need to reveal different microstructures, various etching methods were used to identify the associated microstructural features. In this thesis, three etching techniques were used: Nital etching, color etching, and electrochemical etching. A Nital etching solution dissolving 10 wt% nitric acid in ethonal was used to etch CS A569. A 10 wt% oxalic acid dissolved in water was used to perform electrochemical etching on SS304. The SS304 specimens were polarized at a constant potential of +20 Volts in the 10 wt% oxalic acid for ~60 seconds. It helped in revealing the grain boundaries, twins and potential martensite. As discussed in the previous chapter, the MnS inclusion could impart a detrimental second phase during the pitting process in stainless steels. The SS304 used was a very clean grade and expected to be free of MnS inclusions. The Berahaa's CdS tint etchant [146] described in Table 4-1, was used to confirm the absence of MnS inclusions. The Berahaa's CdS tint etchant selected here was an immersion color etchant. It can deposit a colored film on sulfide compounds through a complex redox reaction and stain the sulfide-film red-brown. It is recommended to dissolve the chemicals in the order shown in Table 4-1 from left to right, age the solution for 24 hours, and finally filter 100 mL for the experiment uses. The suggested immersion time for stainless steels is >90s.

Table 3-2. Chemical composition of the Berahaa's CdS tint etchant.

Chemicals	Water	$Na_2S_2O_3 \cdot 5H_2O$	Citric acid	$CdCl_2$
Weight (g)	1000	240	30	20-25

Characterization of a passive film involves an investigation of chemical composition of passive films. X-ray photoelectron spectroscopy (XPS) is a surface-sensitive quantitative spectroscopic technique that can be used to measure the chemical composition of materials at or near-surface level. Depending on the materials and parameters used, XPS provides the average chemical composition information with depth < 5 nm, so it was used to investigate the chemical composition of the passive film developed on SS304 with different surface treatment. Three spots were examined on each specimen, so that an average chemical composition can be calculated. A spot size of 300 μm was selected to obtain information over a relatively large area on each spot. The information pertaining to the surface chemical composition can be further linked to the associated corrosion behavior.

Optical microscopes, scanning electron microscope (SEM) and the non-contact profilometer introduced in Section. 3.6.2 were used to characterize the pit morphology and the microstructures with/without etching. X-ray diffraction (XRD) was also employed to evaluate phase compositions of different alloy systems and residual stress levels. The equation below is used to calculate the residual stress, σ_φ of a strained surface using XRD [147]:

$$\sigma_{\varphi} = \left(\frac{E}{1+v}\right)_{(hkl)} \frac{1}{d_{\varphi}} \left(\frac{\partial d_{\varphi\psi}}{\sin^2\psi}\right) \qquad 3.5$$

where φ and ψ define the angle of residual strain, φ is parallel to the surface, ψ is perpendicular to the surface, d_{φ} is the interplanar spacing in the φ direction, E is the elastic modulus, v is the Poisson's ratio and $d_{\varphi\psi}$ is the interplanar spacing under strain measured by XRD.

CHAPTER 4. EFFECT OF DEFORMATION ON GENERAL CORROSION

General corrosion is typically an activation-controlled chemical reaction. Under the scope of thermodynamics, strain energy can provide an additional driving force for the reaction. Such strain-accelerated general corrosion was commonly observed in many engineering applications. Fig. 4-1 depicts a pile of carbon steel bars which underwent an accelerated general corrosion in the bent area where the strain is concentrated. For metals to undergo general corrosion, Pourbaix diagrams can give a good indication on the necessary conditions, such as potential and pH for general corrosion to occur.

Figure 4-1. Accelerated general corrosion in the area of bending.

In this chapter, we utilize different deformation techniques namely tensile deformation and cold-rolling over both the elastic and the plastic deformation range. The interaction between different forms of deformation and general corrosion is examined. The corrosion rate and the corrosion tendency is evaluated and estimated by using different electrochemical techniques.

4.1 Effect of Elastic Stresses on General Corrosion

4.1.1 Active Dissolution in Immersion Tests

The stress vs. strain curve for the annealed carbon steel A569 was shown in Fig. 3-3. The yield stress of annealed A569 is roughly 262 MPa. A set of 24-hour immersion tests in a 2 M H_2SO_4 solution at 50 ^oC was performed at different levels of elastic stresses. Four applied stress levels were selected to be 0 MPa (no stress), +55 MPa (tension), +110 MPa (tension) and +220 MPa (tension). The spectrum of this selected stress range fell into the elastic regime and did not induce any plastic deformation. The weight before and after the immersion test was measured for specimens loaded at each stress level, and the corresponding weight change was used to determine the corrosion rate (CR), reported here in mils per year (mpy) by accounting for the density and exposed area for each sample. Each test was repeated twice and the average corrosion rates (CRs) of CS A569 were plotted as a function of applied elastic stresses along with the standard deviations as shown in Fig. 4-2. It is observed that the corrosion rate is directly proportional to the applied elastic stresses, ranging from 5123.7 mpy to 5861.2 mpy. The maximum corrosion rate occurred at the maximum stress level, +220 MPa, which was about 12% above the baseline corrosion rate when no stress (0 MPa) applied.

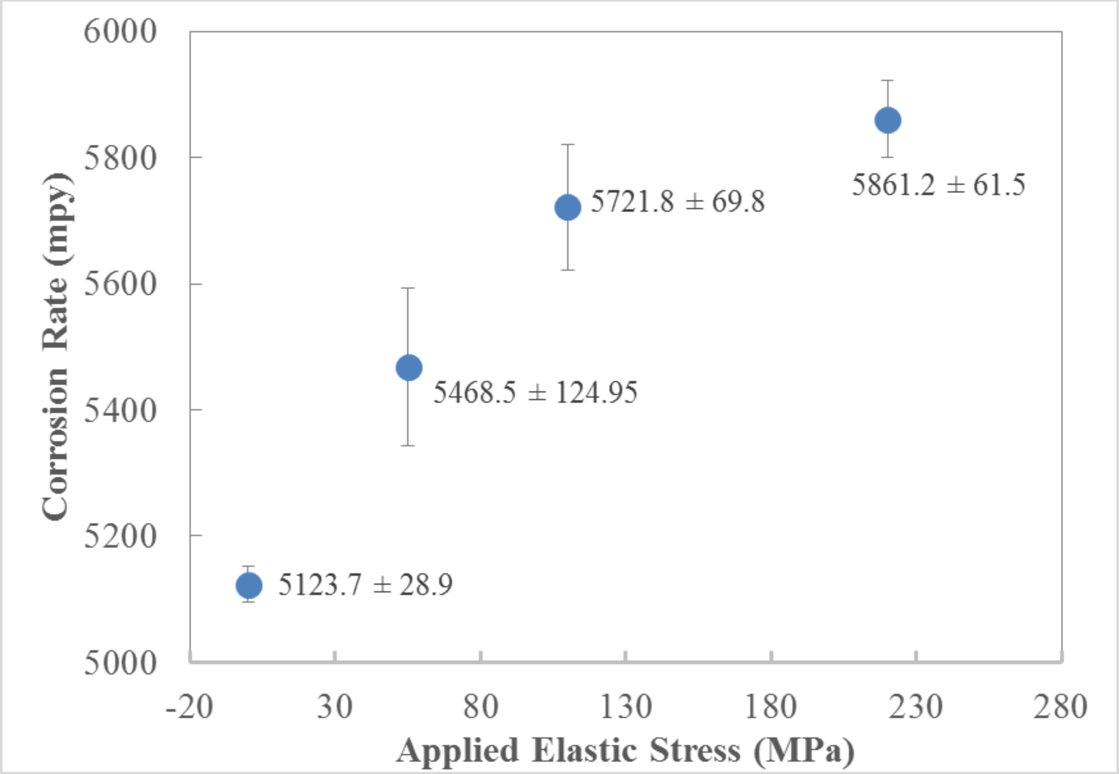

Figure 4-2. Average corrosion rates (CRs) calculated from the immersion tests as a function of the applied elastic stresses in a 2 M H_2SO_4 solution at 50 ^{o}C.

The relative corrosion rate was calculated as

$$Relative\ CR = \frac{CR\ @\ a\ specific\ stress/strain\ level}{CR\ @\ baseline}, \qquad 4.1$$

where CR at baseline was the corrosion rate when no stress/strain applied. Fig. 4-2 was then re-plotted using the relative corrosion rates as shown in Fig. 4-3. A linear trend line was added based on the data. Experimental data shows a linear correlation between the corrosion rate and the elastic stress.

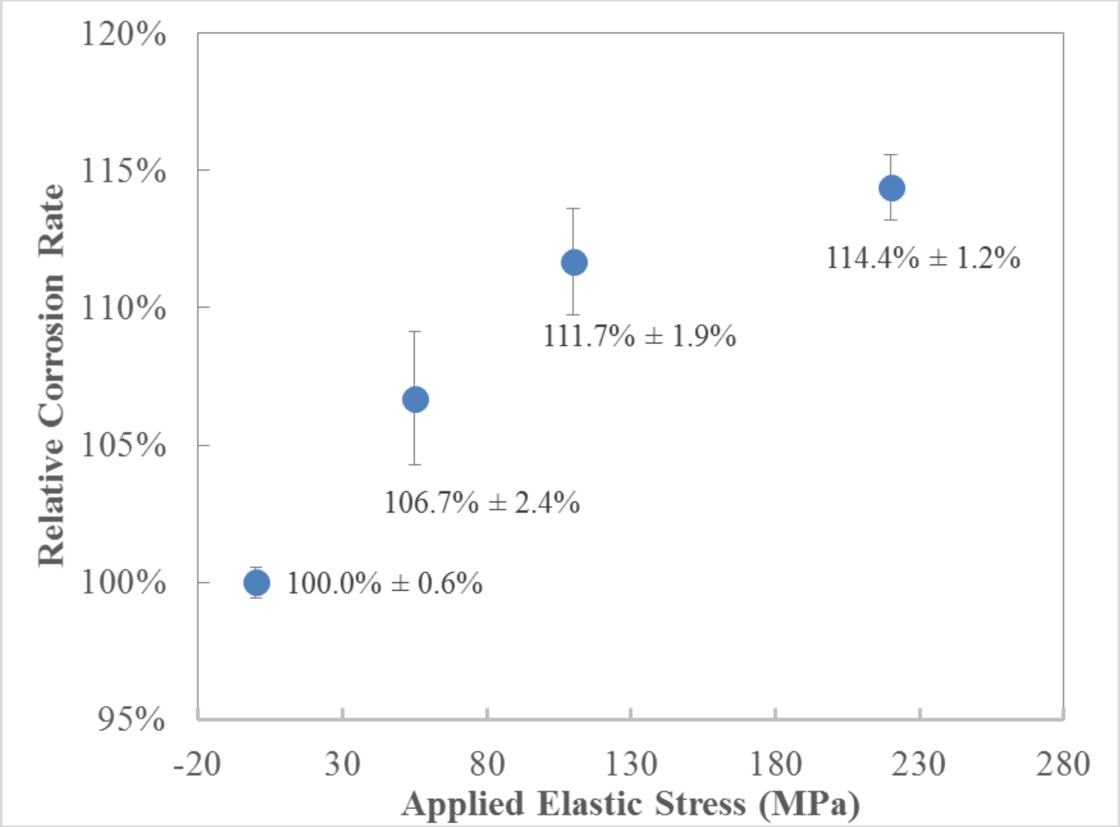

Figure 4-3. Average relative corrosion rates (CRs) calculated from the immersion tests (two repetitions for each stress level) as a function of the applied elastic stresses in a 2 M H_2SO_4 solution at 50 °C.

4.1.2 OCP Evolution and Derived Relative Corrosion Rates from OCP Changes

The open circuit potential (OCP) was also monitored throughout the immersion test for each applied stress level as shown in Fig. 4-4. The OCP underwent an anodic shift in the early stage and gradually stabilized after 5 hours. This reflected that the initial active dissolution on the metal surfaces did not reach a steady state immediately. This is probably because the native film was being dissolved and the corrosion products were slowly built up in the early stage.

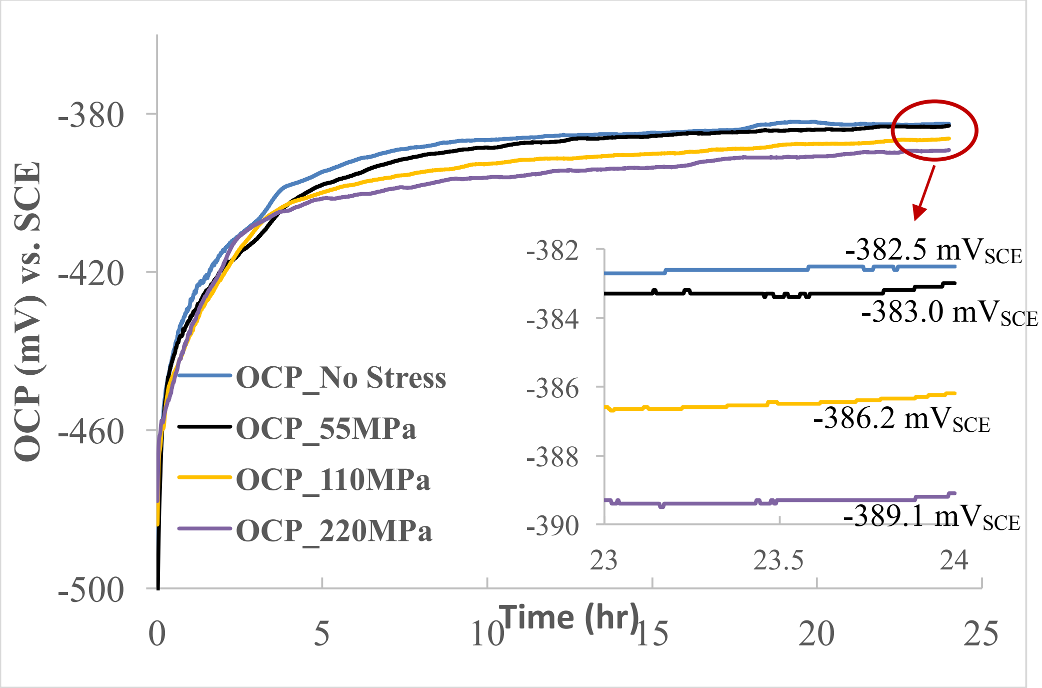

Figure 4-4. OCP evolution of CS A569 at 4 different stress levels (no stress, 55 MPa, 110 MPa and 220 MPa) during 24-hour immersion in a 2 M H_2SO_4 solution at 50 ^{o}C.

A zoom-in view of the OCP evolution in the last hour of the test was embedded in the right bottom of Fig. 4-4. The exact OCP values ranging from -382.5 $mV_{(SCE)}$ to -389.1 $mV_{(SCE)}$ were marked near the corresponding OCP curve in the Figure. It was clear that the OCP in the end of the test was stabilized at a lower value as the applied stress increased. A more negative OCP indicates a stronger oxidation tendency and a faster dissolution rate for the same material. Therefore, OCP can be a thermodynamic indicator for a relative driving force for the reaction and be a kinetics indicator for a relative corrosion rate. The OCP changes were relatively smaller, though the trends were very clear. To further analyze the correlation between the strain-induced corrosion rate and the resulting OCP, theoretical calculations were done. According to the Nernst equation, the relative corrosion rate (CR) can be calculated from the OCP differences by assuming that the effect of strain is only on the anodic reaction, therefore the cathodic Tafel slope, β_c is fixed to be 67 mV/decade. Therefore, the relative CR can be derived using to following equation

$$Relative\ CR = exp\ (\frac{E' - E_0}{\beta_c}), \qquad 4.2$$

Where E' is the stabilized potential at the end of the immersion test, and E_0 is the stabilized potential for the no-stress CS A569 sample. The relative CR was plotted as a function of the applied stress in Fig. 4-5. The relative CR curve obtained from the weight loss measurements was added for comparison. Similar to the trend observed in Fig. 4-3, another positive correlation between relative corrosion rates and stresses was seen, indicating that this CR derived from the OCP changes agreed well with the CR data obtained from the immersion tests.

Despite the similarities in the rising trend and the turns at 55 MPa and 110 MPa between the two curves, it is obvious that the relative CRs obtained from the weight loss measurements was slightly higher than the ones derived using the OCP data. This difference could rise for a couple of reasons. First, the OCP changes were calculated in the end of the immersion tests, so this estimation reflected the relative CR more towards the end of the test. However, the results calculated directly from the weight loss measurements were responsible for the average CR throughout the entire test. In addition, the anodic OCP shift in the early stage of the immersion tests hinted a strong active dissolution in the beginning. This may be the reason that causes a slightly higher CRs obtained in the weight loss case compared to the ones derived from OCP data. Second, OCP is the interception of the metal anodic reaction and the hydrogen cathodic reaction as explained in Section 2.1.2. The derivation of the relative CR was performed under the premise that the hydrogen cathodic stayed unchanged for the same material regardless of the stress levels. However, it may not hold true, since the catalytic activities of metals be altered by strained [30, 32]. This may result in a change of the cathodic Tafel slope or a shift of the cathodic reaction potential. Such ambiguities and uncertainties can cause the inaccuracy when attempting to estimate the relative CR based on the OCP differences.

Even though these two relative CR curves obtained using different methods do not match exactly, but it clearly shows that the CR trends measured from the weight loss are accurate. Based on the above discussion, the other OCP method did generate comparable results, yet it corresponded to a more in-situ assessment despite a minor degree of uncertainties.

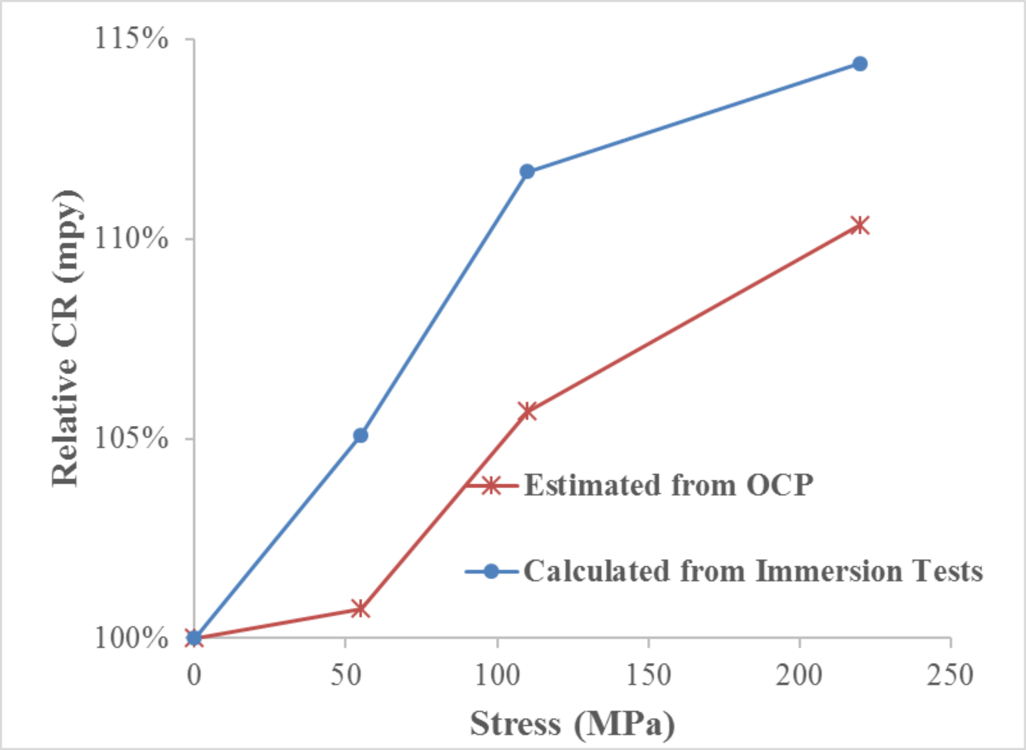

Figure 4-5. Comparison of the average relative CRs derived from the corresponding OCP differences and obtained from the immersion tests.

4.2 Effect of Residual Plastic Stresses on General Corrosion

4.2.1 Effect of Cold-rolling on General Corrosion

One shortcoming of using tensile deformation as the source of strain was that the degree of plastic deformation needed to be limited so that it did not induce potential premature failures, like cracking. To extend the degree of plasticity, carbon steel A569 samples cold-rolled (CR), up to 50% reduction in thickness in this study. Plastically deformed metals store strain energy mainly in the dislocations and other defects, as well as the elastic compressive stresses. Even though the residual stress measured at the surface does not directly measure the total strain energy stored in the carbon steel A569 specimens, it indicates the strain energy levels due to the presence of dislocations and elastic deformation. The immersion tests were used to quantitatively evaluate the effect of cold-rolling as another form of plastic deformation on general corrosion in 2 M H_2SO_4 at 50 ^{o}C 24 hours.

4.2.1.1 Microstructural Evolution upon Cold-rolling

Carbon steel A569 samples were annealed at 850 ^{o}C to remove residual stresses, and then cold-rolled to different levels of thickness reduction, namely 0%, 5%, 10%, 25% and 50%. 0% was referred as the annealed condition. The stored strain energy due to cold-rolling was mainly comprised of the compressive stress and the structural defects like dislocations. The resultant microstructural evolution was revealed in Fig. 4-6 using the Nital etching. Across this range of applied cold-rolling levels, it was observed that grains started to elongate and orient along the rolling direction as the red arrow pointed. Twinning was barely seen in all tested microstructures, probably because that A569 is a body-center-cubic (BCC) crystal structure, which made slips not as easy as in face-center-cubic (FCC) systems.

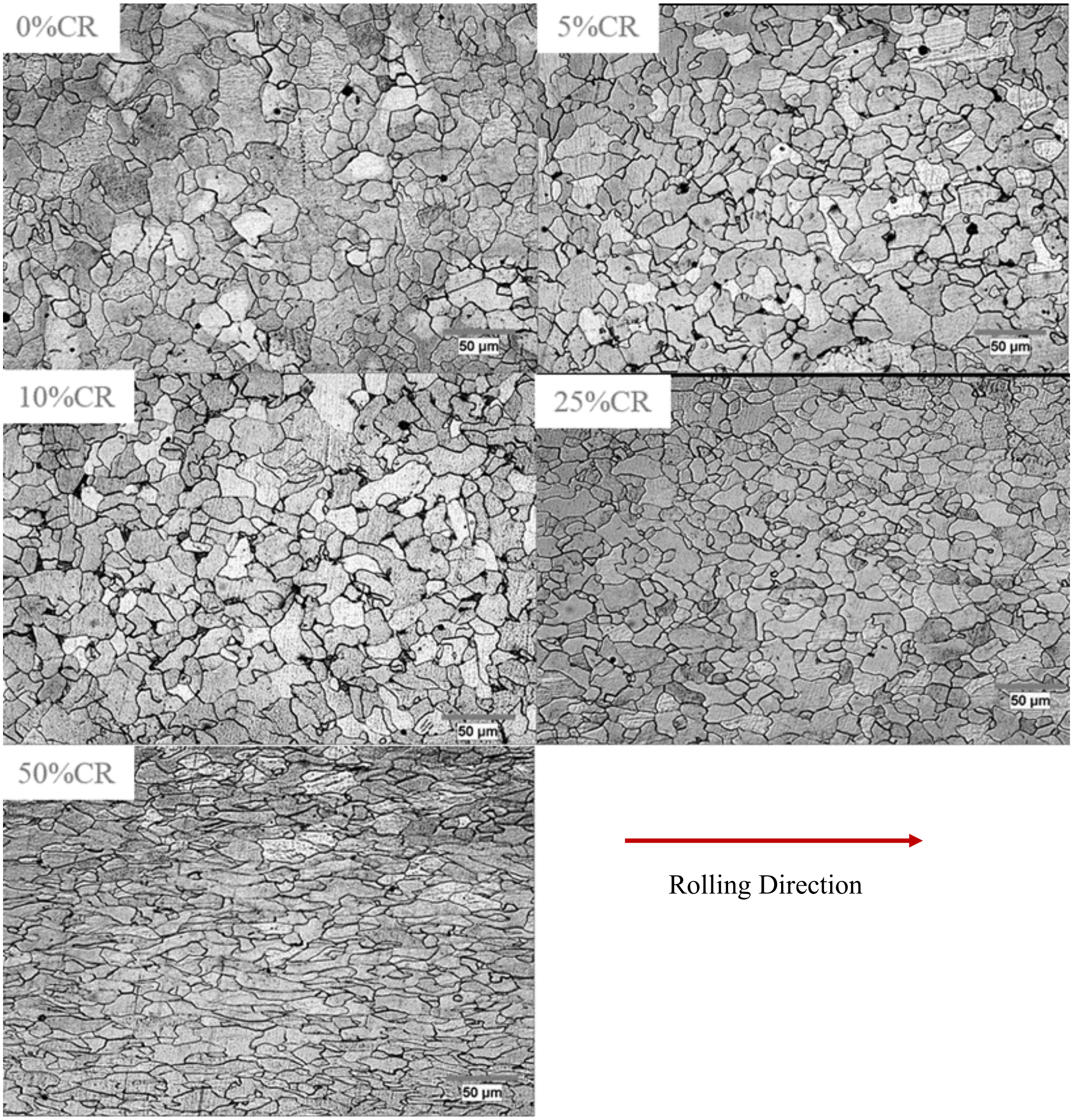

Figure 4-6. Microstructural evolution of CS A569 cold-rolled to 0% (annealed), 5%, 10%, 25% and 50%.

4.2.1.2 Residual Stress Measurements

The residual stresses on cold-rolled samples were measure using X-ray Diffraction (XRD). Even though residual stress measured at the surface does not directly measure the total strain energy stored in the carbon steel A569 samples, it can still give useful clues on the strain energy levels due to the cold-rolling. A569 samples were cold-rolled (CR) to thickness reduction of 0%, 5%, 10%, 25%, and 50%.

All samples were mechanically polished to 2000 grit finish. Residual stress measurements at the specimen surface were made by using the Panalytical Empyrean X-ray Diffraction. Each measurement scanned sixteen different spots on a 1cm x 1cm specimen surface. A monotonic trend was exhibited, as the compressive residual stress increased with an increase in percentage cold-rolling (CR), as shown in Figure 4-7. Another measurement was done on a mill-finished sample, meaning the sample was simply annealed, surface-cleaned using the Clark's solution, without mechanically polishing. The change in the stress from the mill-finished (as-annealed and surface-cleaned) specimen to 0% CR (specimen annealed and mechanically polished) indicated that the mechanical polishing inevitably introduced a significant amount of residual plastic strain into the materials even with a great care used in polishing. A distinct large increase was found from 0% CR to 5%, and the residual stress seemed to level up at a much slower pace from 5% CR to 50% CR. This meant that more strain energy could be stored in structural defects, such as dislocations and sub-grain boundaries upon the higher degrees of cold-rolling taking place.

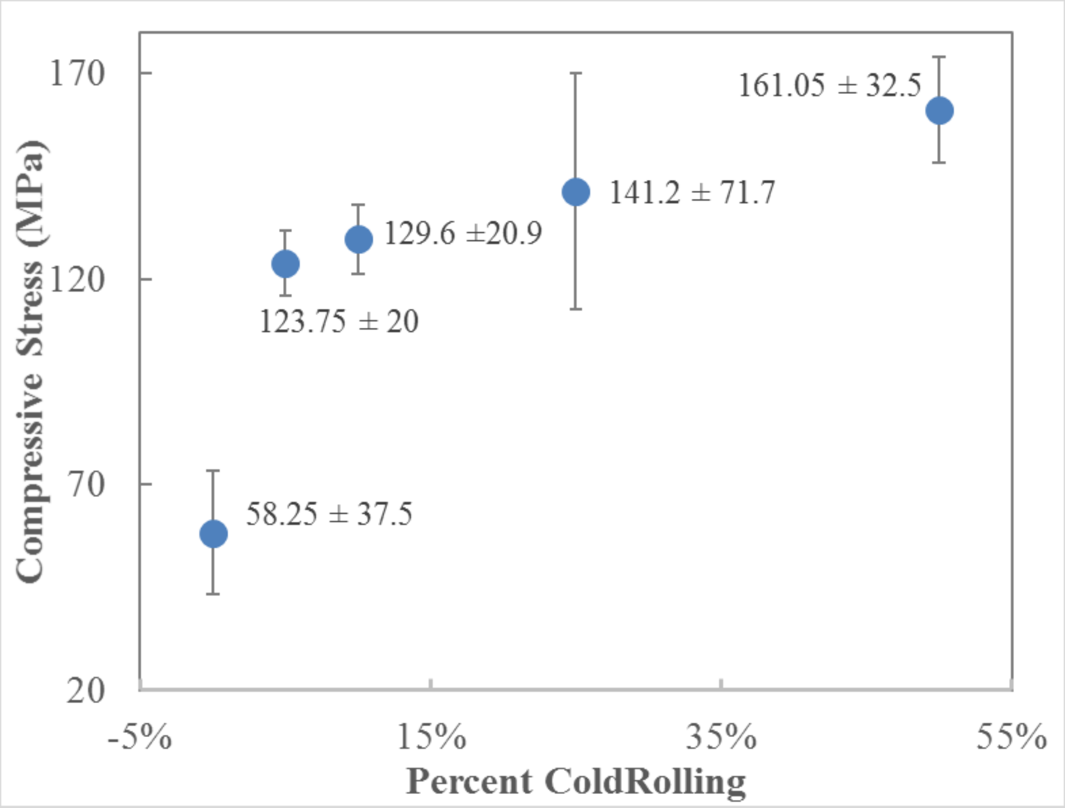

Figure 4-7. Residual stress as a function of percentage cold-rolling.

4.2.1.3 The Effect of Cold-rolling on General Corrosion

The immersion tests were performed at room temperature on Carbon Steel A569 samples with different % CR. The polished carbon steel samples were placed in a 2 M sulfuric acid solution at 50 ^{o}C for 24 hours. The weight loss was calculated at the end of the 24 hours with respect to the measured residual stresses as shown in Fig. 4-8. Each test was repeated twice, and the reproducibility was reasonable as the error bars indicated in Fig. 4-8. The average corrosion rate increased from 4955.3 mpy to 6435.2 mpy with the increasing percentage cold-rolling level. Higher corrosion rates of deformed specimens are indicative of higher active dissolution rates, which means that the presence of strain energy enhanced the active dissolution rate. Therefore, the generic governing mechanism still held true that strain energy provides additional driving force for general corrosion. It was also noticed that the slope connecting 0%CR to 10%CR was steeper than the slope connecting 10%CR to 50%CR data. This change of linearity meant that the dominant deformation mechanism beyond 10%CR could be different from the deformation mechanism in the early stage. It is well known that beyond a certain level of deformation, dislocations start to pile up and low-angle grain boundaries start to form to accommodate the increased lattice distortion. This may explain why we observed that the increasing trend of the measured residual stress slowed down beyond 5%-10% CR. Therefore, it was plausible to believe that the strain energy was stored in these new forms of structural defects, like dislocation pile-ups and low-angle grain boundaries. This additionally stored internal strain energy continued to enhance the tendency of general corrosion of A569.

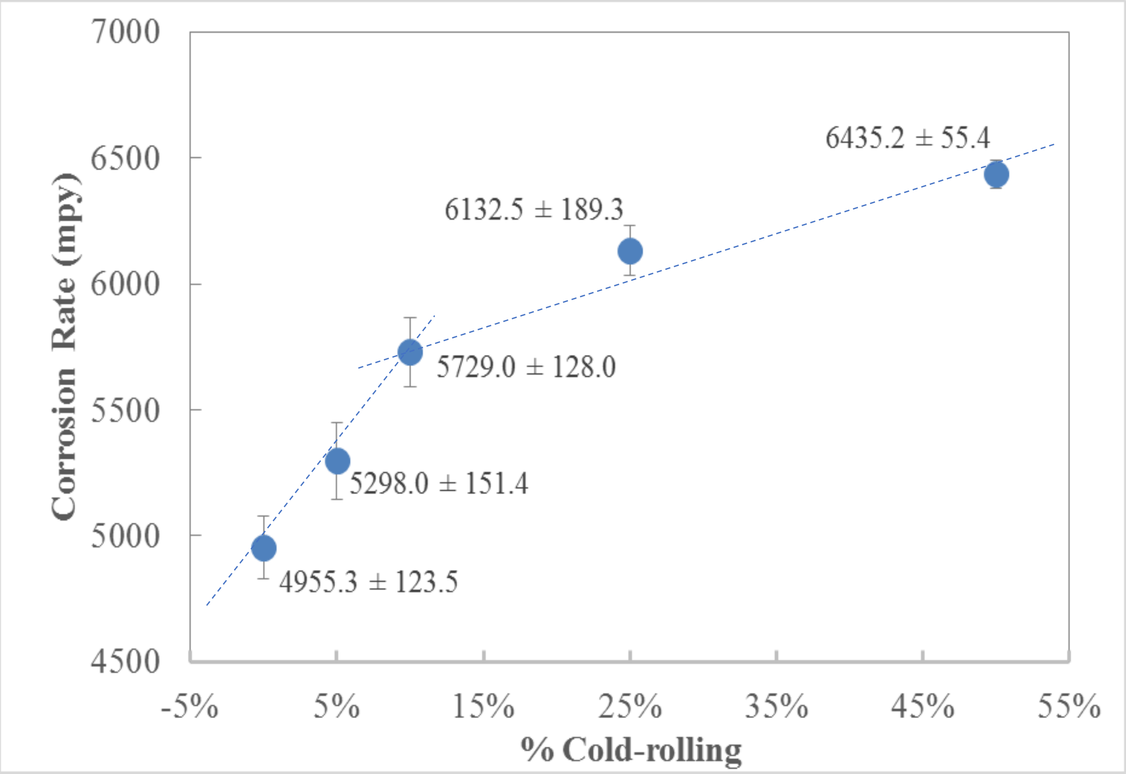

Figure 4-8. Average corrosion rates of CS A569 after the 24-hour immersion tests in a 2 M H_2SO_4 solution at 50 °C with respect to percentage cold-rolling.

Fig. 4-9 demonstrates the corrosion surfaces of A569 at the as-annealed condition and at the 50% cold-rolled condition right before being taken out of immersion. Upon visual inspection, it was clear that much more corrosion products were built up on the heavily deformed specimen.

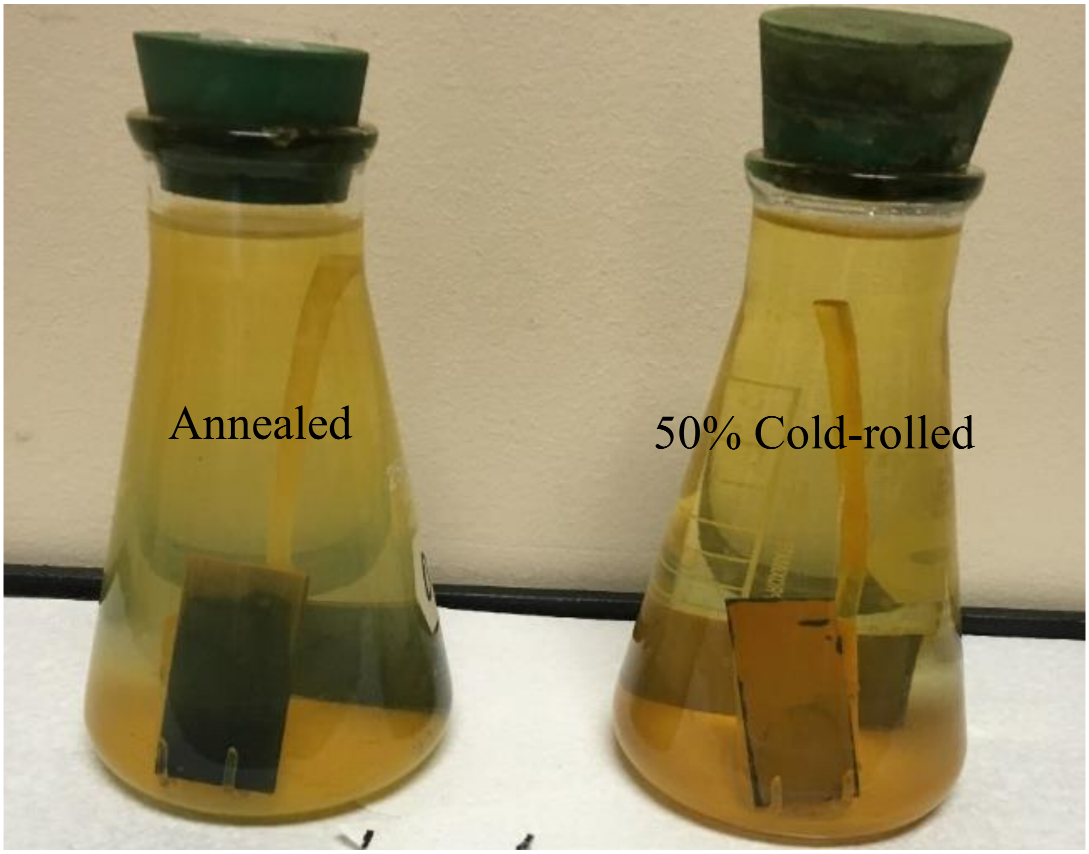

Figure 4-9. Corrosion surfaces of A569 at the as-annealed condition and at the 50% cold-rolled condition in the end of 24-hour immersion in a 2 M H_2SO_4.

It is also worth noticing that the corrosion rates for the 10%CR, 25%CR and 50%CR specimen were respectively 15.6%, 23.8%, and 29.9% higher than the corrosion rate of the annealed specimen. The corrosion rate for the specimen with 9% residual plastic strain was roughly 14.4% above the corrosion rate of the annealed specimen. This set of comparison indicated that cold-rolling and plastic tensile deformation tended to accelerate general corrosion to relatively comparable degrees for the same degree of dimension change. This may further elucidate that cold-rolling imparted more strain than plastic tensile deformation.

4.2.2 Confirmation of Strain-Accelerated General Corrosion Using Residual Plastic Strain

To confirm the strain-accelerated general corrosion, A569 specimens were subjected to different levels of tensile strain, namely 2%, 5%, and 9% and the applied strain levels were held for ten minutes before unloading. A set of 24-hour immersion tests in a 2 M H_2SO_4 solution at 50 ^oC was performed at different levels of the resultant residual plastic strain. The weight before and after the immersion test was measured for specimens loaded at each stress level, and the corresponding weight change was used to determine the corrosion rate (CR), reported here in mils per year (mpy) by accounting for the density and exposed area for each sample. The corrosion rates (CRs) of CS A569 was plotted as a function of plastic residual strain as shown in Fig. 4-10. This plastic strain effect data was compared with the corrosion rate data from a sample with 0% (no strain).

It was observed that the corrosion rate was directly proportional to the residual plastic strain, ranging from 5164 mpy to 5664 mpy. The proportionality was almost linear, which was similar to what we observed in the correlation between CRs and applied elastic stresses. The maximum corrosion rate occurred at the maximum plastic residual strain, 9%, and the lowest corrosion rate was for the baseline sample with no strain applied.

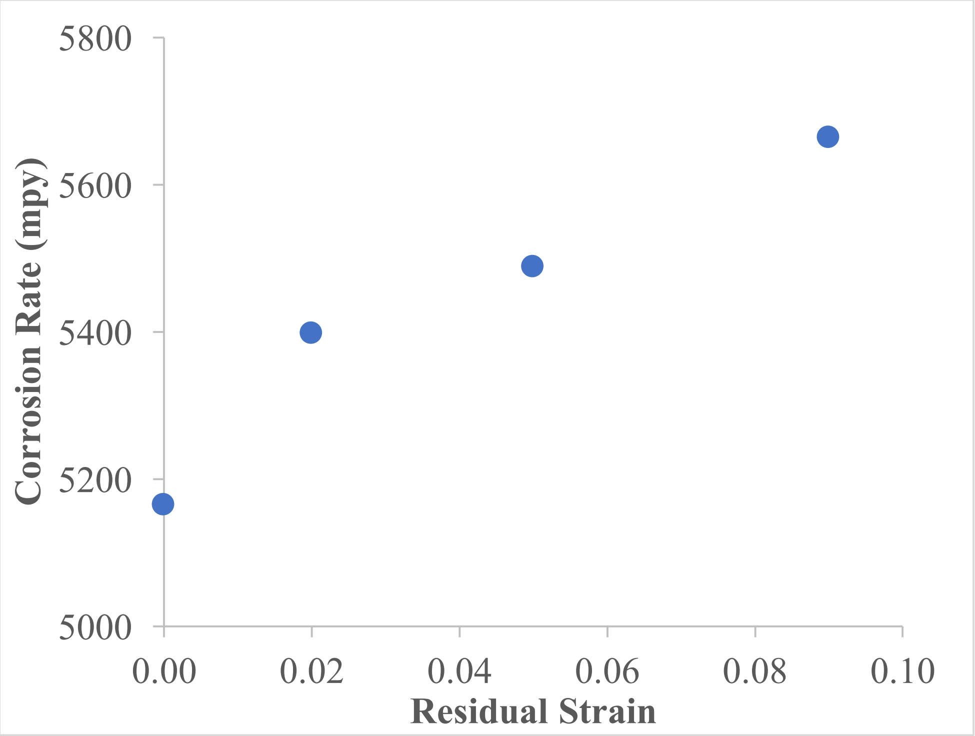

Figure 4-10. Corrosion rates (CRs) calculated from the immersion tests as a function of the plastic residual strain in a 2 M H_2SO_4 solution at 50 ^{o}C.

The corresponding OCP evolution was also monitored for each sample as illustrated in Fig. 4-11. A zoom-in view of the OCP evolution in the last hour of the test was embedded in the right bottom of Fig. 4-11. The exact OCP values ranging from -382.5 $mV_{(SCE)}$ to -387.9 $mV_{(SCE)}$ were marked next to the corresponding OCP curve in the Figure. It was clear that the OCP in the end of the test was stabilized at a lower value as the applied stress increased, confirming higher residual plastic strain drove stronger corrosion reactions.

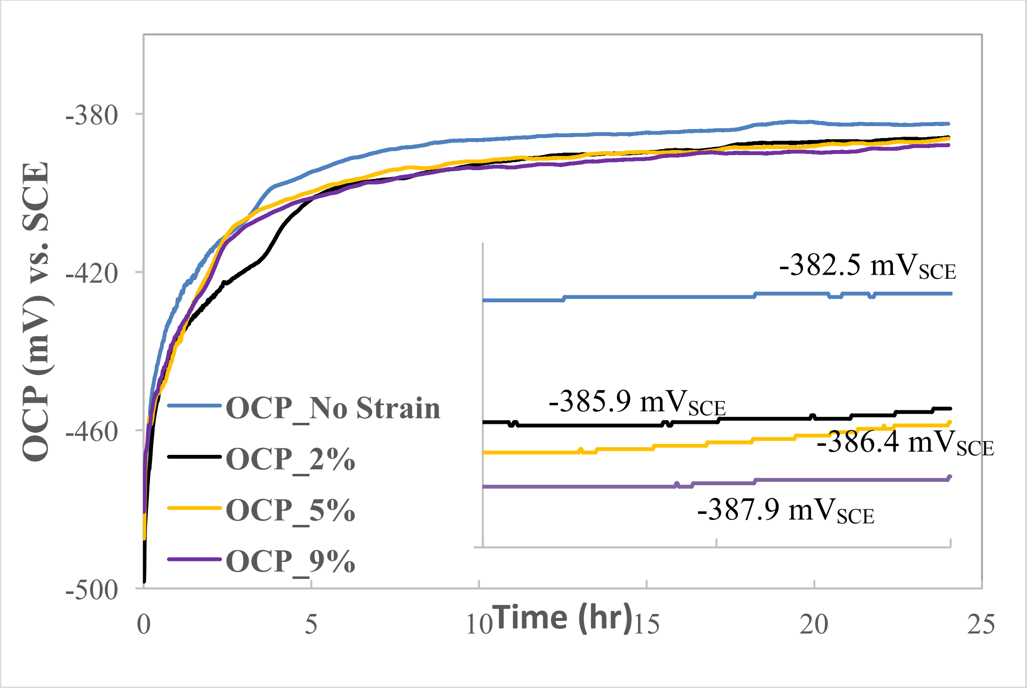

Figure 4-11. OCP evolution of CS A569 at 4 plastic residual strain levels (no strain, 2%, 5% and 9%) during 24-hour immersion in a 2 M H_2SO_4 solution at 50 ^oC.

The linear polarization resistance (LPR) tests were used to assess the CR of CS A569 at the end of the immersion tests. The LPR curves for the four strain levels were represented in Fig. 4-8. The relative polarization ranges of these LPR curves also reflected the decreasing OCP trend as the residual strain increased. The flatter the slopes exhibit, the higher the CRs are. The samples possessing higher degrees of residual strain general exhibited flatter slopes, hence indicating stronger corrosion activities.

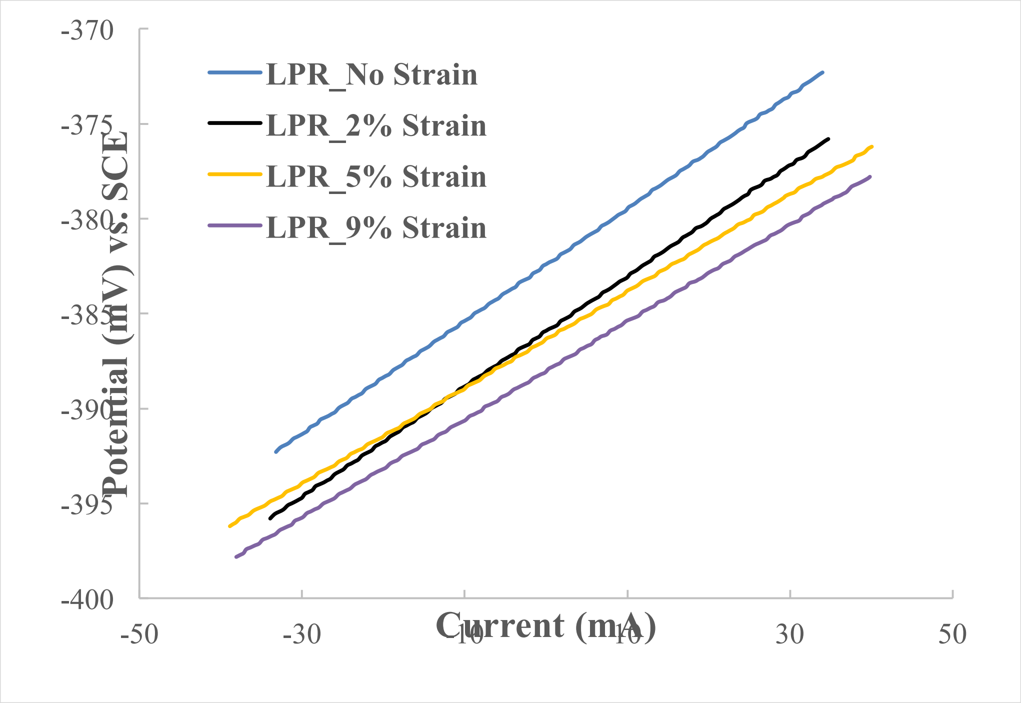

Figure 4-12. Current responses to the anodic polarization during the LPR tests at 4 residual strain levels (0%, 2%, 5% and 9%).

The CRs were then calculated based on Eq. 3.1 and Eq. 3.2, and the results were plotted in Fig. 4-9. It was demonstrated that the CR assessed by LPR followed a positive correlation with the residual strain. So far, the CRs were assessed using three different methods for plastically deformed tensile samples: the immersion test (weight loss method), the OCP indication and the LPR test. All three techniques confirmed that strain energy acting as an additional driving force accelerated general corrosion.

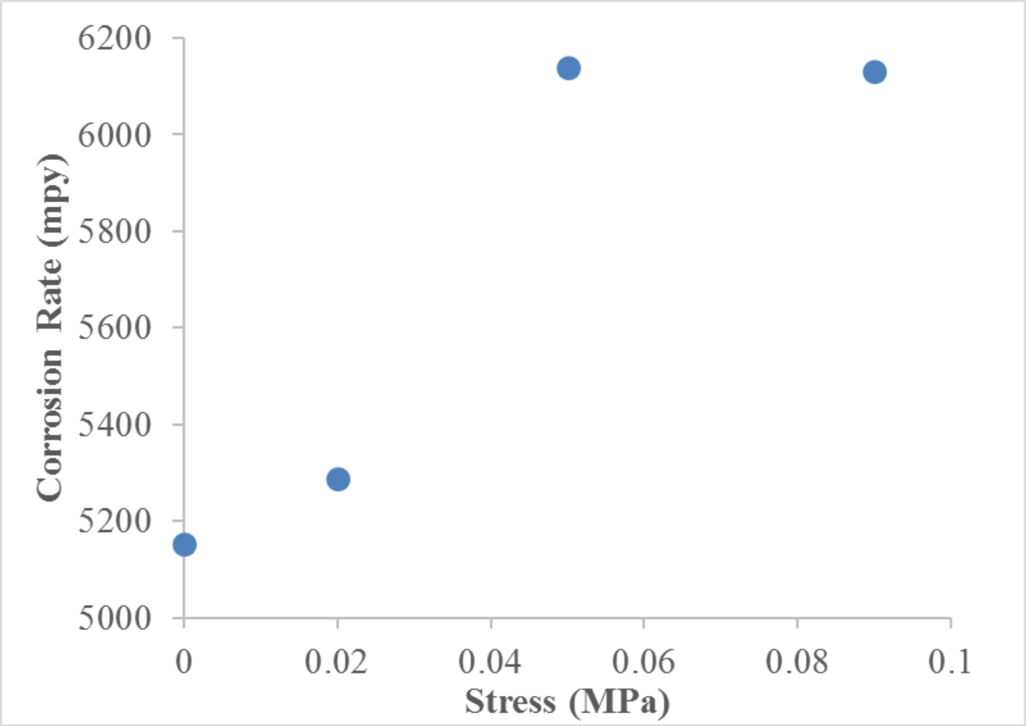

Figure 4-13. Corrosion rates (CRs) calculated from the LPR tests as a function of the plastic residual strain in a 2 M H_2SO_4 solution at 50 ^{o}C.

4.3 Conclusions

In this chapter, we discussed the effect of stresses/strain on general corrosion of CS A569. For tensile samples, the weight change measurements from corrosion tests, the corrosion rate estimation from OCP, and the corrosion rate calculated from LPR test were used to quantitatively assess the absolute or relative corrosion rates of CS A569 specimens in a strong sulfuric acid. For cold-rolled samples, the immersion test was employed to quantify the influence of plastic deformation by cold-rolling on general corrosion. The governing thermodynamic principle that strain energy can accelerate general corrosion held true from all the results obtained in this study. The following conclusions can be drawn from the results in this chapter:

1. An additional strain energy in the carbon steel sample accelerated the general corrosion by providing an increased driving force, regardless of deformation modes (either elastic or plastic) and deformation techniques (either tensile deformation or cold-rolling).
2. Conclusion 1 was verified using different general corrosion measurement methods, including immersion tests, estimation based on OCP and LPR tests. The immersion test reflected an average corrosion rate, while assessing the corrosion rate by the OCP estimation or the LPR tests at the end of the immersion tests may only convey information at the stabilized state. This can create discrepancies in the final value of corrosion rates measured. One can obtain a set of very comprehensive information by incorporating and setting up all three tests in one experiment properly.
3. The corrosion rate increased more rapidly in the range from 0%CR to 10% than it did in the range from 10%CR to 50%. This was likely because that the deformation mechanism changed to store more strain as dislocation pile-ups and new-formed low-angle grain boundaries.

CHAPTER 5. EFFECT OF ELASTIC STRESSES ON PITTING CORROSION

The effect of different forms of strain on the general corrosion behavior of an alloy was quantitatively and qualitatively presented in the previous chapter. However, general corrosion is greatly suppressed in many material/environment systems under passivation control. Stainless steel 304 was used in this study to investigate the influence of strain on pitting corrosion in an active-passive alloy system.

It is very important to keep in mind that corrosion is a surface phenomenon. Stainless steels alloyed with at least 12% Cr form a Cr_2O_3-rich oxide film on the surfaces, and this oxide film acts as a barrier film and helps to passivate the alloy surfaces. Hence, stainless steels are protected from general corrosion in most environments. However, localized corrosion, such as pitting corrosion often cause catastrophic failures in stainless steels. It was also widely reported that many failures of pitting corrosion were suspiciously correlated to either internal/residual strain or external/applied strain [140, 143, 148]. Yet, correlation does not necessarily equal causation. Most prior studies have confirmed the negative effect of strain on pitting corrosion of stainless steels, and pertinent evidence was also demonstrated [1, 100, 104, 139, 141, 142]. However, the exact mechanism still remained elusive, and a unified understanding through a systematic investigation under different forms of stresses/strain is lacking.

In this study, we started the investigation using elastic stresses as the variable and aimed to explain the mechanism of the stress-assisted pitting behavior. Many concepts in pitting corrosion, such as pit growth and salt film were used to elucidate the interaction between elastic stresses and pitting corrosion of stainless steel 304.

5.1 Effect of Environments on Mechanical Behavior of SS 304

Tensile tests were performed on SS 304, both in air and in 0.1 M NaCl at 50 ^oC. The corresponding stress vs. strain curves are shown in Fig. 5-1. It is clear from the results in Fig. 5-1 that there was a significant loss in ductility due to the presence of Cl^-. The open circuit potential (OCP) response was also recorded throughout the tensile test in 0.1 M NaCl at 50 ^oC as shown in Fig. 5-2. It was observed that the OCP curve experienced many current transients upon the yield point which took place around 200 MPa. This indicated that passive film was ruptured as deformation exceeded yielding, and this phenomenon occurred throughout the plastic regime of tensile test. From the perspective of film rupture, the in-situ plastic deformation ruptures the intact passive film, and therefore the material enters a state of unstable passivity. Even though a rapid repassivation can be expected on stainless steel systems, the constant breakdown of passive film beyond yielding may promote pitting corrosion at the stressed surface. Since yield stress was around 200 MPa for both tests, any stress below 200 MPa is in the elastic regime. Four elastics stress levels, namely 0 MPa, 52 MPa, 103 MPa and 155 MPa were applied to each fresh tensile sample to assess the pitting behavior of elastically deformed SS 304.

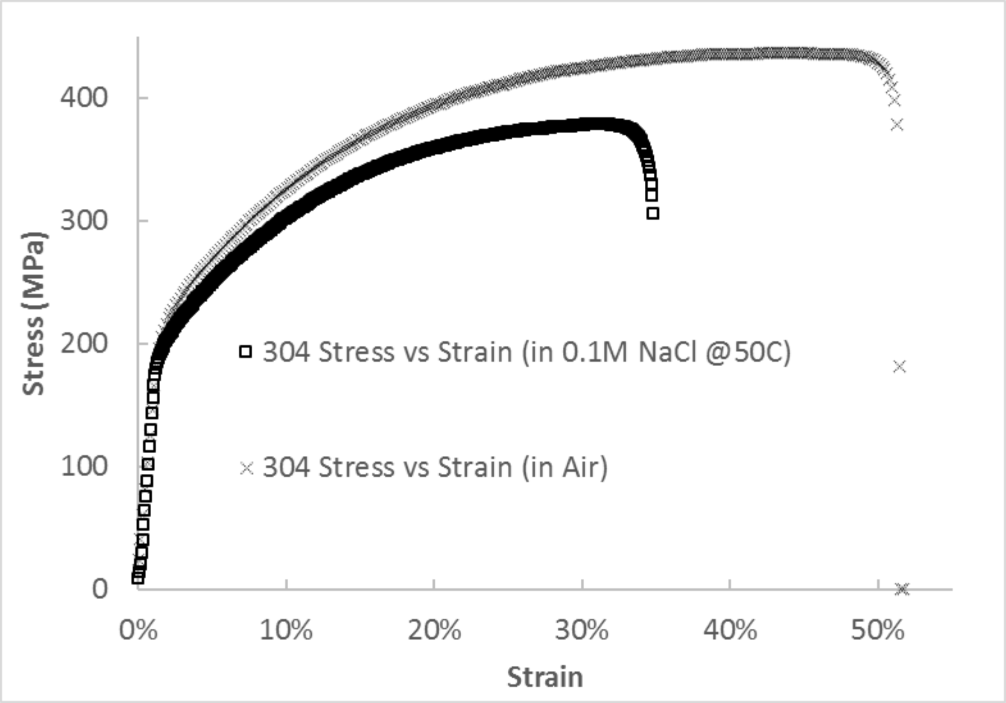

Figure 5-1. Stress vs. strain curves of SS 304 both in dry air and in 0.1 M NaCl at 50 °C.

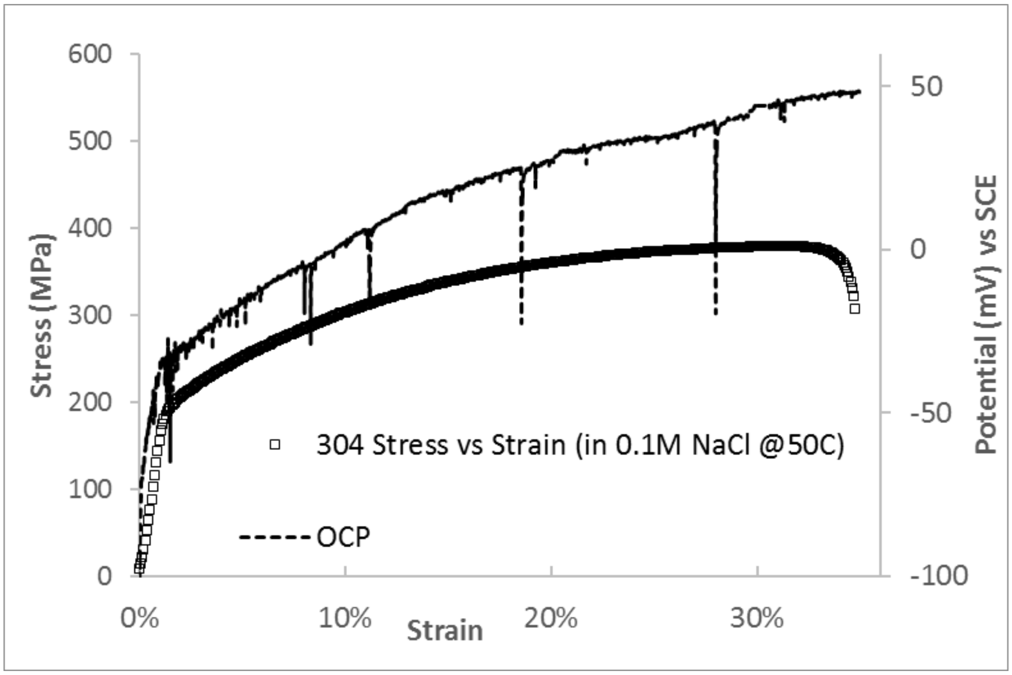

Figure 5-2. OCP response during the tensile test of SS 304 in 0.1 M NaCl at 50 °C.

5.2 Effect of Elastic Stresses on Pitting Potential

A set of cyclic polarization tests was performed on SS 304 specimens at various stress levels in 0.1 M NaCl solution at 50 ^{o}C and each test was repeated at least five times. Four elastic tensile stresses, namely 0 MPa, 52 MPa, 103 MPa, and 155 MPa were applied to SS 304. A monotonically decreasing trend of pitting potential is shown in Fig. 5-3 as the applied tensile stress increases. The average pitting potential at each applied stress level was calculated based on five repetitions of tests in Fig. 5-4. This consistent decreasing trend of the pitting potential suggested that elastic tensile stresses make of SS 304 more susceptible to pitting corrosion in 0.1M NaCl at 50 ^{o}C.

To study the effect of stable passive film, a set of SS 304 specimens were prepared by pre-oxidizing them in a 2 M HNO_3 solution for 1 hour to develop a more protective passive film on the surface. Chemical composition of the resultant surface passive film was characterized using XPS. XPS results are summarized in Table 5-1. From Table 5-1, it was clear that more Cr was present on the pre-oxidized SS 304 surface. It was noticed that there was a significant increase in the Cr/O ratio after the peroxidation, while the Fe/O ratio remained nearly unchanged. This was an indication that a more Cr-oxide rich passive film was formed after the pre-oxidation treatment. A new set of cyclic polarization tests were performed on the pre-oxidized SS 304 tensile samples by applying the same four levels of elastic tensile stresses. The resultant average pitting potentials were calculated in Fig. 5-5 over 3 repetitions of tests at each stress level. The pre-oxidized specimens had a general increase in the pitting potential as compared to an equivalent test with non-treated samples, probably due to the Cr-oxide rich film formed at the surface due to pre-oxidation as illustrated in Table 5-1. However, the negative effect of applied elastic tensile stresses on pitting behavior of SS 304 was again observed for the pre-oxidized tensile samples. Based on these results, it can be argued that the negative effect of elastic deformation on localized pitting corrosion was independent of the composition of the passive film on SS 304. This may further indicate that the change in surface film inhomogeneities (if there are any) due to elastic deformation is not a key factor in making a significant impact on the increased pitting corrosion susceptibility of SS 304 samples tested under applied elastic stresses.

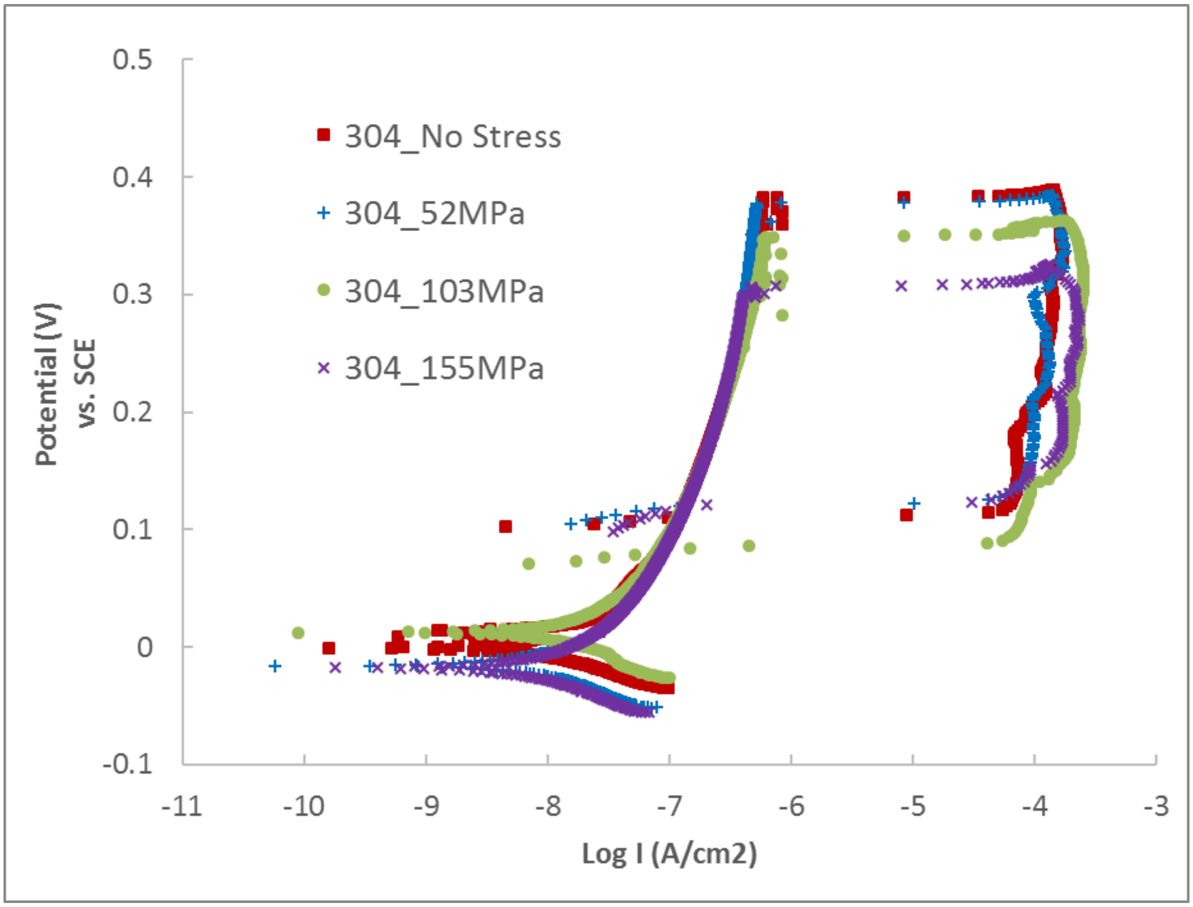

Figure 5-3. Cyclic polarization behavior of SS 304 at no stress (0 MPa), 52 MPa, 103 MPa, and 155 MPa in 0.1 M NaCl solution at 50 ^{o}C.

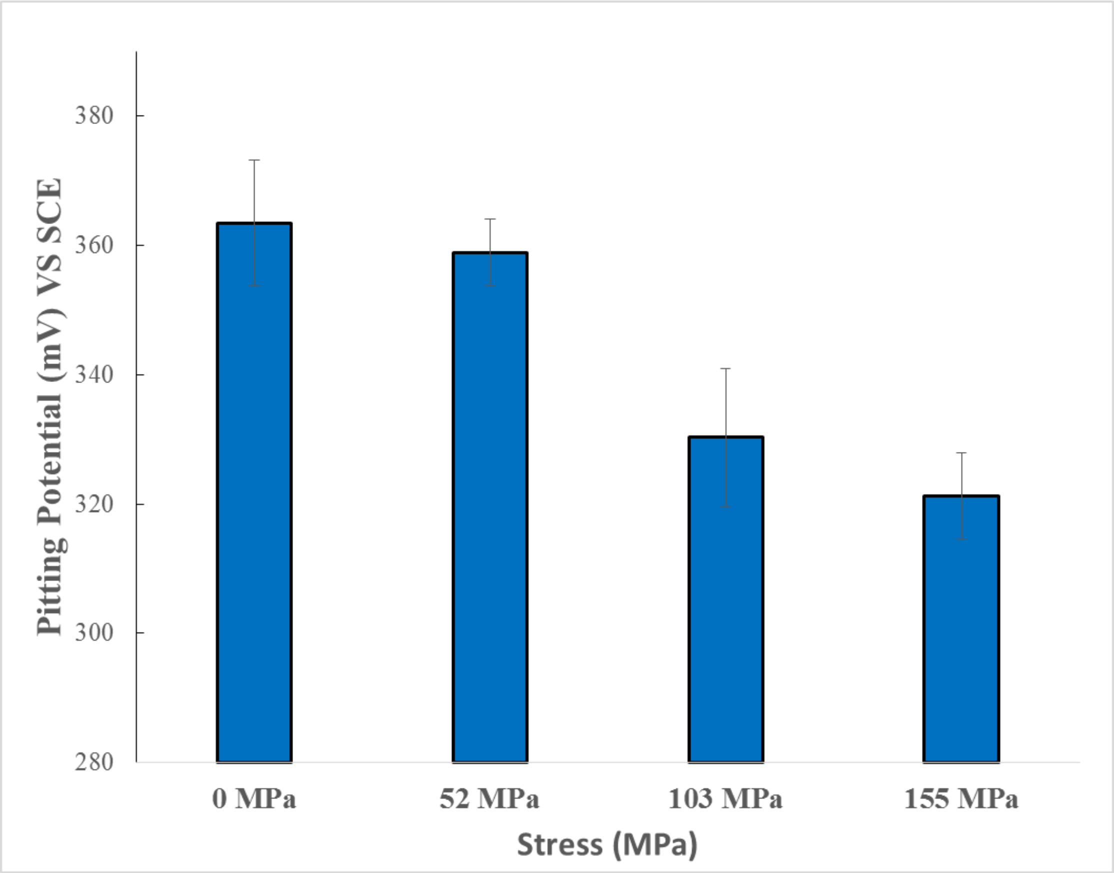

Figure 5-4. Average pitting potentials of SS 304 at no stress (0 MPa), 52 MPa, 103 MPa, and 155 MPa in 0.1 M NaCl solution at 50 ^{o}C.

Table 5-1. Surface Chemical Composition (wt%) of SS 304 and Pre-oxidized SS 304.

	O	**Cr**	**Fe**	**Ni**	**Mn**	**Zn**	**Ca**	**Cr/O**	**Fe/O**
304	73.33	10.46	11.62		0.83	2	1.76	0.14	0.16
304_Pre-oxidized	69.17	16.28	10.67	2.09	1.2			0.24	0.15

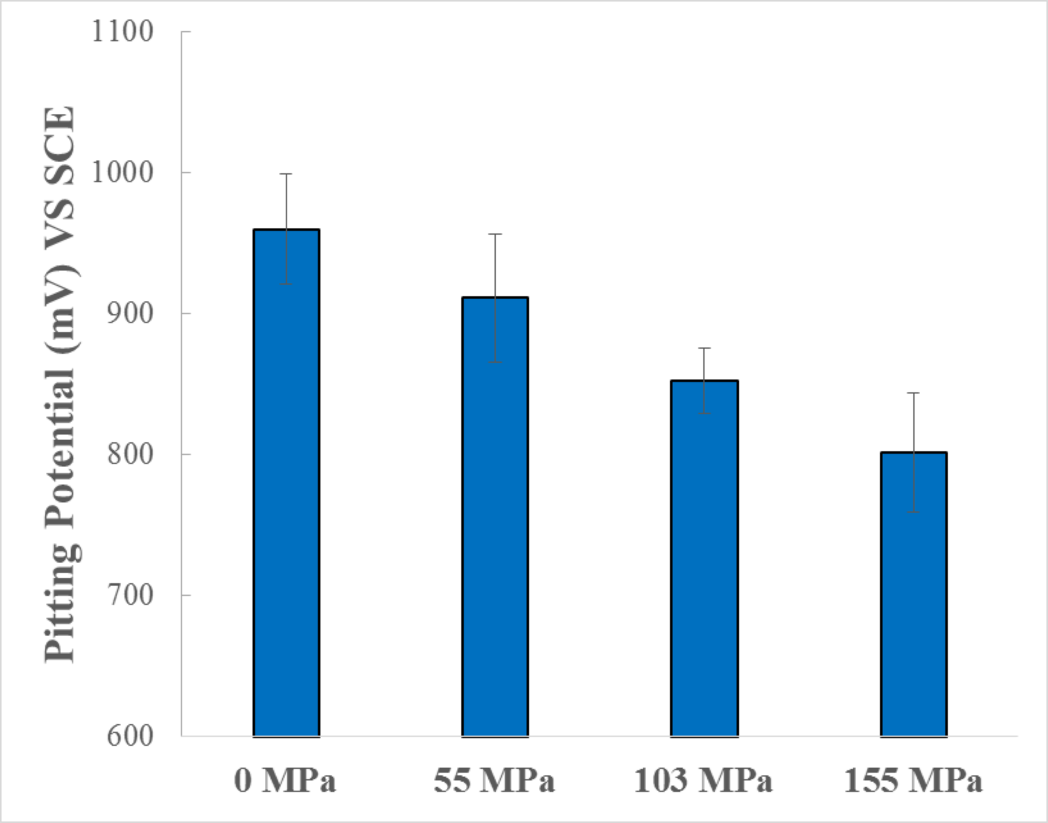

Figure 5-5. Average pitting potentials of pre-oxidized SS 304 at no stress (0 MPa), 52 MPa, 103 MPa, and 155 MPa in 0.1 M NaCl solution at 50 ^{o}C.

5.3 Effect of Elastic Stresses on Metastable to Stable Pit-Growth Transition

To further investigate the stress-assisted pitting corrosion behavior, chronoamperometry tests were performed on SS 304 specimens at +250 mV$_{(SCE)}$ in 0.1M NaCl at 50 ^{o}C. Tensile samples were loaded at 0 MPa (no stress), 52 MPa, 103 MPa and 155 MPa, and all metastable pit and stable pit activities were detected and recorded, as shown by the results in Fig. 5-6 a-d. In Fig. 5-6 a-d, each graph contains five runs of chronoamperometry tests at a given elastic stress level. Results in Fig. 7a show that mostly metastable pits were developed when no elastic stress (0 MPa) was applied under these test conditions. In this set of tests, a stable pit was defined as a single event with a current transient greater than 100 μA.

As the applied stress increases, the frequency of stable pitting increased from 1 in 5 at 53 MPa to 4 in 5 at 155 MPa. By directly comparing the metastable pitting currents between no applied stress and 155 MPa, it was noticed that the metastable pits in the no stress case grew larger than the ones at 155 MPa as indicated by the magnitude of the current transients, as shown by the inlay zoomed-in views. It was likely that the large metastable pits were not stable at higher stresses, e.g. at 155 MPa, as they rather became stable pits. It was found that the applied stress could potentially hinder the repassivation process so that large metastable pits could eventually transit to stable pits, depending of the applied elastic stress values. As demonstrated in Fig. 5-2, tensile stresses beyond yielding can easily rupture the passive film formed on the surfaces. Pit initiation creates a 3-D pit-geometry on the surface, and this geometry can lead to stress concentration around the pit wall, therefore concentrating the stress field around the pit that is comprised of tensile, compressive and shear stresses in the pit vicinity. Depending on the applied stresses and pit geometry, localized stress state at the pit surface can potentially disrupt or destabilize the passive film and to stabilize the pit growth. To put it simple: data indicates that the applied elastic stresses hinder the pit-repassivation by assisting the pit growth.

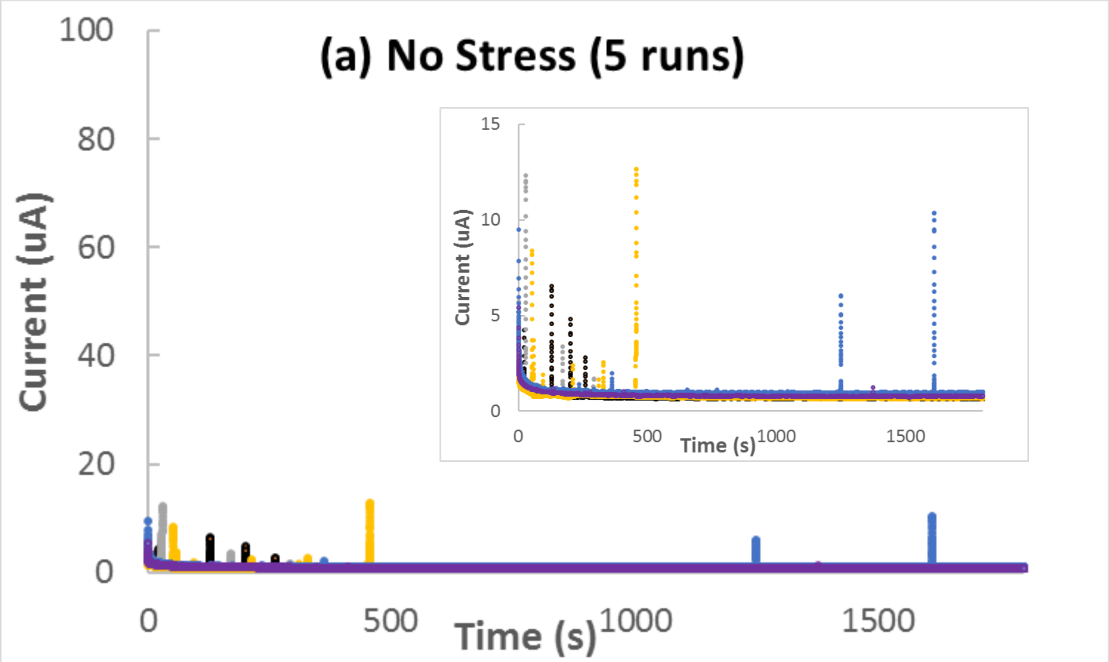
(a) No Stress (5 runs)
Current (uA)
100
80
60
40
20
0
0
500
Time (s)
1000
1500
15
10
5
0
Current (uA)
0
500
Time (s)
1000
1500

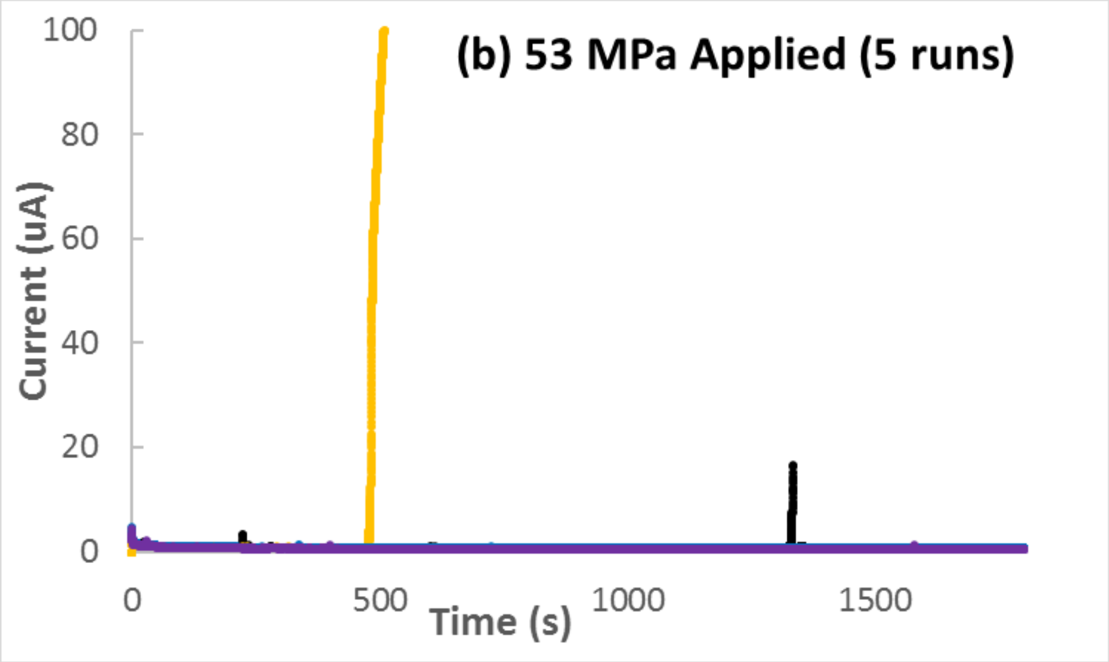
(b) 53 MPa Applied (5 runs)
Current (uA)
100
80
60
40
20
0
0
500
Time (s)
1000
1500

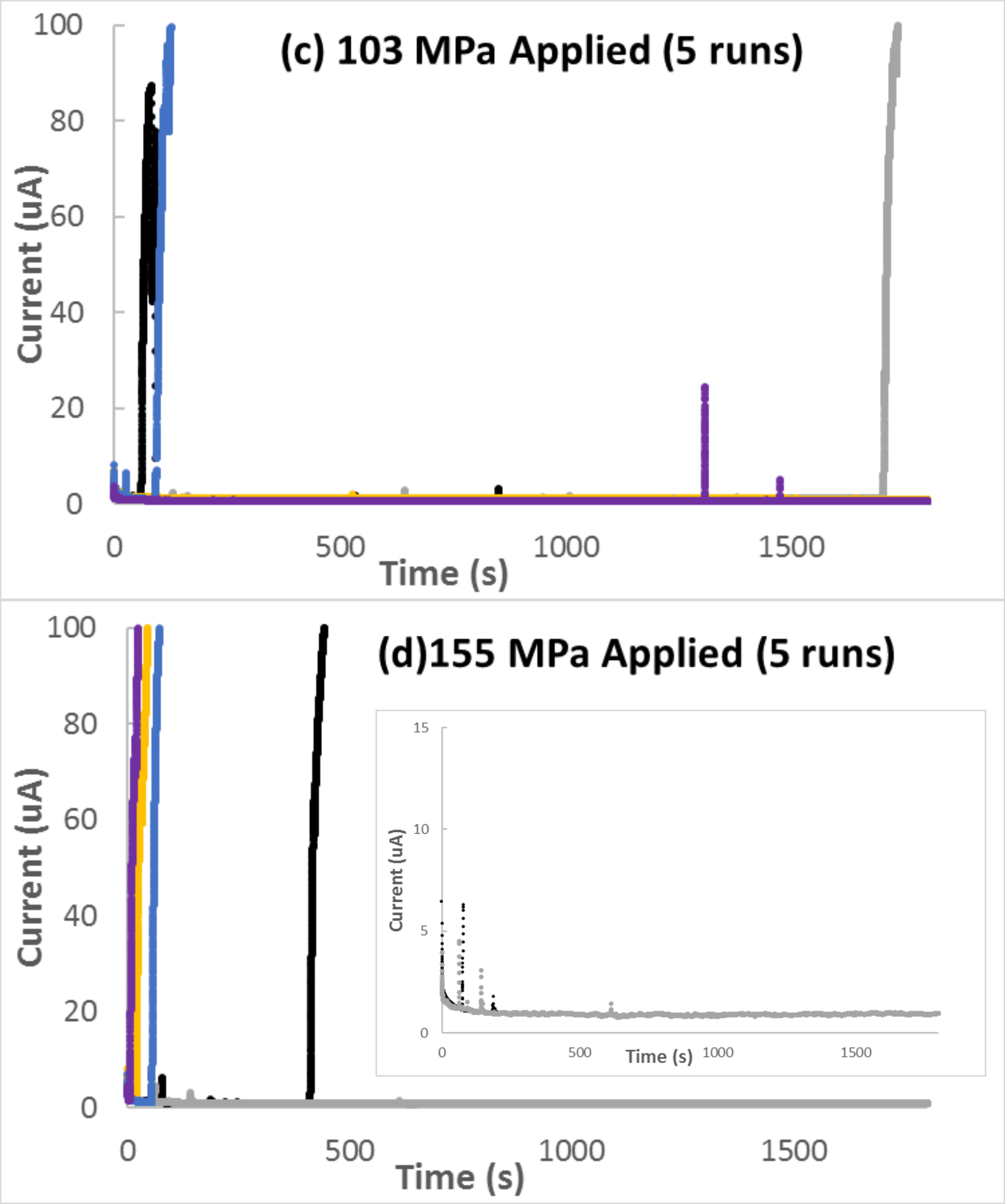

Figure 5-6. Current responses of SS 304 at +250 mV$_{(SCE)}$ and 50 ^{o}C in 0.1M NaCl with applied stress of (a) no stress (0 MPa), (b) 52 MPa, (c) 103 MPa and (d) 155 MPa respectively.

5.4 Effect of Elastic Stresses on Pit Growth

To verify if the elastic stresses may facilitate pit growth, controlled tests were done where a single-pit was intentionally initiated on the exposed surface of a SS 304 tensile sample by applying a potential of +300 $mV_{(SCE)}$ till the transient current reached +40 μA. After the initiation of pits, samples were examined under optical microscope to confirm that only single pit had initiated in the test area. Samples with initiated pit were further tested under applied elastic stresses, where the tests were done at four applied stress levels, i.e. 0 MPa (no stress), 52 MPa, 103 MPa and 155 MPa, and the samples with an initiated single pit were used in the following investigation. It was noticed that the incubation time to initiate such a pit varied from one test run to another regardless of the stress levels applied. This was because the passive film of SS 304 formed at +300 $mV_{(SCE)}$ in 0.1M NaCl at 50 ^{o}C is unstable, and it led to the highly stochastic pit-initiation events. To avoid interference between multiple pits during the pit growth stage, only the data generated from the surfaces with a single-pit in the exposed surfaces were selected. The resultant 3-D pit geometry developed was examined using a laser profilometer as shown in Fig. 5-7. Cylindrical pits were observed across all tested samples, and the diameter to depth ratio for cylindrical pits was around 1.5 across for all applied stress levels tested. This observation agrees with some previous observations, suggesting that the stable pits with flat walls were typically developed at low potentials, whereas higher applied potentials (significantly higher than the pitting potential) resulted into hemispherical pits [116, 117, 127]. The volume of most examined pits was also calculated from the current transient data and were found to be close to 1,000 μm^3, which indicated that the amounts of metal corroded inside the pits at different stress levels were relatively similar. Therefore, the low pH inside the pits caused by metal cation hydrolysis should also be similar with such a pit-initiation method. It ensured that the further pit growth step was proceeded in similar 3-

D geometries and chemical environments. It was also noticed that pit covers were barely seen on these initiated pits, probably because the pit covers had ruptured if there had existed any.

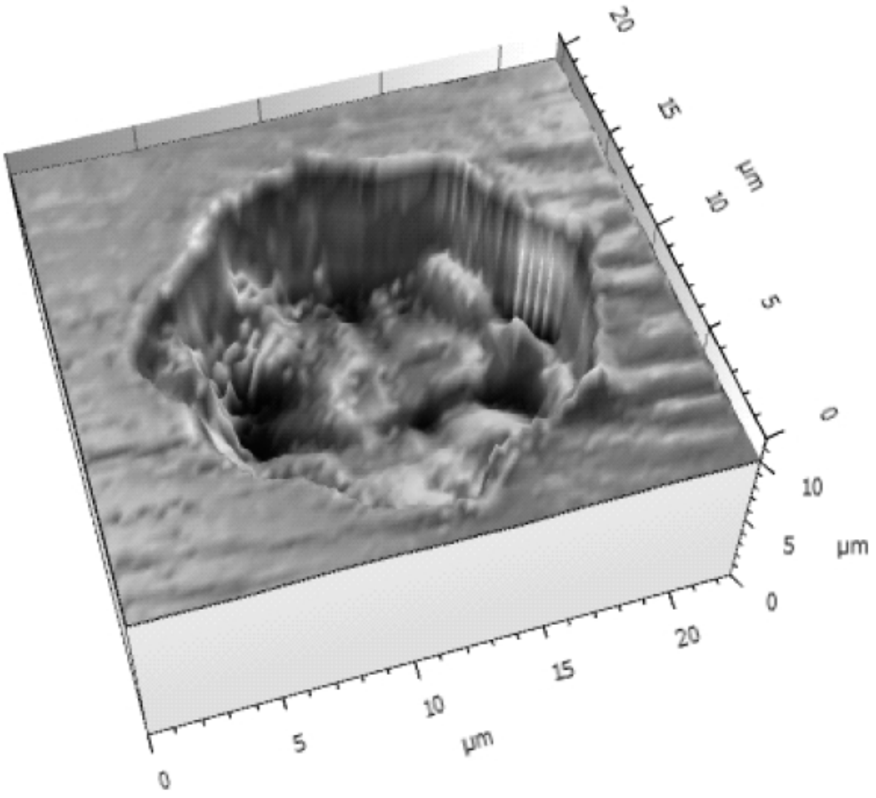

Figure 5-7. A representative 3-D 40uA-pit geometry developed at +300 mV$_{(SCE)}$.

As the pit-initiation current reached +40 µA, the 3-D pit geometry inside the pits developed at the four applied elastic stress levels were similar. Once the pit had initiated, the applied potential was immediately switched to +250 mV$_{(SCE)}$ in order to repassivate the pit, and current responses were monitored and are shown in Fig. 5-8. Triplicate tests were done under each applied stress level. It is clearly observed from the results in Fig. 5-8 that the pit repassavated upon changing the applied potential from +300 mV$_{(SCE)}$ to +250 mV$_{(SCE)}$ when no stress was applied, while the repassivation took longer time to when the applied stress level was increased. The repassivation failed for the sample with 155 MPa applied stress, indicated by the increasing current terminated at +60 μA. To demonstrate the reproducibility of this set of tests, as shown by the triplicate set of data in Fig. 5-9. From Fig. 5-9 a-d, the trend of increasing repassivation loop size was consistent as the applied stress was increased. One out of three pit-repassivation tests seemed to fail at 52 MPa. However, the pit repassivated within the first 2 seconds and then started to grow stably. This could be due to the interference of crevice corrosion at that specific moment or an initiation of a secondary pit. There was also one repassivation test failed at 103 MPa, with a much more rapid pit-growth indicated by the fast rate of current increase. This set of comparison tests suggested that a stable pit growth was favored when a higher level of elastic stress was applied. It was discussed earlier in the thesis that the applied elastic stresses tended to induce stable pits on SS 304 whereas an un-stressed SS 304 sample developed large metastable pitting. It was also observed that the negative effect of elastic stresses is independent of the surface chemistry of the passive film. Since elastic stresses seem to alter the pit-growth behavior of stainless steel by stabilizing an active dissolution inside the pits, the previous two observations can now also be rationalized: when the pit growth is stabilized, repassivation of pits may not be preferred, hence the metastable pits will become stable pits; regardless of the surface chemistry of the passive film, presence of elastics stresses imparts a negative effect on pitting corrosion as long as the passive film of the material still breaks down and undergoes pit initiation.

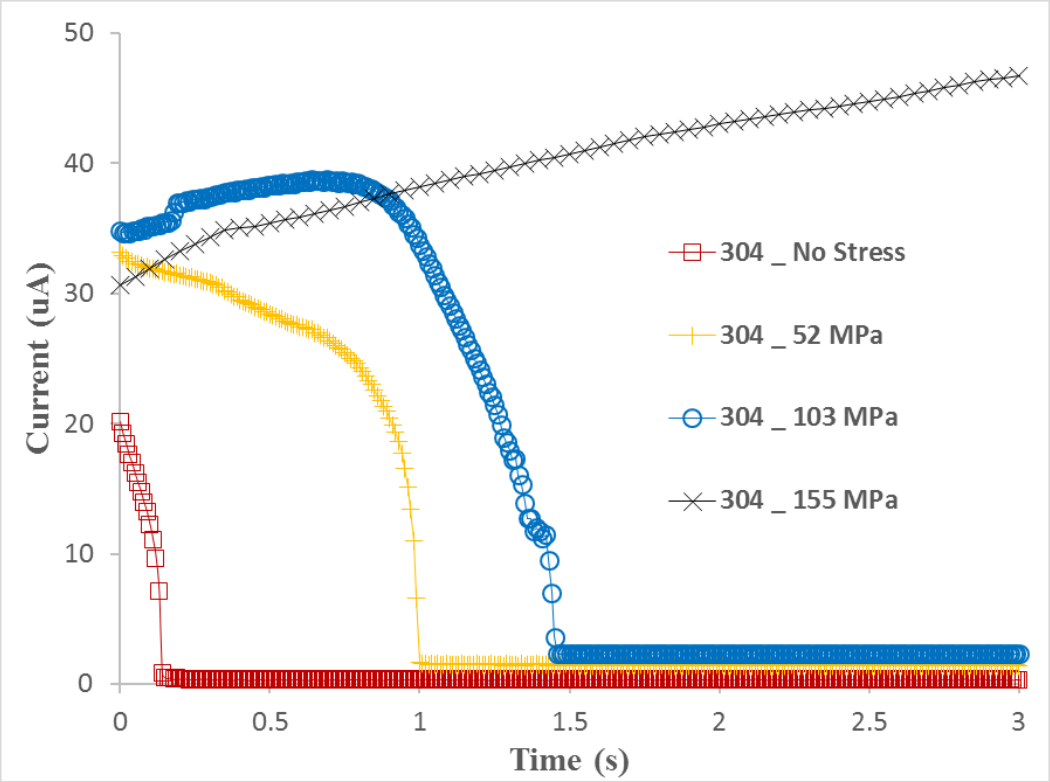

Figure 5-8. Pit-repassivation at +250 mV$_{(SCE)}$ immediately following pit initiation at +300 mV$_{(SCE)}$.

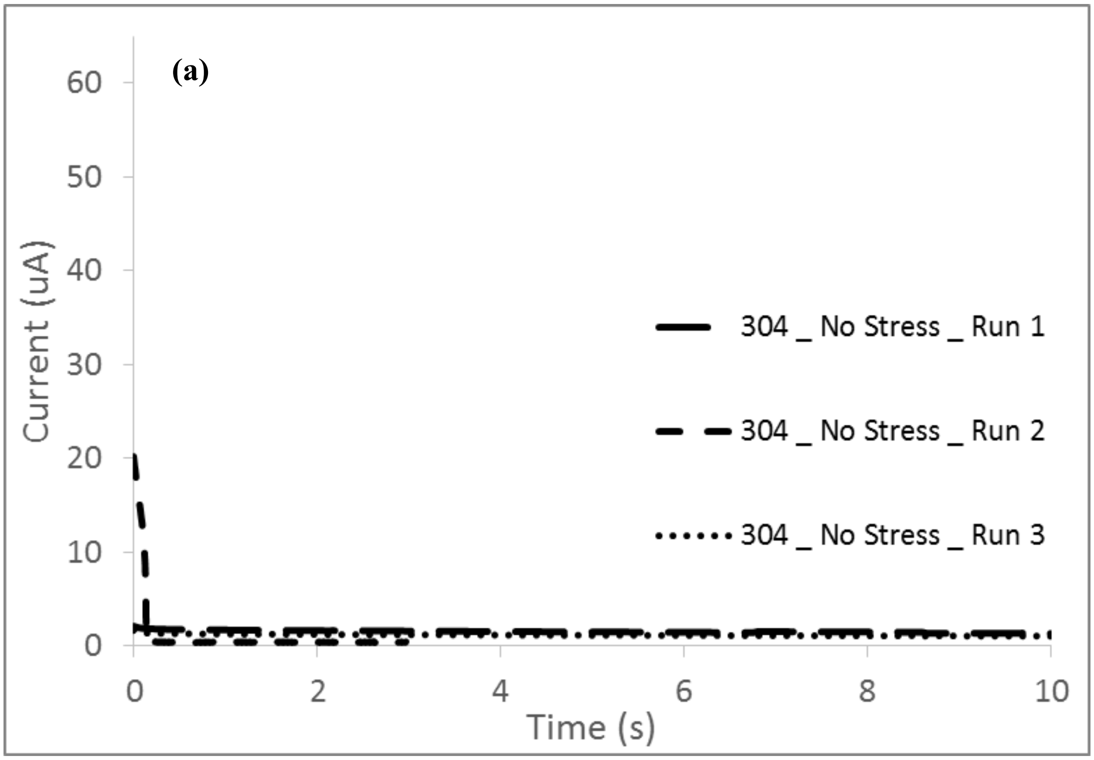

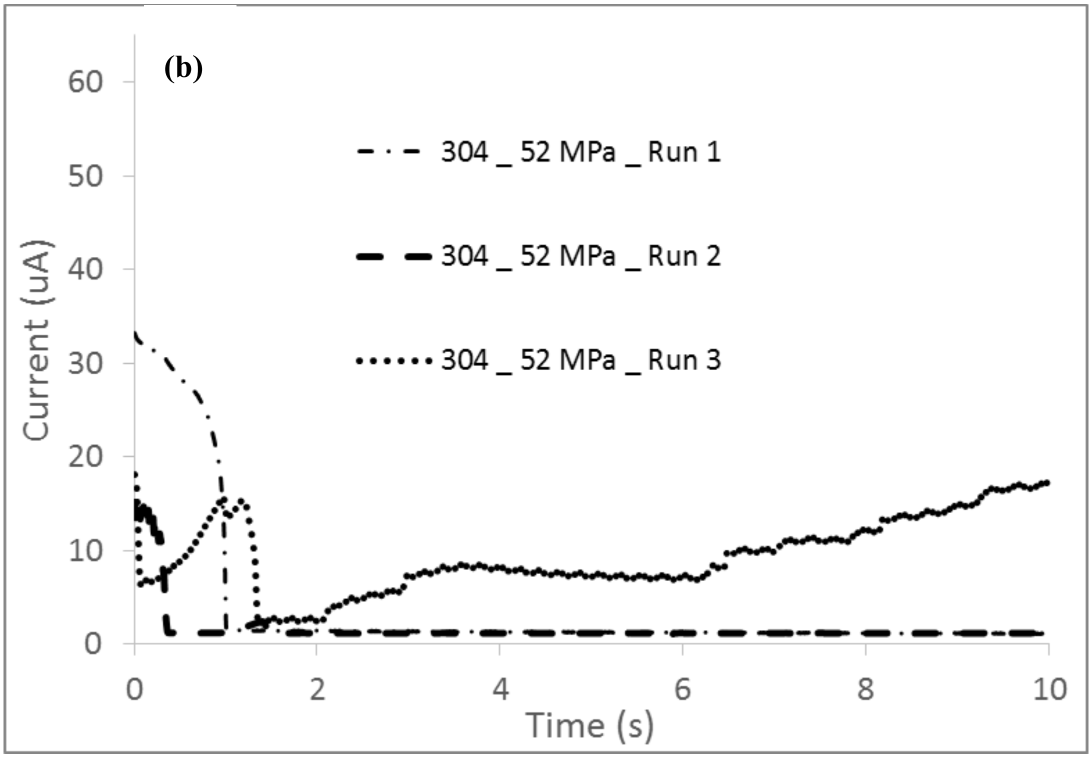

(b)
Current (uA)
0
10
20
30
40
50
60
Time (s)
0
2
4
6
8
10
304 _ 52 MPa _ Run 1
304 _ 52 MPa _ Run 2
304 _ 52 MPa _ Run 3

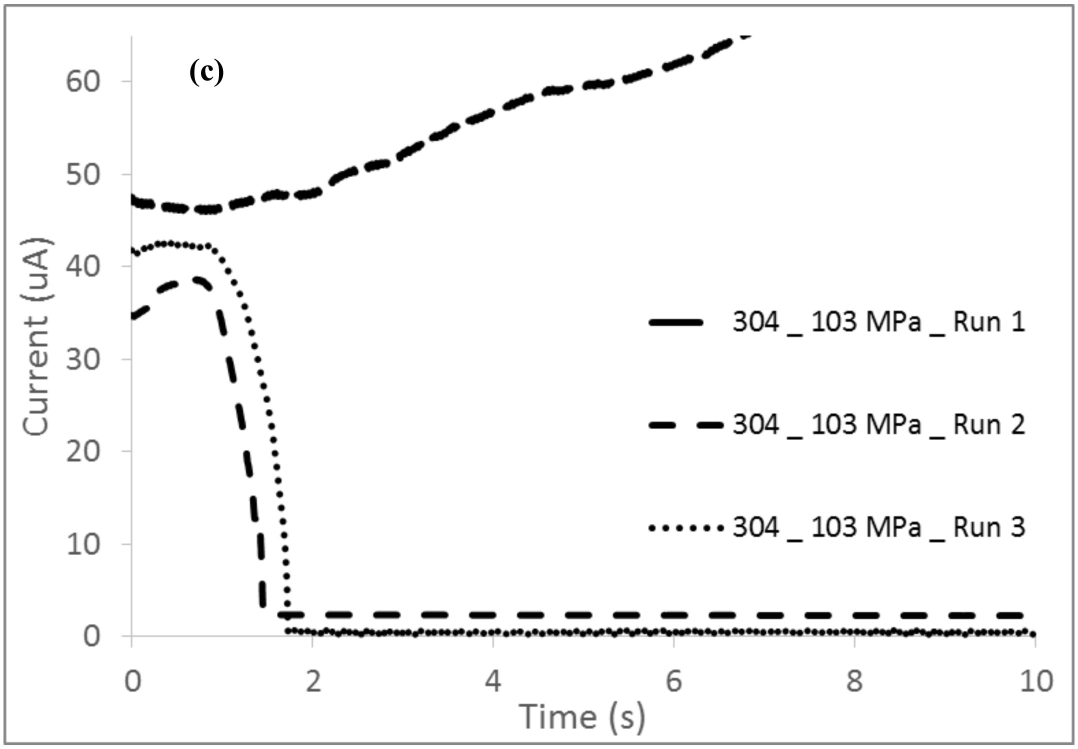

(c)
Current (uA)
0
10
20
30
40
50
60
Time (s)
0
2
4
6
8
10
304 _ 103 MPa _ Run 1
304 _ 103 MPa _ Run 2
304 _ 103 MPa _ Run 3

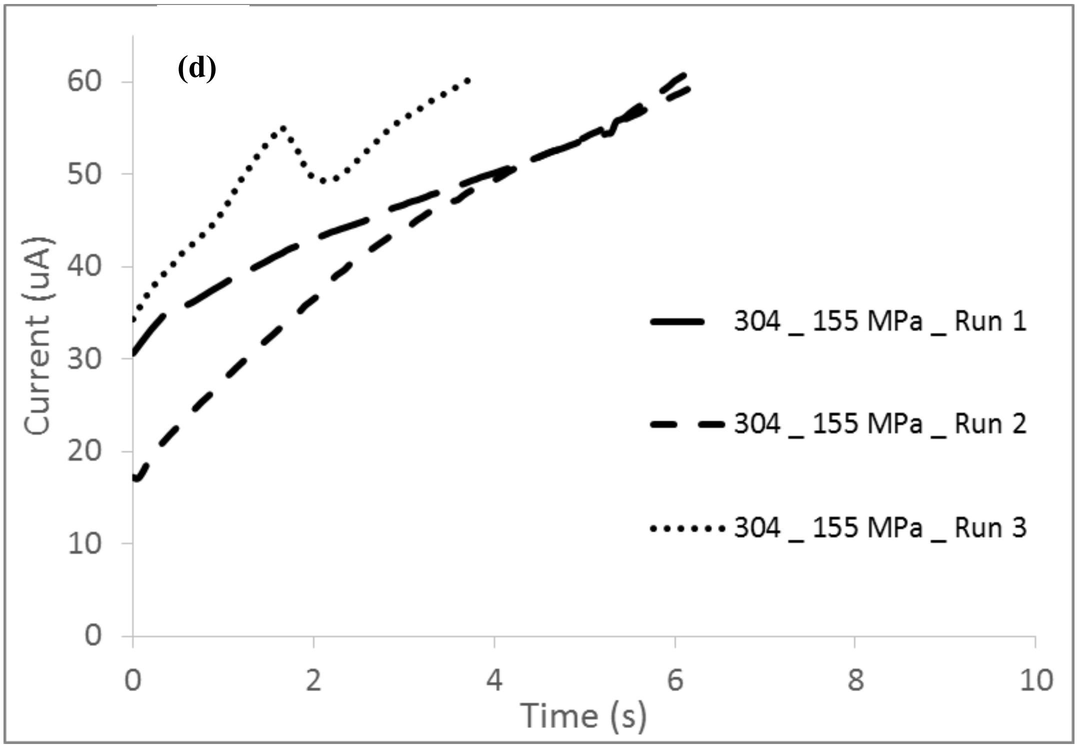

Figure 5-9. Three repetitions of pit-repassivation tests of SS 304 at four different stress levels: (a) no stress, (b) 52 MPa, (c) 103 MPa and (d) 155 MPa.

5.5 Effect of Elastic Stresses on Salt Film Stability inside Pits

A salt film usually forms to stabilize pit growth during pitting corrosion. Inside a propagating pit, a low pH is maintained which causes active dissolution of metal into metal cations inside the pit. To balance the charge neutrality, Cl^- ions or other anions are drawn into the pit solution. In addition, the hydrolysis of metal cations can induce a high concentration of metal hydroxide and release protons that will lower the pH inside the pit. When the concentration of metal salts, either metal hydroxide or metal chloride exceeds the solute solubility, a layer of salt film can be precipitated out near the pit opening as indicated in Fig. 5-10. The presence of the salt film governs the diffusion process across itself. Hence, the diffusion process becomes the driving force for the active dissolution inside the pit. According to Belk and Alkire, pit solutions can become saturated with a salt film within $10^{-8} – 10^{-4}$ seconds of pit initiation [126]. While a salt film is stable and complete, the chemistry inside the pits should gradually stabilize, thereby pit-growth is stabilized. During repassivation, the dissolution of metals inside salt film covered pits is either under activation control or under diffusion control.

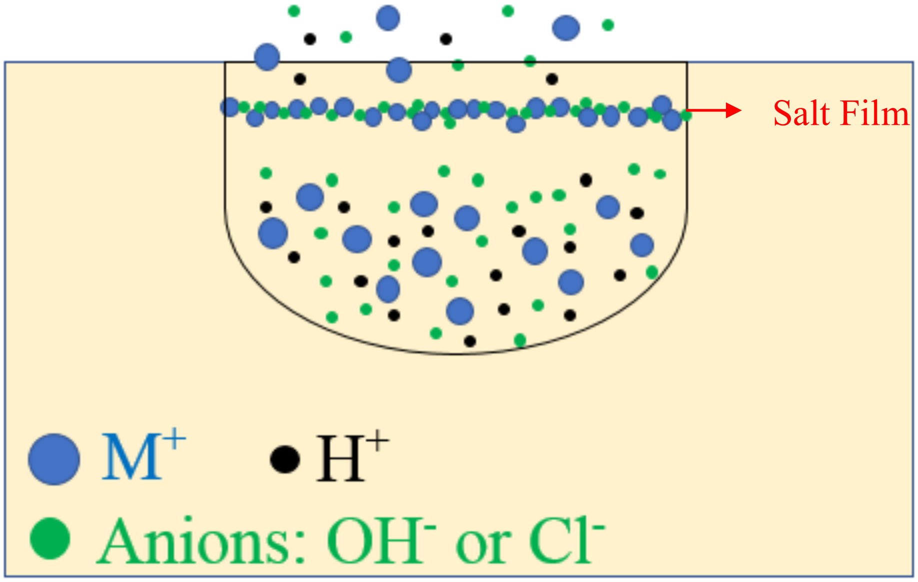

Figure 5-10. A schematic of salt-film formation near a pit opening.

To further investigate the pit growth behavior in the presence of the in-situ elastic stresses, the salt film stability was assessed during the pit-growth process. An ideal behavior of the salt film upon a reverse polarization scan was demonstrated in Fig. 5-11, where the potential is scanned from a high value to a low applied potential value. It is clear from the data in Fig. 5-11 that the salt film first enters the diffusion-controlled regime. In this regime, the Log current is independent of the applied potential. This is because the salt film remains in a steady state. In this steady state, two reactions reach an equilibrium: the salt film dissolving into the exterior environment and the new salts precipitating out to repair the salt film. Since the salt film governs the diffusion across the film, it limits the maximum dissolution current by controlling the diffusion process across the film. As the potential continues to decrease, the salt film starts to break down at lower potentials and is not able to recover. At or below that potential, a pit enters the activation-controlled regime, where Log Current is positively co-related the applied potential. The potential that separates these two regimes is defined as the transition potential, denoted as $E_{transition}$ in Fig. 5-11. In reality, the stability of the salt film can be disrupted even in the diffusion-controlled regime due to either electrocehmical or physical disturbances. It is common to see a repair behavior of the salt film as a slightly deviated version of the ideal behavior. A disturbance was intentionally created, as described in the next section, to investigate the salt film repair kinetics under the influence of applied elastic stresses.

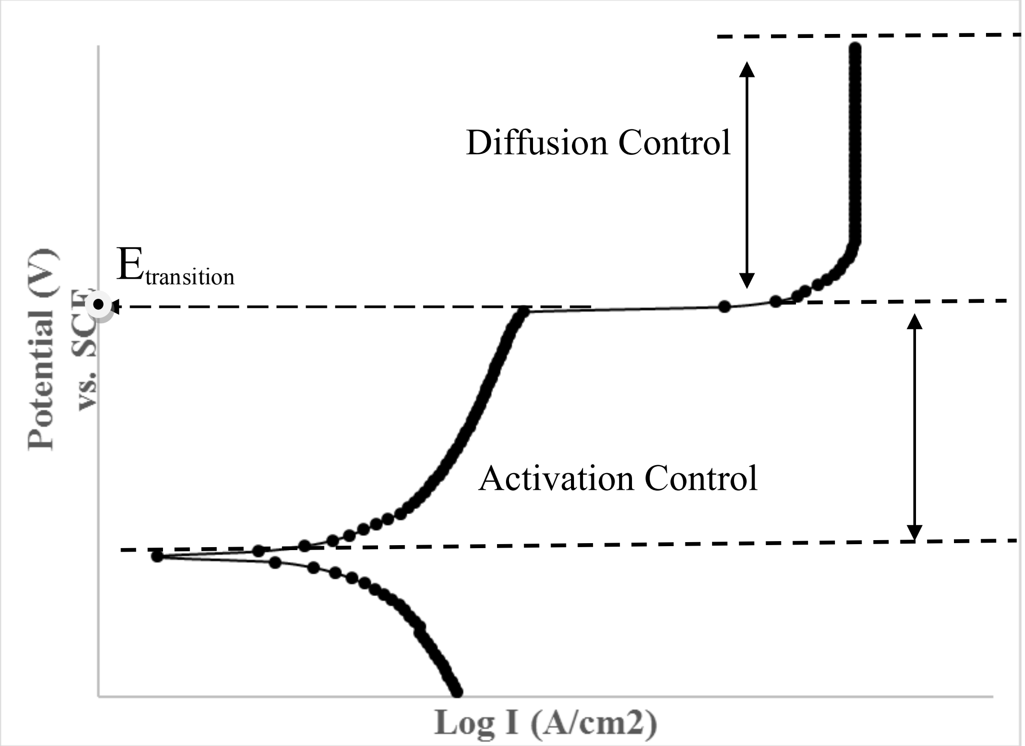

Figure 5-11. An ideal behavior of the salt film during a reverse polarization.

To study the pit-repassivation behavior of SS 304 under potentiodynamic control, a set of reverse polarization tests were performed on SS 304 tensile specimens, stressed separately to 0 MPa or 155 MPa, 3 seconds after a single-pit (initiation stopped at +40 μA) was initiated at +300 mV$_{(SCE)}$. The 3 seconds time lag was intentionally imposed as a disruption to the salt film. By doing this, the electrochemical driving force for pit growth was temporarily removed, allowing some loss of salt film to the exterior environments. This was evident from the lower current near +300 mV$_{(SCE)}$, since the pH of the pit solution was expected to increase when the salt film was not completely covering the pit surface. The comparison of the polarization curves are shown in Fig. 5-12, where the potential was scanned from +300 mV$_{(SCE)}$ to 0 mV$_{(SCE)}$ at a scan rate of 5 mV/s. This reverse polarization repassivates the initiated pit and the new OCP is established.

For the un-stressed 304 specimens, two types of polarization behavior were seen after at least 9 repetitions under same test conditions. Type 1 polarization behavior for an unstressed (0 MPa) sample exhibited a positively linear potential vs. log current correlation. This was indicative of an activation-controlled active dissolution within the pit. The Type 2 polarization curve of un-stressed sample was comprised of two types of dissolution behavior: firstly, diffusion control and then followed by activation control. It is reasonable to assume that the salt film was being repaired under diffusion control during the first regime of the reverse scan. This explains why the Type 2 curve of un-stressed sample slowly increased and then reached a steady state for a short range of potential, from +240 mV$_{(SCE)}$ to +220 mV$_{(SCE)}$.

During the salt film repair stage, the faster the active dissolution within a pit, the quicker a salt film can repair. As the potential kept decreasing, the salt film eventually broke down and the activation-controlled dissolution took over below the transition potential as marked in Fig. 5-11. Since the presence of salt film controls the diffusion of ions across the film, any loss of salt film can cause some degree of pH increase inside the pit. This can lead to higher pH and lower Cl- concentration inside the pit, further causing a decrease in the current value during the reverse potential scan. The key to stabilize the pit growth is to maintain a salt film inside the pit and guarantee its stability. The steady state of current density in the first active regime for the 155 MPa loaded SS 304 steel sample indicates that the active dissolution was governed by the salt film, and is therefore diffusion-controlled. This is in agreement with most pit-repassivation behavior reported in the literature [114, 126]. The elastically stressed (with 155 MPa applied stress) 304 specimen reached a steady state of current density in the diffusion-controlled regime almost immediately, while the active dissolution of unloaded specimen either entered the activation-controlled regime or took a lower value of potential to reach a steady state at roughly +220 $mV_{(SCE)}$. This data suggests that the kinetics of salt film repair was significantly faster when stress was applied.

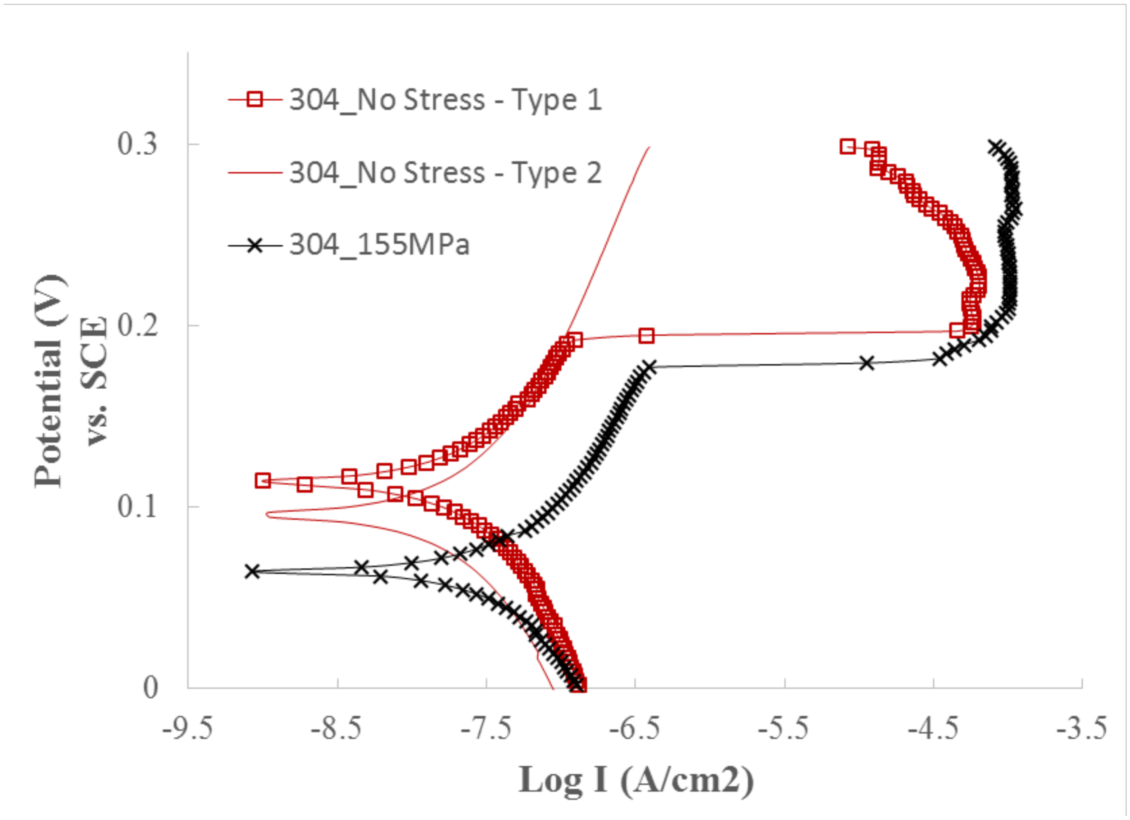

Figure 5-12. Pit-repassivation upon a reverse polarization behavior of SS 304 under no stress (0 MPa) and at 155 MPa.

5.6 A Proposed Mechanism to Explain the Stress Assisted Pit-Growth Process

Stress acting as an additional driving force has been reported to accelerate active dissolution [16, 29]. A stress concentration is developed around the 3-D pit geometry for the elastically stressed sample, with 155 MPa applied stress. Especially when a salt film is not complete, this could result into an accelerated active dissolution in a saturated pit solution, thereby precipitating out new salt film for a quicker repair. It was also noticed that the active dissolution current density was higher for the sample with 155 MPa applied stress than that for the unstressed sample throughout the polarization scan. It means that the active dissolution inside the pit during the reverse polarization was enhanced for the stressed sample regardless of whether it was in the diffusion-controlled regime or the activation-controlled regime.

As summarized in Fig. 5-13, the average transition potential (over 6 repeated tests under similar conditions) for the sample loaded at 155 MPa, roughly +156.0 ± 11.3 $mV_{(SCE)}$ was significantly lower than the transition potential for the unstressed sample which was around +200.4 ± 9.7 $mV_{(SCE)}$. This indicates that the potential range for the salt film stability was extended by ~44 $mV_{(SCE)}$ when the stress was applied. Analyzing the activation-controlled regime of polarization behavior, not only the elastically stressed sample (155 MPa) exhibited a higher current, it also lowered the newly established OCP by roughly +25 $mV_{(SCE)}$ as indicated in Fig. 5-13. It can be then further deduced that a lower pH was present within the pit developed under stresses during repassivation. This can be ascribed to the extended salt-film stability range, which helped to sustain a low pH up to a lower potential level. In addition, the strain-accelerated active dissolution can also lead to a lower pH during repassivation. Therefore, a model is proposed to account for the stress-assisted pit growth process. The proposed effects of applied elastic stresses on pitting corrosion of stainless steels is following:

- Once a pit is initiated under stresses, a 3-D pit cavity/geometry is developed, occluded with a low pH and a high concentration of Cl^-. As a result, a salt film forms within the pit.

- The salt film reaches a steady state through a competing mechanism between film breakdown and film repair.

- The pit's interior surfaces experience an amplified stress state due to the stress concentration developed around the pit, which enhances the tendency of active dissolution during the pit growth stage.

- The resultant effect is two folds:

  1. Firstly, it accelerates the salt saturation in the pit solution, leading a quicker salt film repair when the salt film is lost to environments. This stabilizes the pit growth.

  2. Secondly, during repassivation, it maintains a lower pH through a more complete hydrolysis by providing more metal cations. This hinders the repassivation kinetics for pitting corrosion.

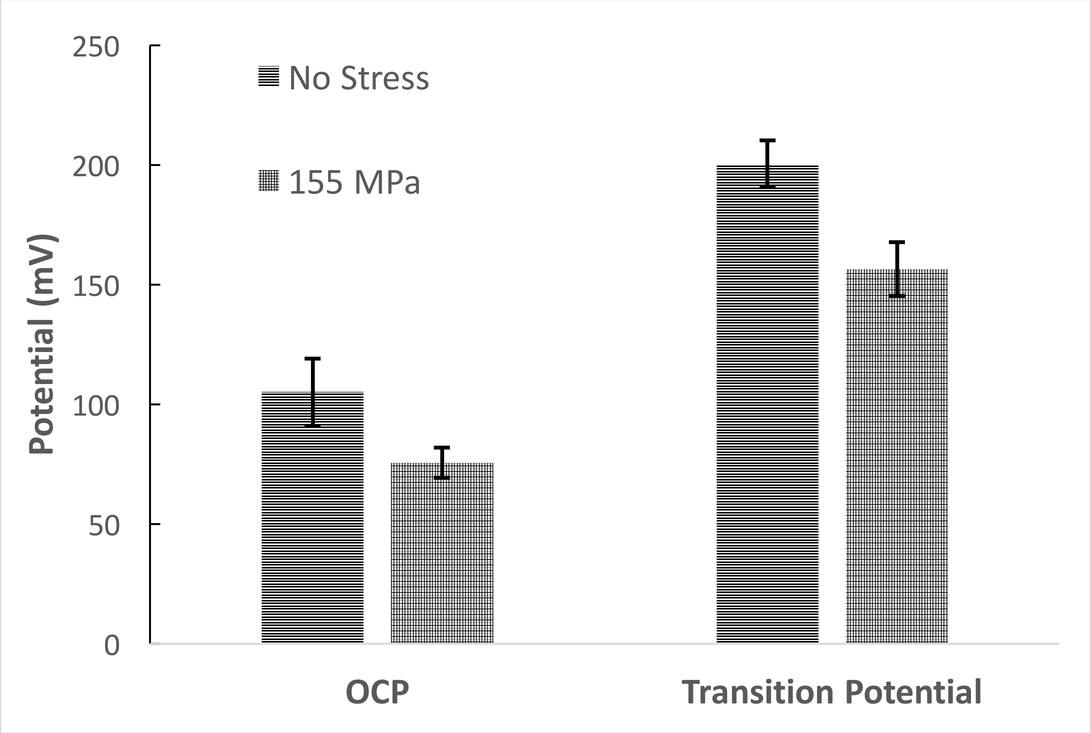

Figure 5-13. Statistical summary of transition potential and newly-establish OCP for sample with no stress applied (0MPa) and at a 155 MPa stress level during the reverse scan.

5.7 Effect of Elastic Stresses on Repassivation and on Re-initiation of Pits

To determine whether the repassivated pit sites can re-initiate pit growth under applied elastic stresses, a new set of samples were tested with applied elastic stresses of 155 MPa, where a single-pit was initiated at +300 $mV_{(SCE)}$. As soon as the current transient reached +40 μA, the applied potential was immediately changed to 0 $mV_{(SCE)}$ and held for 10 minutes to repassivate the initiated pit. The potential was then held at +250 $mV_{(SCE)}$ to monitor the current response as indicated in Fig. 5-14. A sudden current increase was not seen until about 500 s, unlike for the equivalent test at 155 MPa without the repassivation step where the current kept growing without any signs of repassivation. The surface was examined under an optical microscope, and two separate pits were observed after the sample with a single repassivated pit was held at +250 $mV_{(SCE)}$. The fact that the two pits were not near each other suggested that a repassivated pit did not necessarily act as a preferential pit-initiation site even if the resultant occluded cavity might experience an amplified state of stress field due to the stress concentration developed around the 3-D geometry. Therefore, two key factors are necessary for a repassivated pit initiated at +300 $mV_{(SCE)}$ to stabilize pit growth at +250 $mV_{(SCE)}$: its resultant pit chemistry/solution and stress.

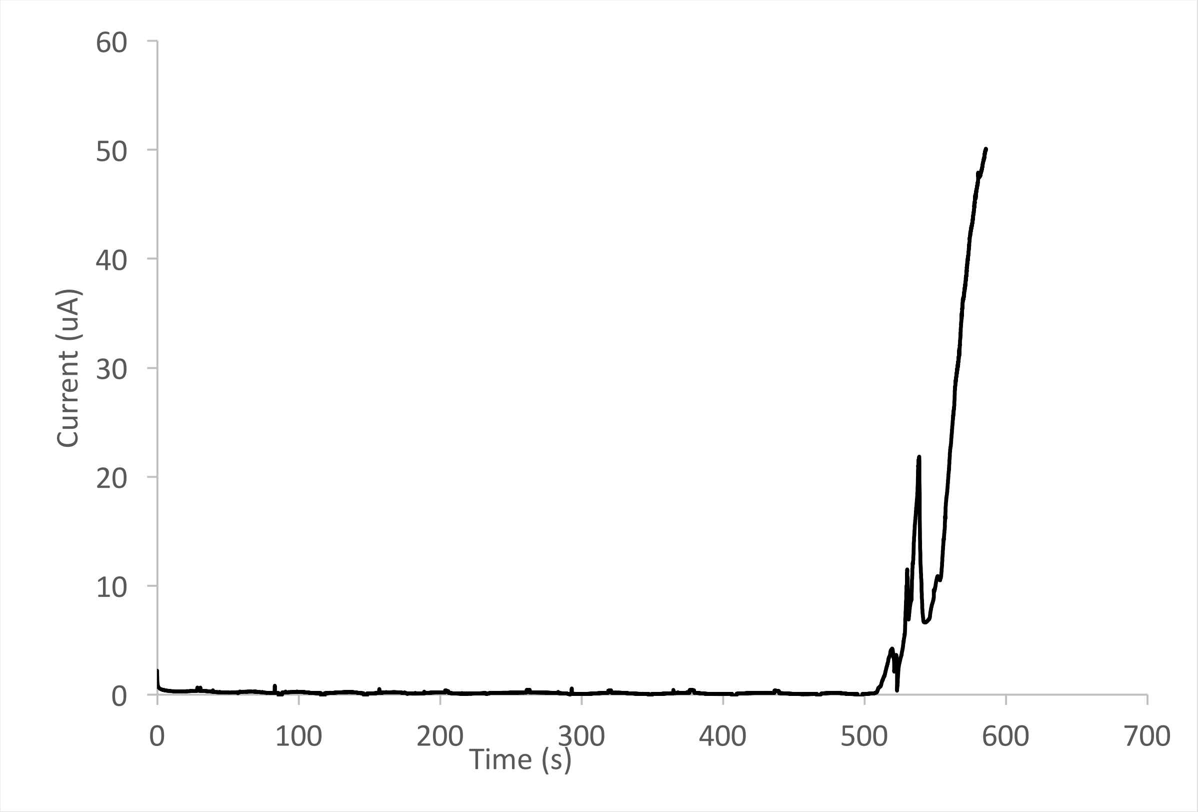

Figure 5-14. Current response of SS 304 loaded at 155 MPa at +250 $mV_{(SCE)}$ following a 40-uA pit initiation at +300 $mV_{(SCE)}$ and repassivation at 0 $mV_{(SCE)}$ for 10 mins.

5.8 Conclusions

Following conclusions on the effect of applied elastic stresses on pitting corrosion behavior of austenitic stainless steel 304L can be drawn from the results discussed:

- The presence of in-situ elastic stresses impedes the pitting resistance of SS 304 in Cl^--containing environments by stabilizing the pit growth.

- A more protective passive film resulted from pre-oxidation can help to increase the pitting potential, but the negative effect of elastic stresses was still observed regardless of the composition of passive films formed on the SS 304 samples.

- Metastable pitting was more dominant when lower stresses were applied in the 0.1 M NaCl solution at 50 ^{o}C, while higher elastic stresses tend to transit metastable pitting to stable pitting.

- In-situ elastic stresses stabilize pit growth by accelerating salt-film repair kinetics and extending the stability potential range for the salt film through a proposed mechanism in section 5.6.

- A repassivated pit-initiation site did not necessarily act as a preferential pit-initiation site.

CHAPTER 6. EFFECT OF PLASTIC DEFORMATION ON PITTING CORROSION

This chapter describes the effect of plastic deformation on pitting corrosion behavior of SS 304. Two different methods, an in-situ straining of tensile sample and cold-rolling were utilized to apply different amounts of plastic deformation to SS 304. Plastic deformation introduced surface defects and an increase in the internal energy with an increase in the structural defects in the material. The resultant pitting corrosion behavior for plastically deformed SS 304 was compared with the similar tests done after applying elastic stresses.

6.1 Effect of Plastic Deformation on Pitting Resistance of SS 304

Before discussing the electrochemical results of plastically deformed SS 304, the surface morphology was examined under the scanning electron microscope (SEM). The most prominent change upon tensile plastic deformation was the appearance of slip-steps as shown in Fig. 6-1. These surface defects were also examined using a non-contact laser profilometer. The depth contour of these surface defects was depicted in Fig. 6-2. The density of these surface defects was observed to increase as the applied strain increased up to 9%. A set of cyclipolarization tests was done in 0.1 M NaCl at 50 ^{o}C by applying three strain levels, namely 0.1% (yield strain), 2% and 9%. The average pitting potentials over at least 3 repetitions were plotted in Fig. 6-3, along with the results obtained in the elastic range. Constant strain values were applied to the sample throughout the test. It was clear that the pitting potential decreased up to the yield stress/strain. However, the decreasing trend of pitting potential ceased beyond yield stress. Further plastic strain does not decrease the pitting potential of SS 304 any further. These results suggested that the effect of in-situ plastic deformation on pitting resistance did not exceed the limit set by the onset of plastic strain.

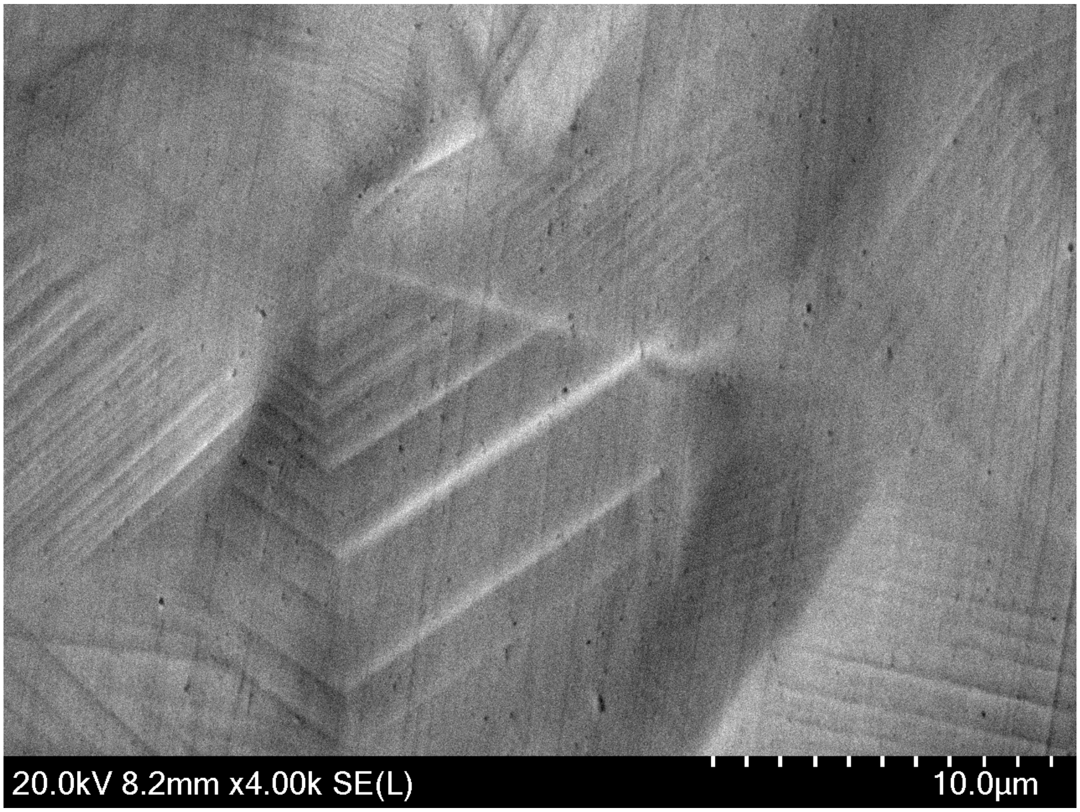

Figure 6-1. Appearance of slip-steps on a SS 304 surface upon tensile plastic deformation.

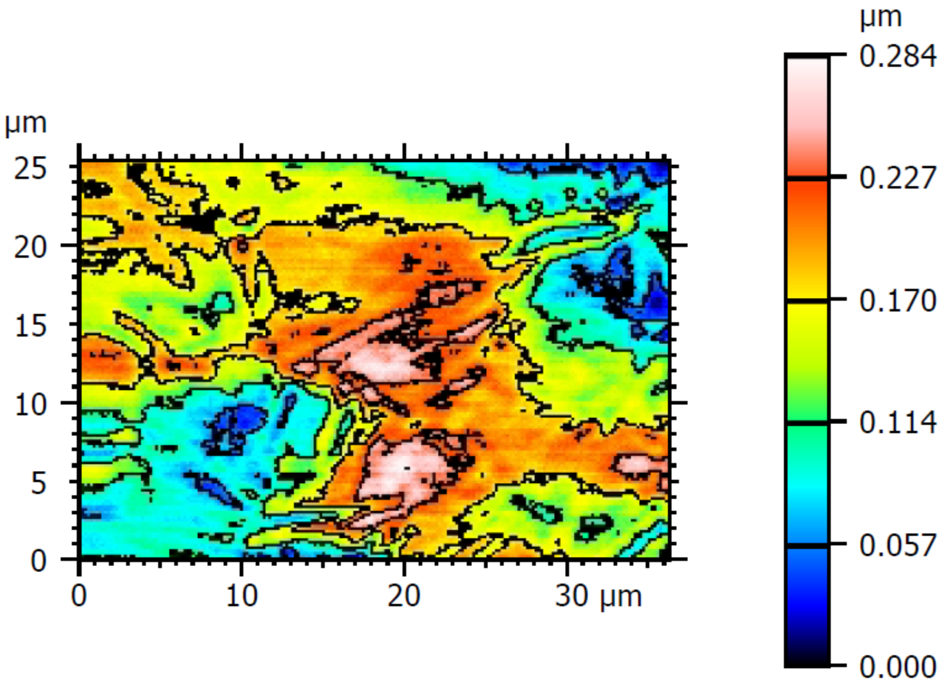

Figure 6-2. A representative depth contour of surface defects due to plastic deformation.

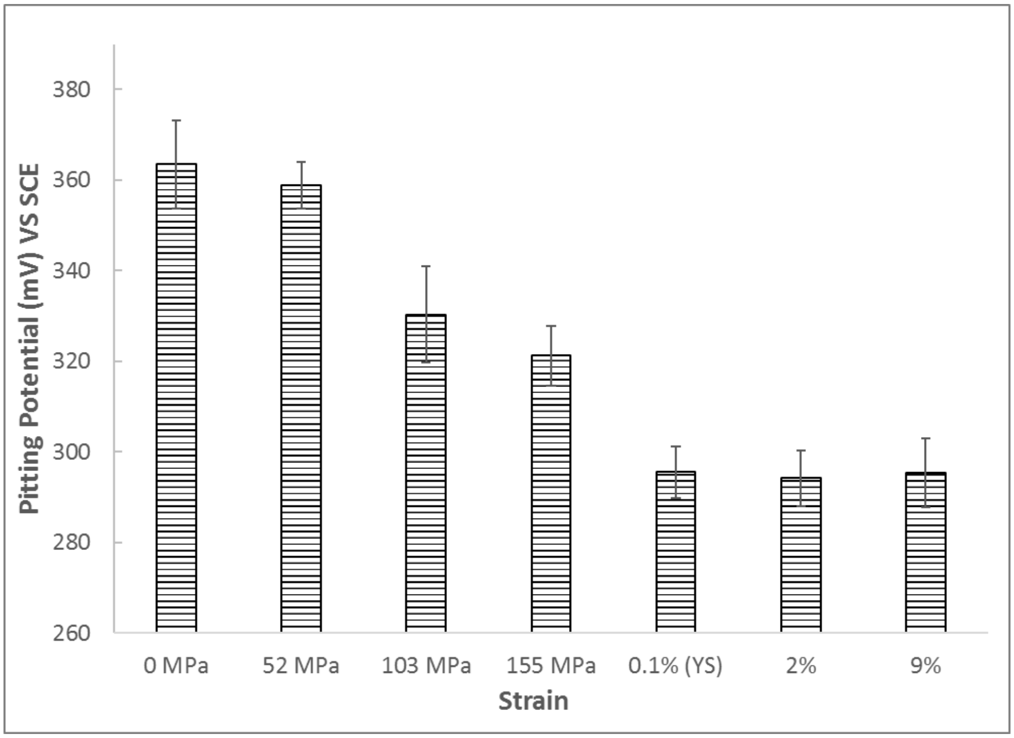

Figure 6-3. Average pitting potential with respect to applied in-situ elastic stresses and applied in-situ plastic strain.

However, one question that was not addressed was whether the release of elastic stresses upon unloading a plastically deformed sample had an impact on pitting resistance of SS 304. Another set of cyclic polarization was done where the sample was plastically strained to the desired values and then unloaded, so that the elastic stresses were released. The plastic residual strain was mainly comprised of surface defects like slip-lines and structural defects like dislocations in the material. As a comparison, the average pitting potential of SS 304 under residual plastic strain (over at least 3 repetitions) was plotted in Fig. 6-4, along with the ones under applied in-situ strain and two other conditions, namely no strain (0%) and a sample repolished after 9% strain. By comparing the pitting potentials at the same strain level, but in the in-situ strain-condition and in the plastic residual strain-condition, there was a difference in the pitting potential. The smaller is the value of plastic residual strain, the more the pitting potential can recover upon unloading towards the no-strain condition indicated by the value at 0%. It was observed that the sample with a high plastic residual strain of 9% did not show any recovery in pitting resistance upon unloading. This was likely because of the surface structural defects, like shown in Fig. 6-1 that were more prone to pitting attack.

It was often observed that pitting events occurred in the areas where these surface defects are concentrated, as indicated in Fig. 6-5. These surface defects are localized high-energy areas, and it was reported that these high-energy defects could act as an anodic site with respect to the bulk material [105]. Since cyclic-polarization tests only captured the first stable-pitting event, it made sense that the susceptibility to pitting corrosion increased to a plateau as the density of these surface defects increased to a critical value, 9% plastic strain in this case.

A specimen was strained to 9% strain and then re-polished to remove the plastic deformation/roughness from the surface. The corresponding pitting potential completely recovered to the no-strain condition as demonstrated by the results in Fig. 6-4. This meant that re-polishing had removed the surface defects formed by plastic deformation. Since the metals' susceptibility to pitting corrosion is extremely dependent on surface conditions, re-polishing alleviated the surface condition to a large degree and the pitting resistance of re-polished SS 304 was completely recovered. It is also well known that plastic deformation causes martensitic transformation in austenitic stainless steel 304. About 10% of martensite was expected to be induced at a strain level of 9% [2]. However, it seemed like that the presence of martensite within the bulk material did not significantly altered the pitting potentials of SS 304, by directly comparing the pitting potentials at 0% strain and at 9%_repolished.

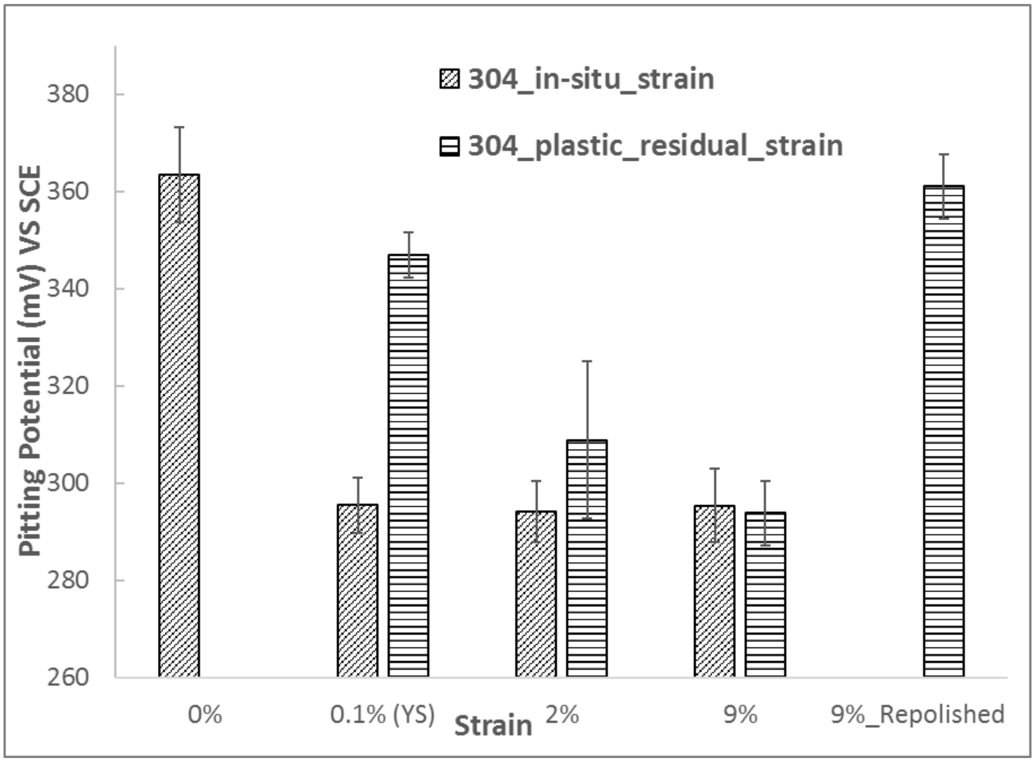

Figure 6-4. Average pitting potential with respect to different strain-conditions.

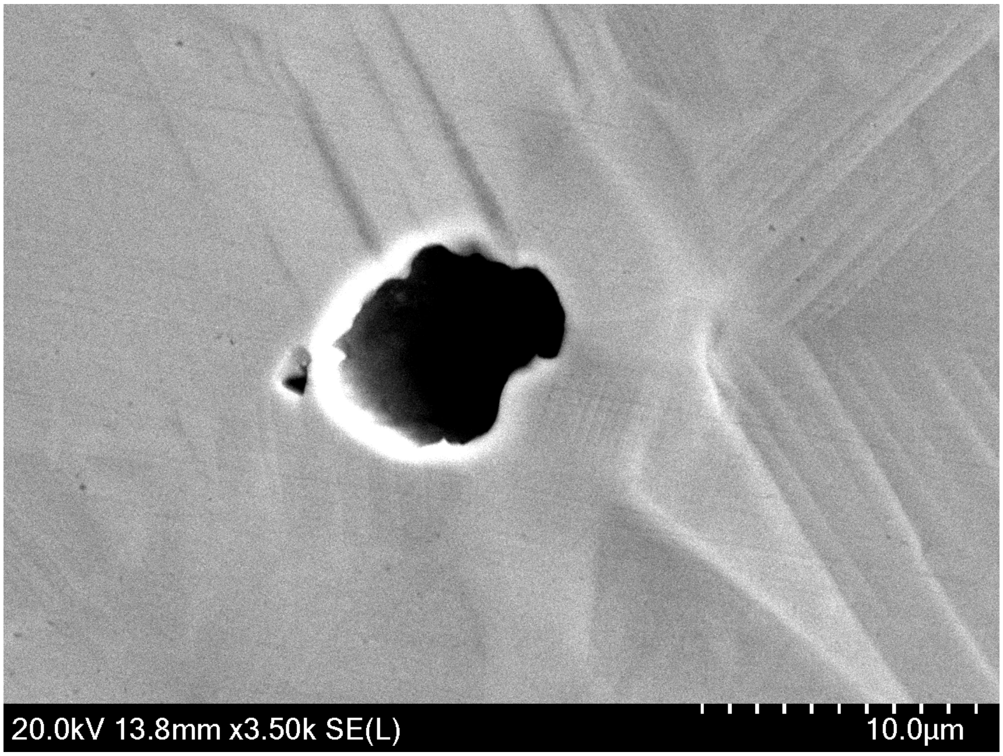

Figure 6-5. Observation of pit occurrence associated with surface structural defects (slip-steps in this case).

6.2 Microstructural Evolution of SS 304 upon Cold-rolling

To investigate the effect of cold-rolling (CR) on pitting corrosion of SS 304, mill-annealed 304 samples were cold-rolled to four thickness reduction levels of 5%, 10%, 25% and 50%. The microstructural evolution for the cold-rolled samples is demonstrated in Fig. 6-6, from the as-annealed condition to the most heavily cold-rolled condition. It was observed that the density of twins increased with an increase in the percentage CR. In addition, the appearance of martensite laths became very clear at high levels of cold-rolling, especially at 50% CR. X-ray diffraction (XRD) was used to semi-quantitatively evaluate the content of martensite induced during cold-rolling as shown in Fig. 6-7, where austenite peaks are indicated as blue and martensite peaks are indicated as green. The relative counts of martensite peaks increased as the percentage of cold-rolling increased, indicating that a high degree of cold-rolling induced a high content of martensite. Taking the as-annealed sample as a baseline, the relative martensite contents of SS 304 at different cold-rolling levels were listed in Table 6-1. A monotonically increasing trend of martensite content was exhibited as the degree of cold-rolling increased. It was worth noticing that a steep increase from 12.3% to 30.3% in the martensite content occurred from 25% CR to 50% CR. It meant that martensitic transformation was intensively induced in this range. Since the interface between the martensite and the parental austenite bore a concentrated strain field [22, 23, 103], one can expect the significant strain energy can be stored in this interface upon martensitic transformation.

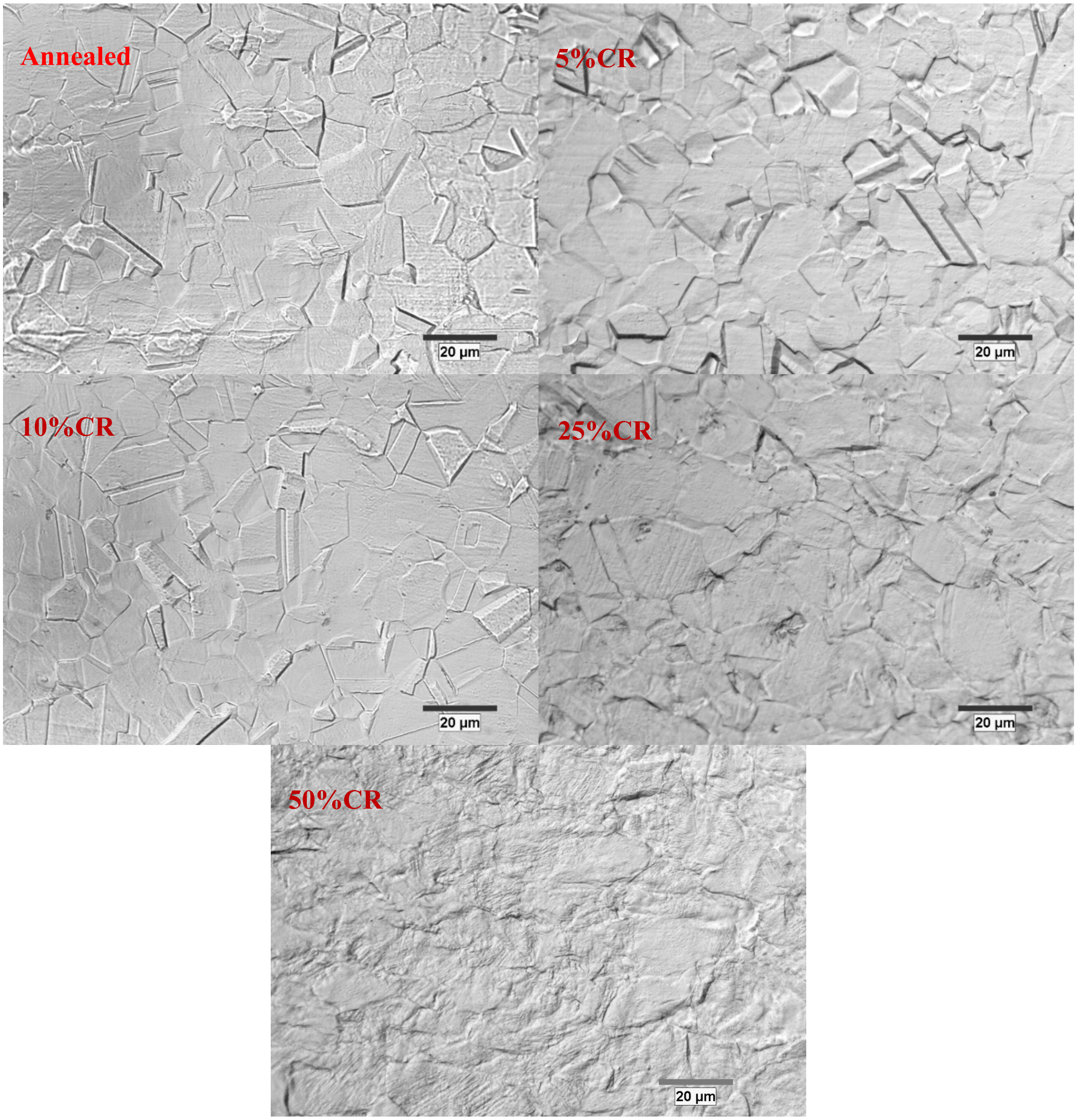

Figure 6-6. Microstructural evolution of SS 304 from the annealed condition to four cold-rolled conditions (5% CR, 10% CR, 25% CR and 50% CR).

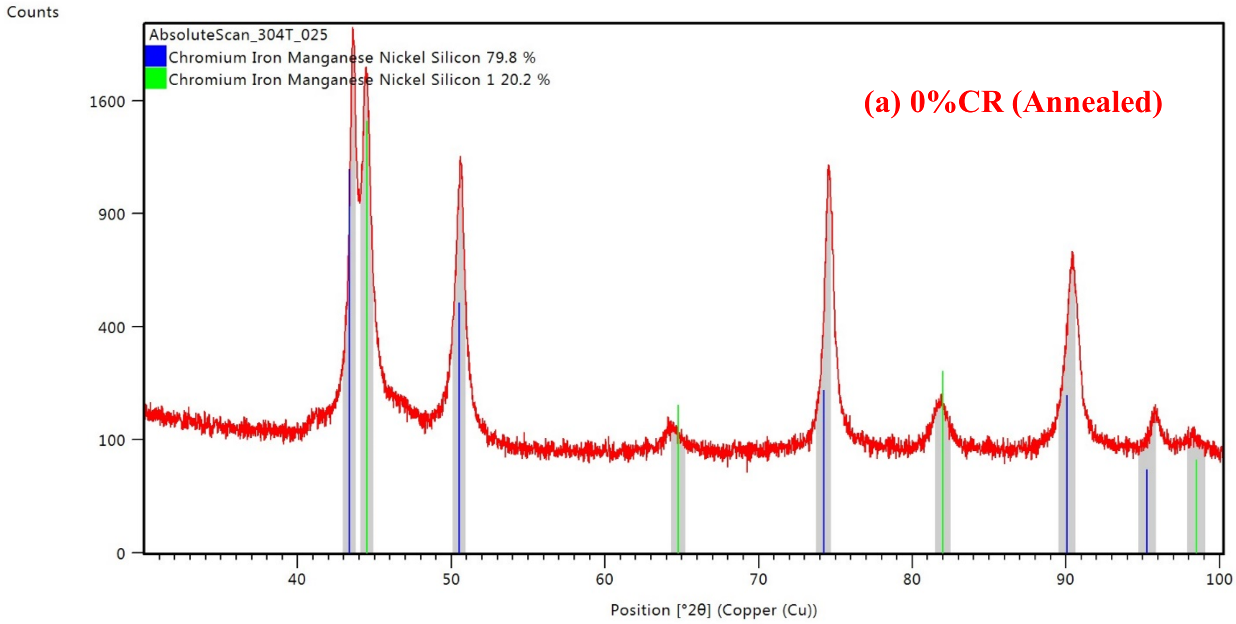
Counts
AbsoluteScan_304T_025
🟦 Chromium Iron Manganese Nickel Silicon 79.8 %
🟩 Chromium Iron Manganese Nickel Silicon 1 20.2 %
(a) 0%CR (Annealed)
1600
900
400
100
0
40
50
60
70
80
90
100
Position [°2θ] (Copper (Cu))

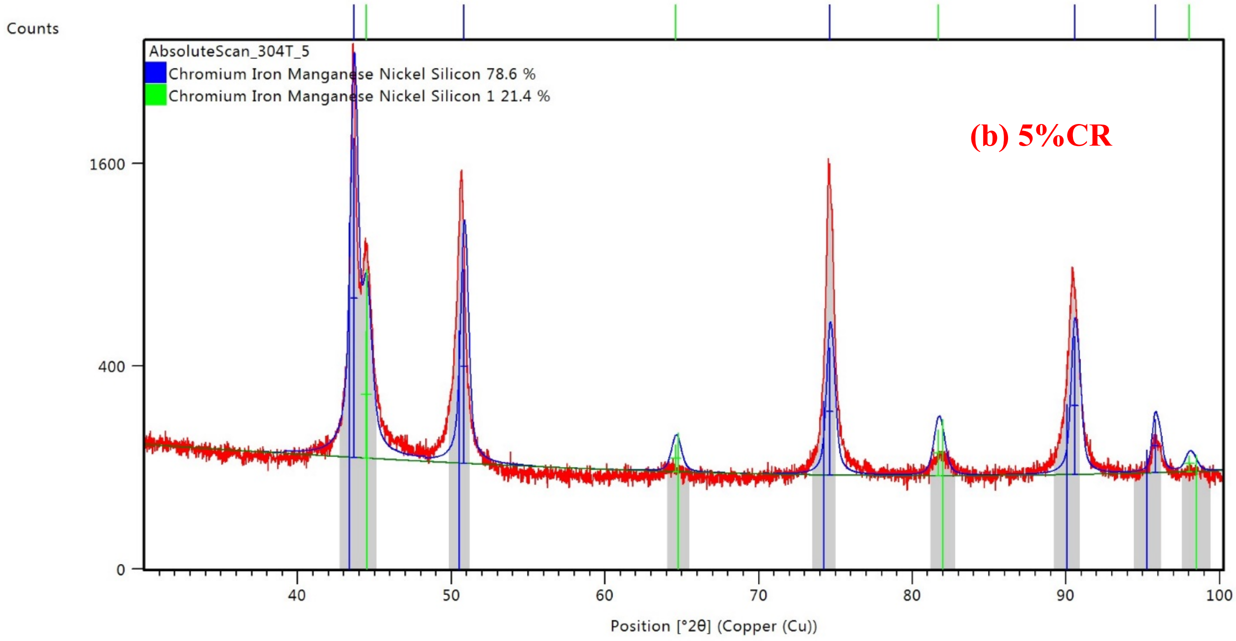
Counts
AbsoluteScan_304T_5
🟦 Chromium Iron Manganese Nickel Silicon 78.6 %
🟩 Chromium Iron Manganese Nickel Silicon 1 21.4 %
(b) 5%CR
1600
400
0
40
50
60
70
80
90
100
Position [°2θ] (Copper (Cu))

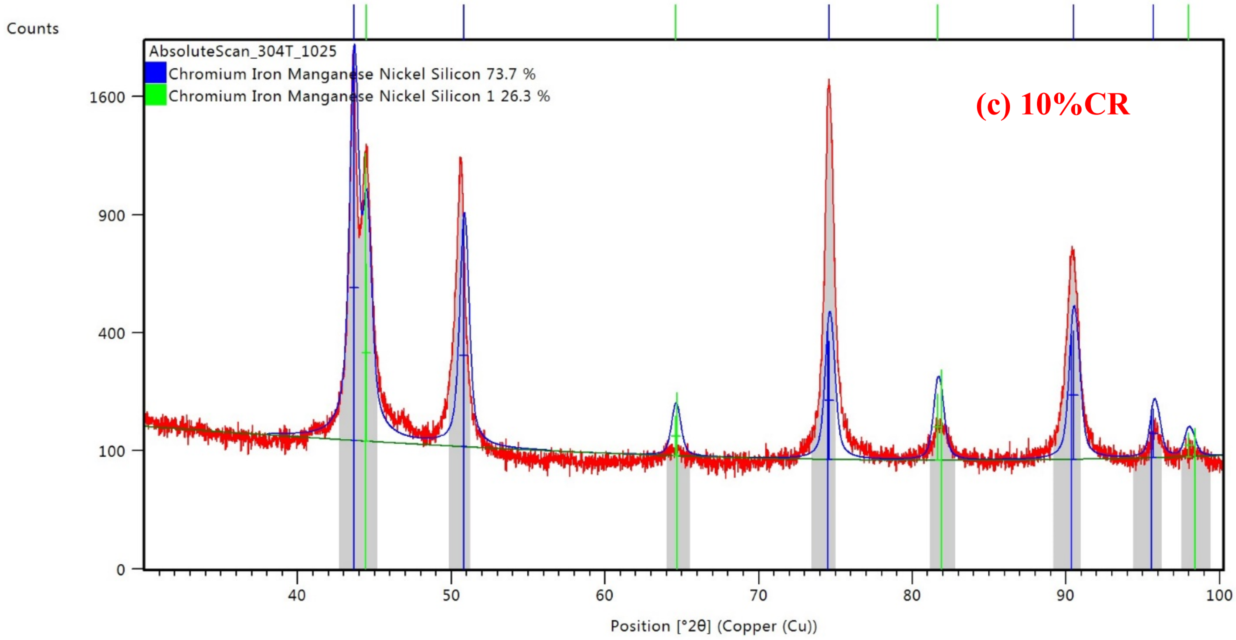
Counts
AbsoluteScan_304T_1025
Chromium Iron Manganese Nickel Silicon 73.7 %
Chromium Iron Manganese Nickel Silicon 1 26.3 %
(c) 10%CR
1600
900
400
100
0
40
50
60
70
80
90
100
Position [°2θ] (Copper (Cu))

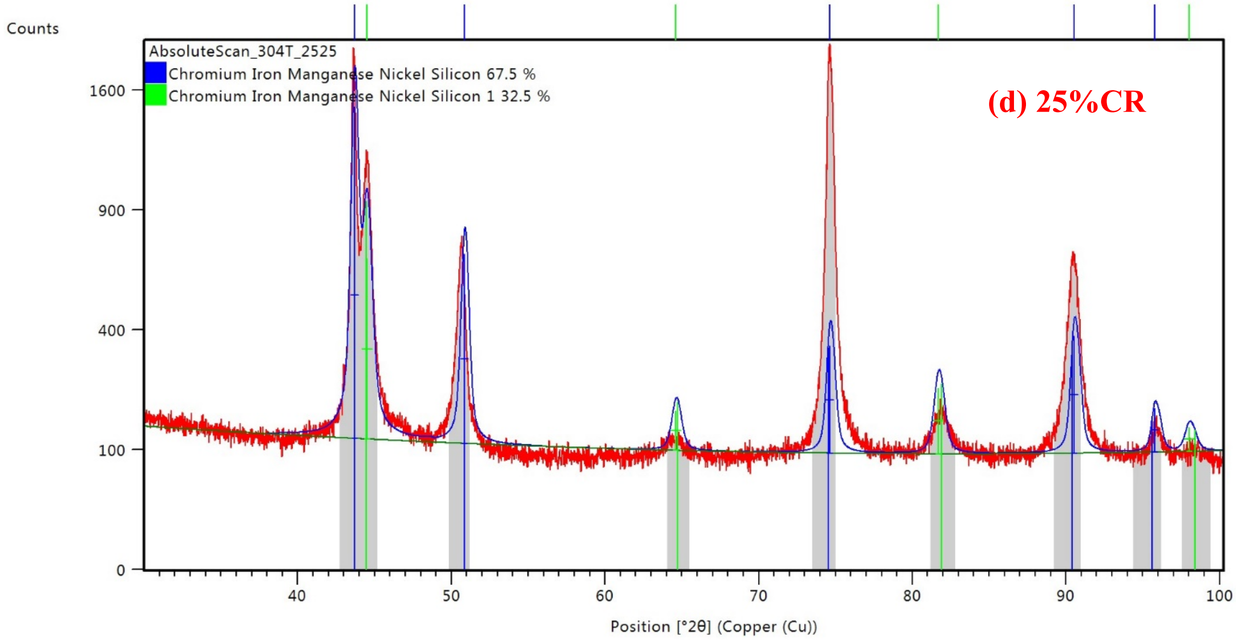
Counts
AbsoluteScan_304T_2525
Chromium Iron Manganese Nickel Silicon 67.5 %
Chromium Iron Manganese Nickel Silicon 1 32.5 %
(d) 25%CR
1600
900
400
100
0
40
50
60
70
80
90
100
Position [°2θ] (Copper (Cu))

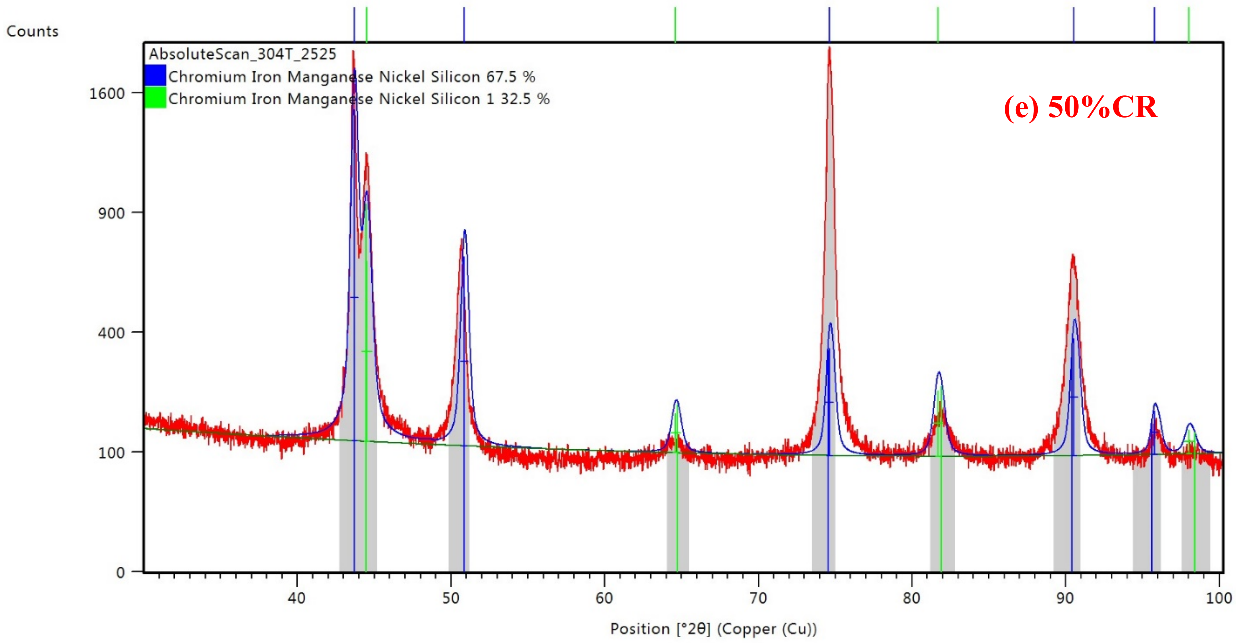

Figure 6-7. XRD scans of SS 304 samples cold-rolled to 0%CR (annealed), 5%CR, 10%CR, 25%CR and 50%CR respectively.

Table 6-1. Relative martensite contents of SS 304 at different cold-rolling levels.

%CR	**Annealed**	**5%**	**10%**	**25%**	**50%**
%Martensite	0	1.2%	6.1%	12.3%	30.3%

6.3 Effect of Cold-rolling on Pitting Corrosion

To evaluate the effect of cold-rolling on pitting corrosion of SS 304, a set of polarization tests was performed in 0.1 M NaCl at 50 ^{o}C as shown in Fig. 6-8. The average pitting potential was based on 5 test repetitions under each test condition and the results are as shown in Fig. 6-9. No distinct trend of the pitting potential was observed across the 5 different cold-rolling levels, namely the annealed condition (0%CR), 5%CR, 10%CR, 25%CR and 50%CR. This was likely because all test specimens were re-polished before testing to remove many embedded impurities and debris on the as-rolled surfaces. As discussed for the re-polished 9%-strained tensile specimen in section 6.3, the surface roughness or plastic deformation was removed due to surface polishing. Even the passive films formed on the specimen surfaces were formed on the newly polished surface. The prior surface defects/roughness were eliminated by re-polishing, so the new surfaces of did not exhibit any observable trend in pitting corrosion unlike that for the in-situ plastic strain tests. It further confirmed that pitting corrosion was a strongly dependent on surface conditions, and surface defects created by plastic deformation contributed a major damage to the pitting resistance of SS 304 with residual plastic strain.

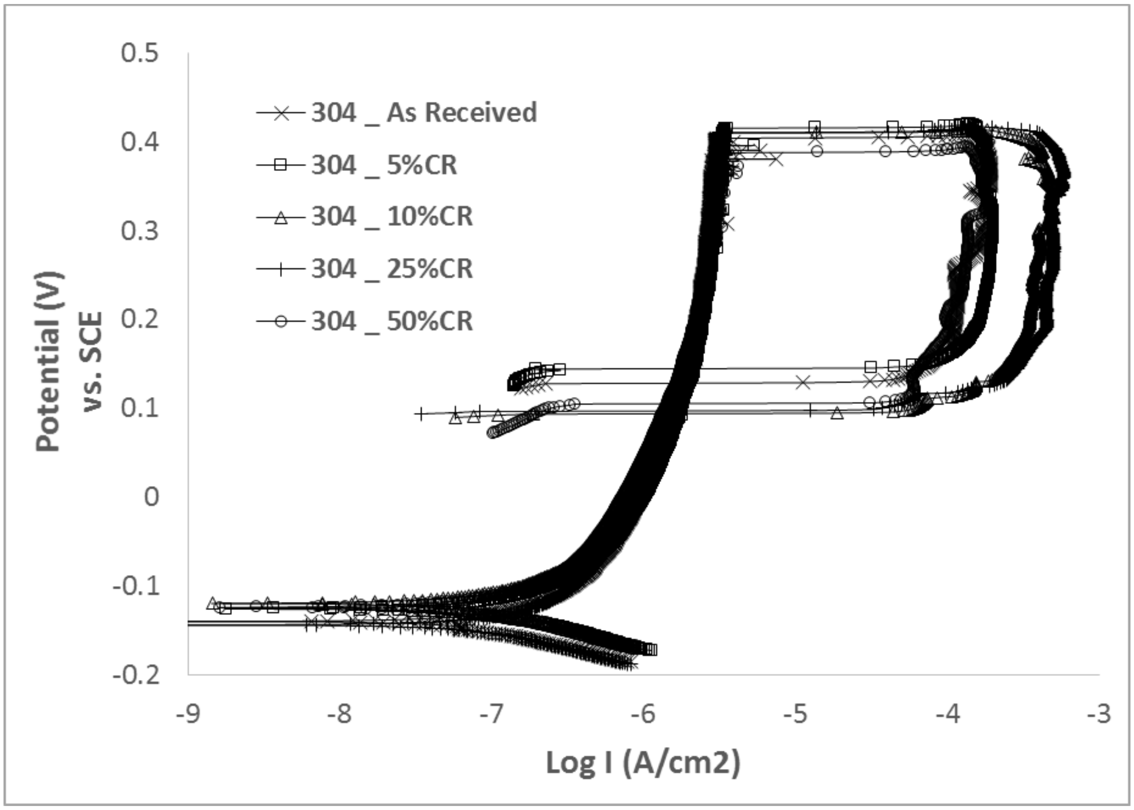

Figure 6-8. Cyclic polarization behavior for SS 304 specimens as received, 5% CR, 10% CR, 25% CR, and 50% CR specimens in 0.1 M NaCl solution at 50 ^{o}C.

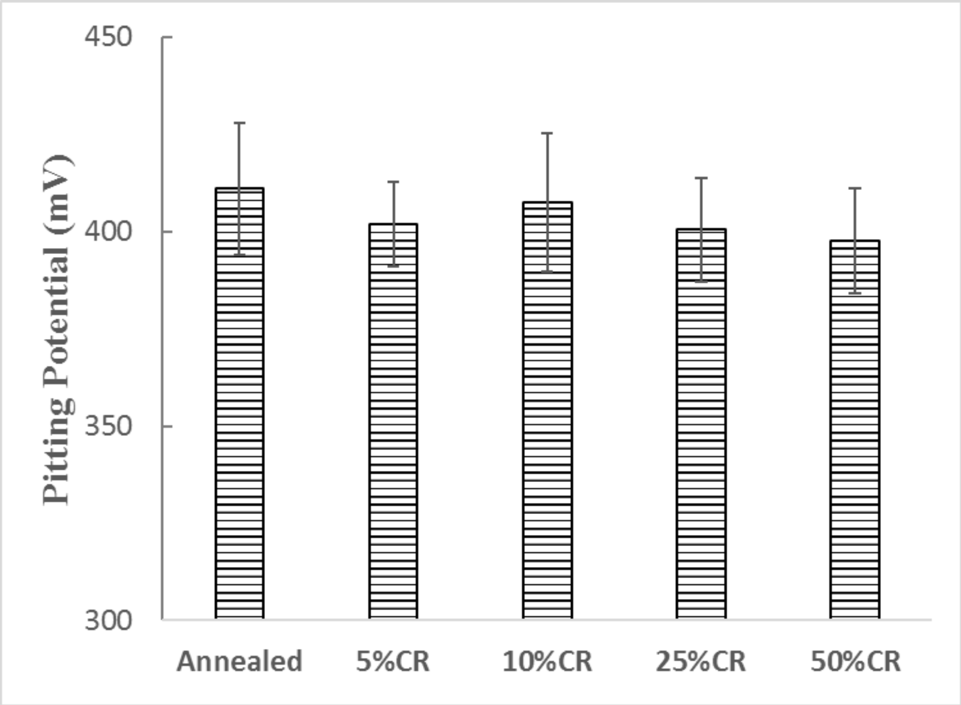

Figure 6-9. Average pitting potentials of SS 304 as a function of percentage cold-rolling in 0.1 M NaCl solution at 50 ^{o}C.

Even though there was not a significant difference in pitting potentials of SS 304 specimens, it did not mean that the cold-rolling does not influence on the corrosion resistance of SS 304. Pit-repassivation depends more on the chemistry inside the pits rather than surface conditions. Cold-rolling could still have an impact on the pit-repassivation process, since a pit volume can easily surpass the near-surface microstructure influenced by mechanical polishing. To investigate the effect of cold-rolling on pit-repassivation, a set of pit-repassivation tests were performed on re-polished SS 304 specimens at the five cold-rolling levels in 0.1 M NaCl at 50 ^{o}C. As a pit was initiated at +300 mV$_{(SCE)}$, the potential was immediately dropped to +250 mV$_{(SCE)}$ to repassivate the pit. As discussed in the previous chapter that such pits initiated on different samples possessed a similar geometry. This guaranteed the following pit-repassivation step was set up in the same starting line. The corresponding repassivation currents for SS 304 specimens at five cold-rolling levels are demonstrated in Fig. 6-10. The current decay signifies a pit-repassivation process. The longer it took for the current to decay, the more difficult the repassivation was. It was clearly shown by the results that it took longer time for an initiated pit to repassivate as the degree of cold-rolling increased. This means it was more difficult for heavily cold-rolled specimens to repassivate a pit at +250 mV$_{(SCE)}$.

To demonstrate the reproducibility, three tests were done under similar conditions for each cold-rolling level and presented in Fig. 6-11. From Fig. 6-11 a-e, the trend of increasing size of repassivation loop, which indicates higher pit growth, stayed consistent as the percentage of cold-rolling increased. It can be seen in Fig. 6-11 (e) that the repassivation time was only ~0.5 second when the maximum level of cold-rolling was applied. Although repassivation times are very short, but the results were reproducible and indicate that pit-repassivation was hindered by the residual cold-rolling strain. This may also explain why there was not a significant difference in the cyclic-polarization behavior of SS 304 at different cold-rolling levels.

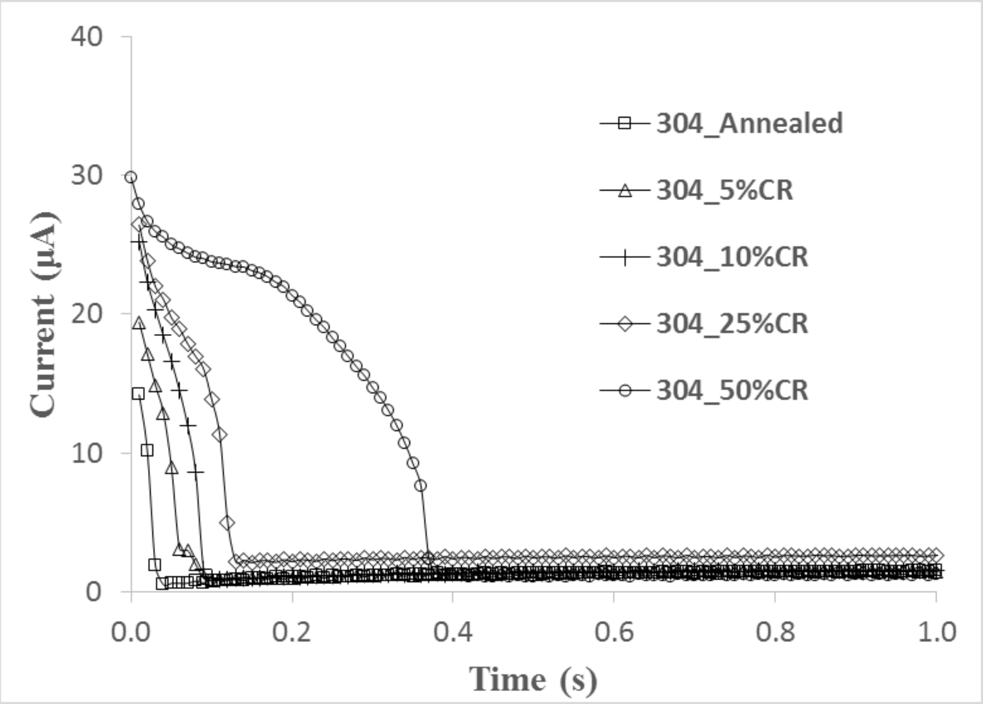

Figure 6-10. Pit-repassivation behavior at +250 mV$_{(SCE)}$ for SS 304 specimens as received, 5% CR, 10% CR, 25% CR, and 50% CR specimens in 0.1 M NaCl solution at 50 ^{o}C.

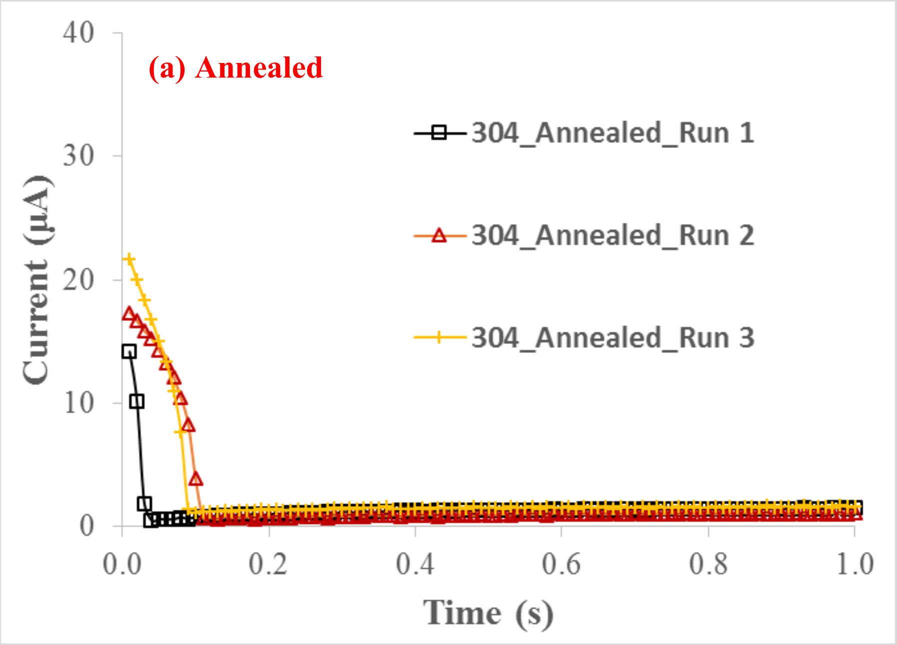
(a) Annealed
304_Annealed_Run 1
304_Annealed_Run 2
304_Annealed_Run 3
Current (μA)
40
30
20
10
0
Time (s)
0.0
0.2
0.4
0.6
0.8
1.0

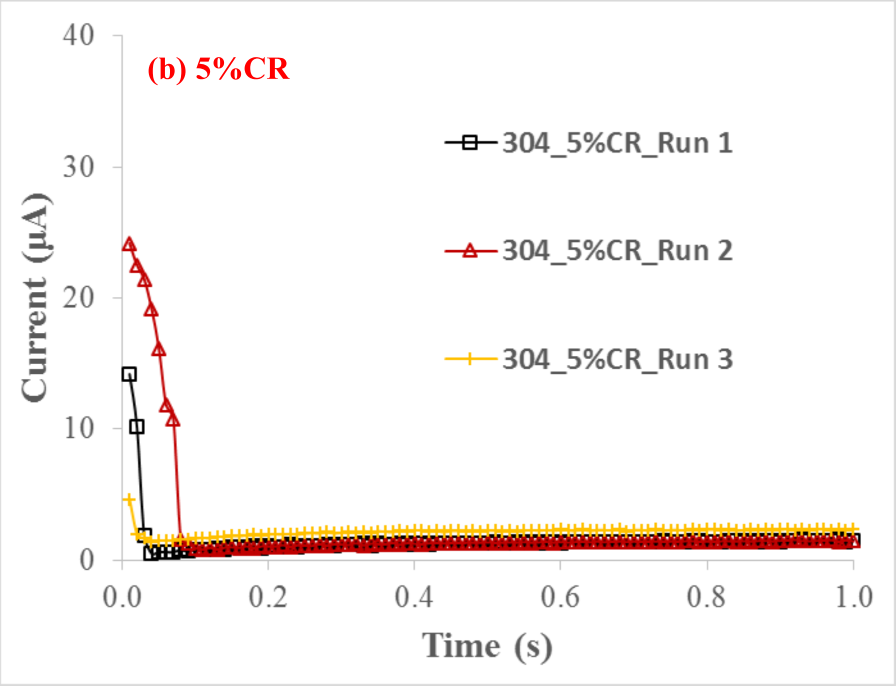
(b) 5%CR
304_5%CR_Run 1
304_5%CR_Run 2
304_5%CR_Run 3
Current (μA)
Time (s)
0
10
20
30
40
0.0
0.2
0.4
0.6
0.8
1.0

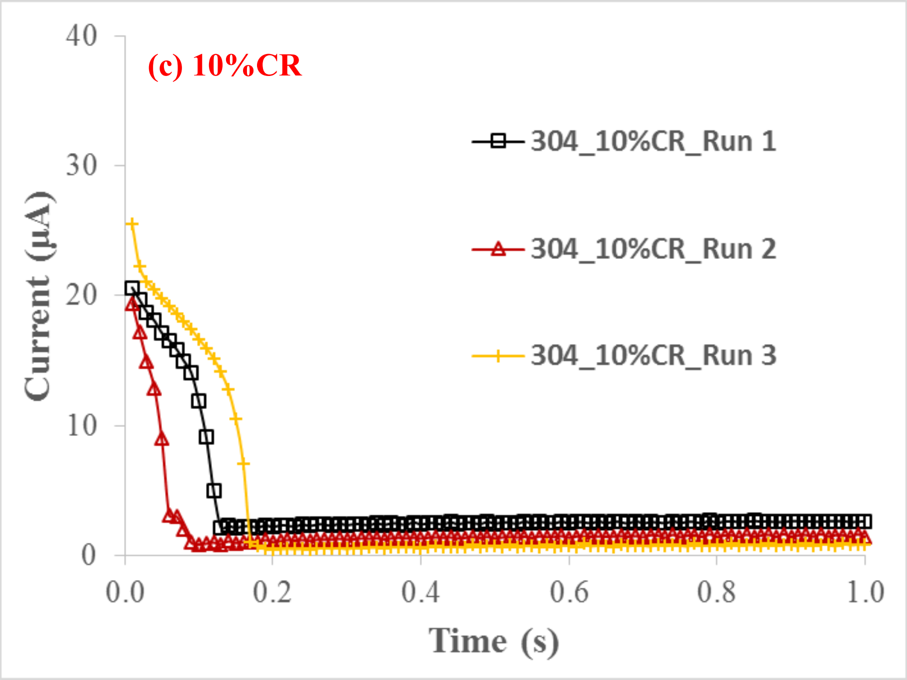
(c) 10%CR
304_10%CR_Run 1
304_10%CR_Run 2
304_10%CR_Run 3
Current (μA)
Time (s)
0
10
20
30
40
0.0
0.2
0.4
0.6
0.8
1.0

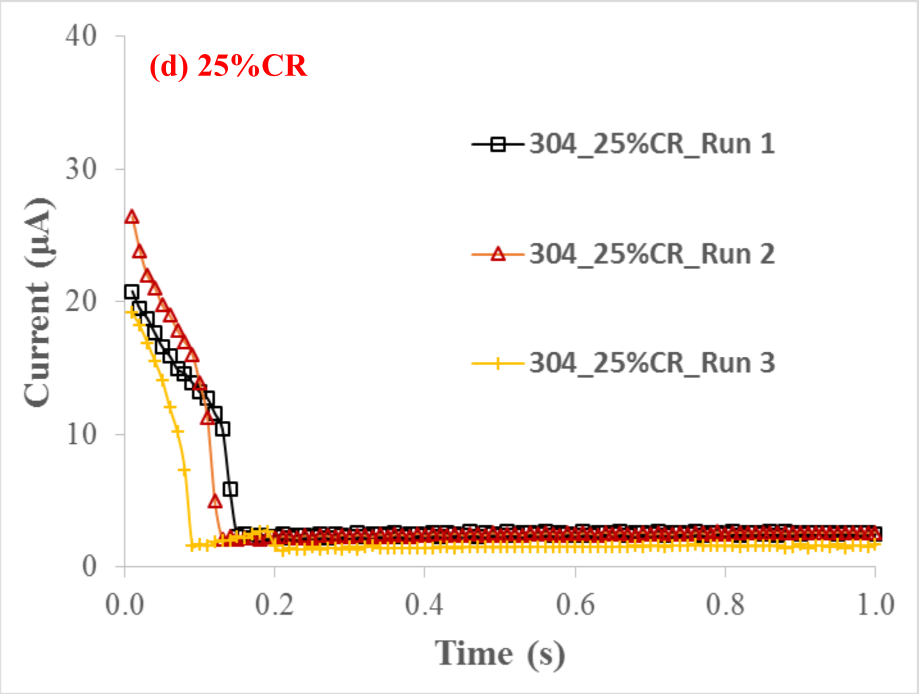

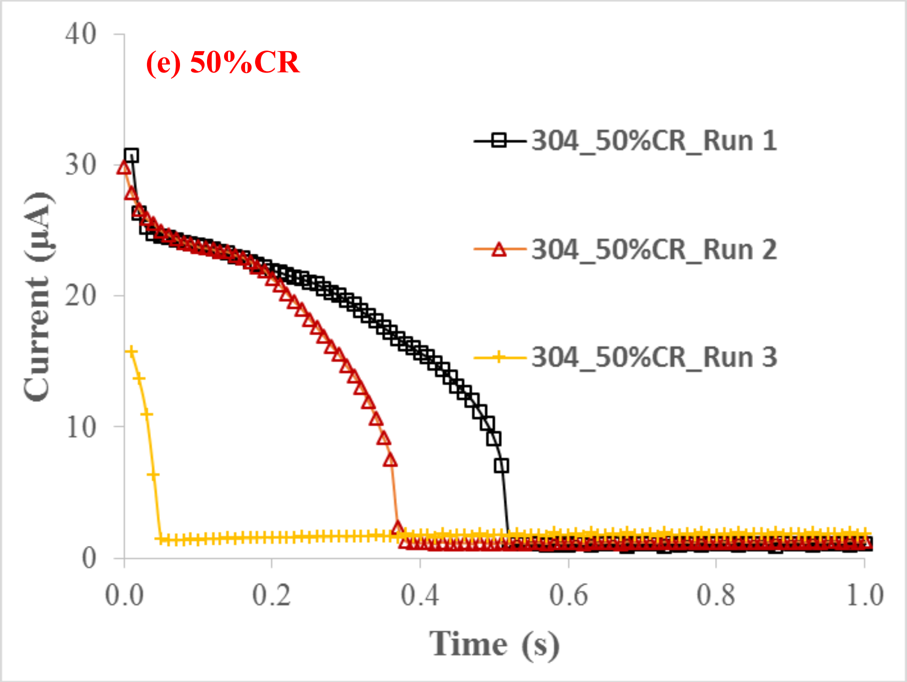

Figure 6-11. Three repetitions of pit-repassivation tests of SS 304 at +250 mV$_{(SCE)}$ for five different cold-rolling levels: (a) annealed (0%CR), (b) 5%CR, (c) 10%CR, (d) 25%CR and (e) 50%CR.

To amplify the effect of cold-rolling on the pit-repassivation process, a set of pit-repassivation tests were done at an elevated potential of +280 $mV_{(SCE)}$, and the results are shown in Fig. 6-12. At +280 $mV_{(SCE)}$, all tested samples of SS 304, strained to different values, took longer time to repassivate a pit as compared to an equivalent test done at +250 $mV_{(SCE)}$. However, the pit on the samples with50% CR failed to repassivate and continued to grow instead and became a stable pit. These results clearly indicated that strain introduced by cold-rolling hindered the pit-repassivation process. To demonstrate the reproducibility of this set of tests, three tests were done at each cold-rolling level and presented in Fig. 6-13. Reasonable deviations of the pit-repassivation behavior was seen, but the above-mentioned trend in Fig. 6-12 was confirmed.

Comparing the pit-repassivation activities at +250 $mV_{(SCE)}$ and the ones at +280 $mV_{(SCE)}$, it was found that a high degree of cold-rolling impeded repassivation of SS 304, and this hindered repassivation behavior can transit a metastable pit to a stable pit for the 50%CR specimen at + 280 $mV_{(SCE)}$. It was argued in the previous chapter that strain acts as an additional driving force and stabilizes pit growth by a quick dissolution mechanism which ensures the stability of the salt film within the pit. The same argument can apply here, a high level of cold-rolling leads to a higher internal strain energy which drives a stronger dissolution during repassivation. This made the pit-environment more aggressive, since the hydrolysis driven by a stronger dissolution reaction can result in a lower pH and a higher concentration of Cl^-. Situations may be further complicated when elastic tensile stresses are applied, because the tensile stresses can concentrate stresses at the pit walls, disrupting passive layer and repassivation. This may accelerate the dissolution inside a pit even further.

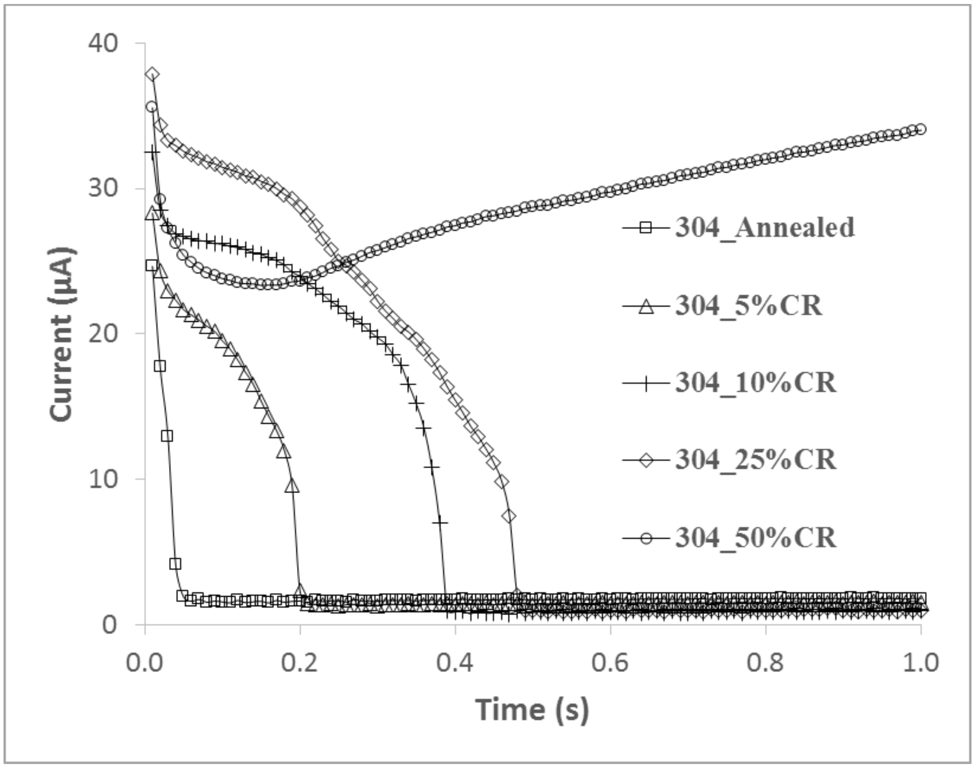

Figure 6-12. Pit-repassivation behavior at +280 mV$_{(SCE)}$ for SS 304 Specimens as received, 5% CR, 10% CR, 25% CR, and 50% CR specimens in 0.1 M NaCl solution at 50 ^{o}C.

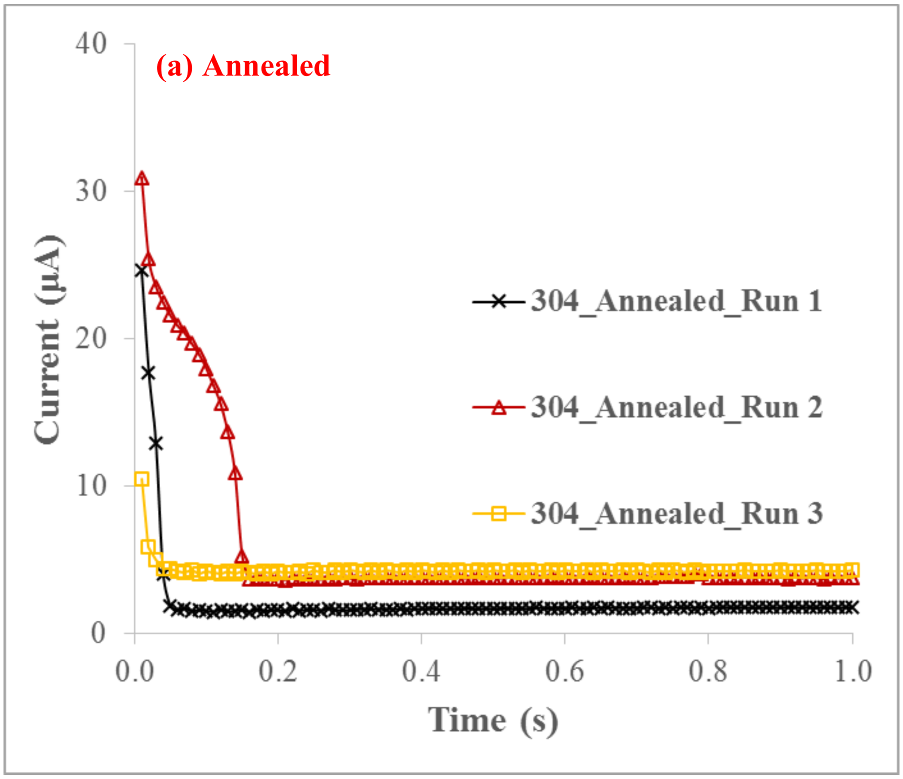
(a) Annealed
Current (μA)
40
30
20
10
0
0.0
0.2
0.4
0.6
0.8
1.0
Time (s)
304_Annealed_Run 1
304_Annealed_Run 2
304_Annealed_Run 3

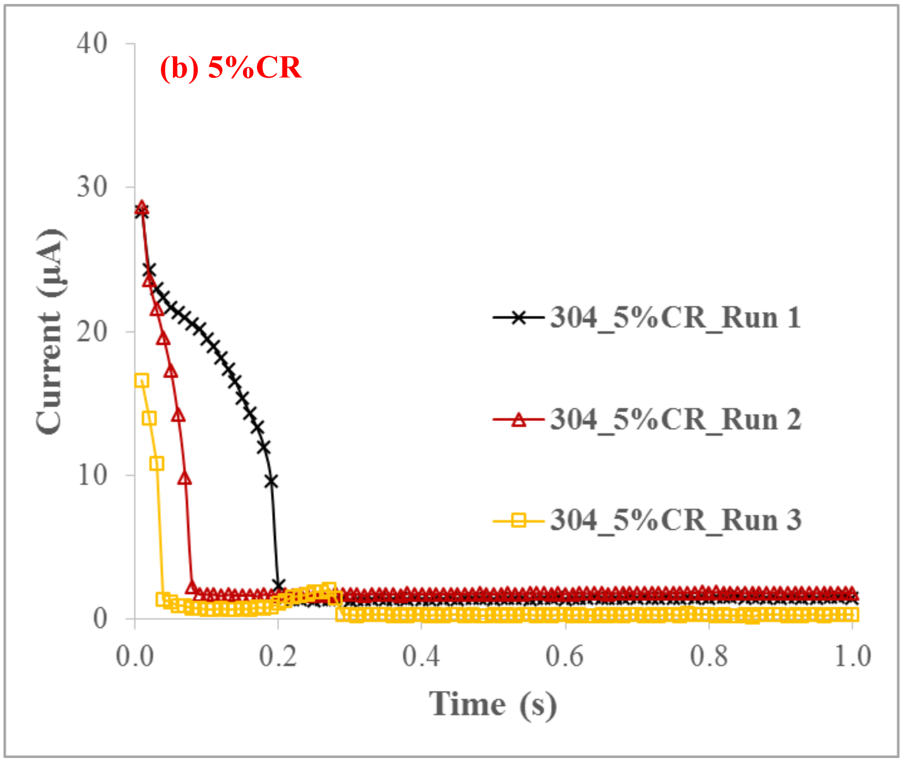
(b) 5%CR
Current (μA)
40
30
20
10
0
0.0
0.2
0.4
0.6
0.8
1.0
Time (s)
304_5%CR_Run 1
304_5%CR_Run 2
304_5%CR_Run 3

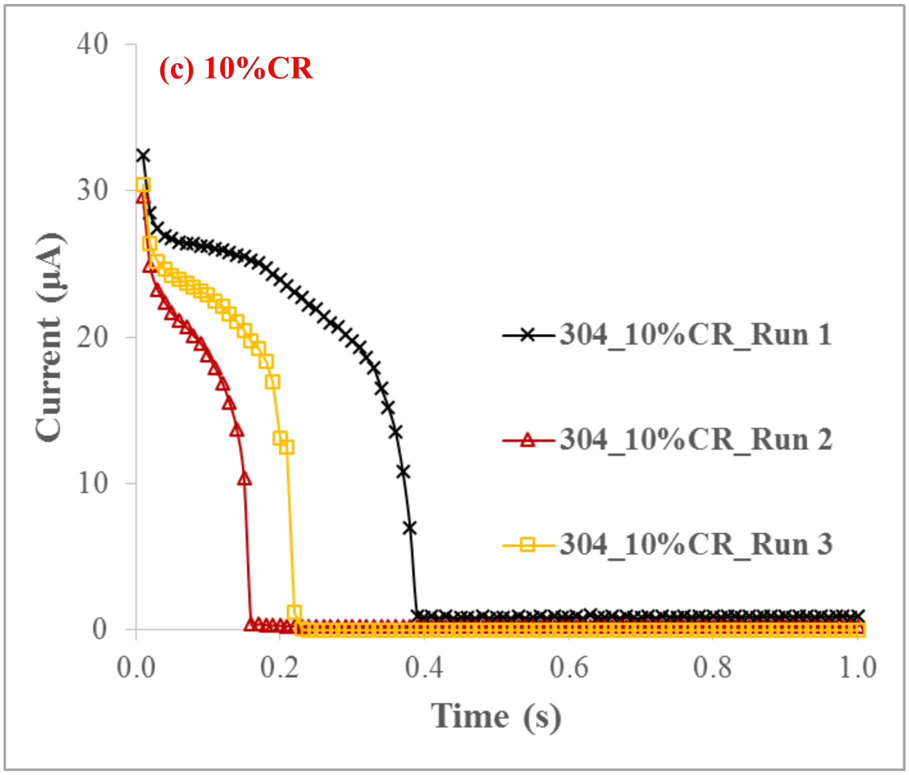
(c) 10%CR
40
30
20
10
0
Current (µA)
0.0
0.2
0.4
0.6
0.8
1.0
Time (s)
304_10%CR_Run 1
304_10%CR_Run 2
304_10%CR_Run 3

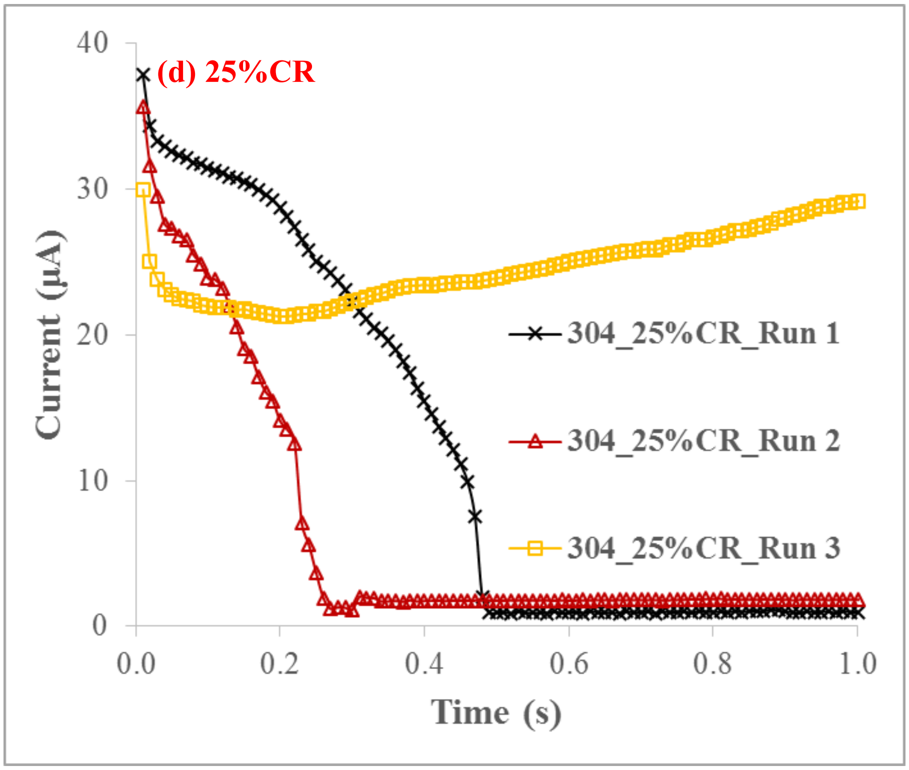
(d) 25%CR
40
30
20
10
0
Current (µA)
0.0
0.2
0.4
0.6
0.8
1.0
Time (s)
304_25%CR_Run 1
304_25%CR_Run 2
304_25%CR_Run 3

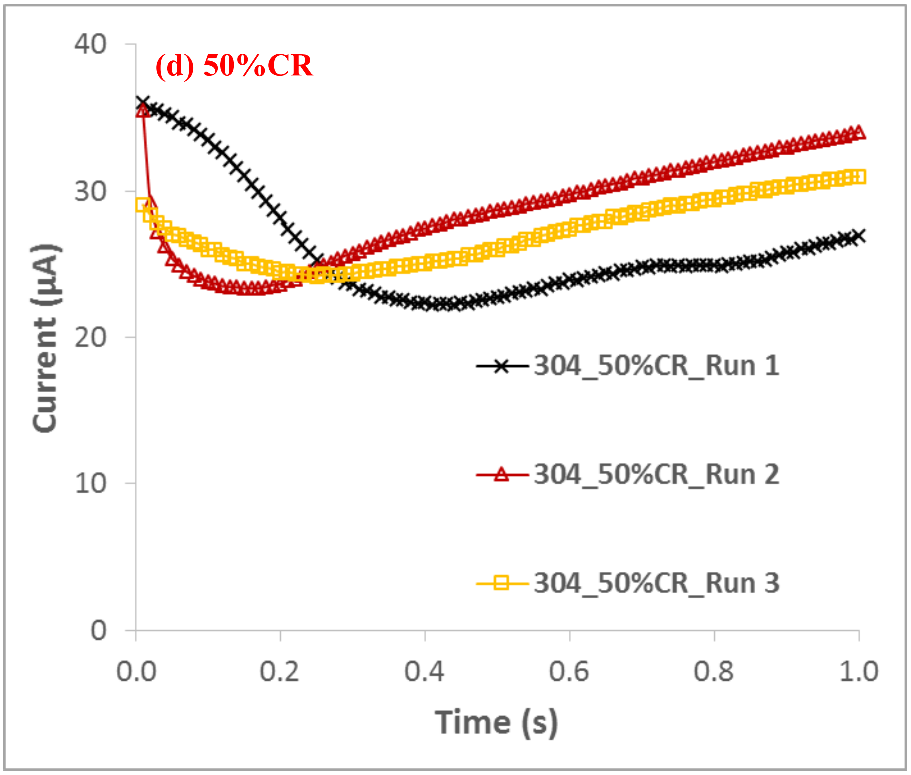

Figure 6-13. Three repetitions of pit-repassivation tests of SS 304 at +280 mV$_{(SCE)}$ for five different cold-rolling levels: (a) annealed (0%CR), (b) 5%CR, (c) 10%CR, (d) 25%CR and (e) 50%CR.

6.4 Similarities and Differences: Effects of Plastic Deformation and Effect of Elastic Stresses

For SS 304 samples elastically loaded at 155 MPa, the pit-repassivation started to fail and transited to a stable pit at +250 mV$_{(SCE)}$. However, the effect of cold-rolling, plastic strain, on pit-repassivation behavior was relatively minor at +250 mV$_{(SCE)}$. No pre-initiated and repassiavted pit became a stable pit in all tested cold-rolled specimens at +250 mV$_{(SCE)}$, and the time period required to repasssivate each pit was also small, all less than 0.4 - 0.5 second. Yet, repassivation under elastic stresses seemed to be impeded to a much larger extent at +250 mV$_{(SCE)}$. The repassivation time for the SS 304 speicimens ranged from ~0.2 second to 1.5 seconds in the stress range from 0 MPa to +103 MPa, while the stable pits started to grow and the repassivation failed at +155 MPa.

To directly compare the repassivation behavoior under elastic conditions and cold-rolling conditions, two repassivation curves at +250 $mV_{(SCE)}$, namely at an elastic stress level of 52 MPa and at 50% CR level were plotted in Fig. 6-14. Based on the residual stress measurements, SS 304 at 50%CR level possessed roughly +150 MPa [3] compressive stress. However, the repassivation kinetics was faster for SS 304 specimen at 50%CR compared to the specimen at the elastic stress of 52 MPa. This indicates that the effect of elastic stresses was greatly magnified through some mechanism. It was discussed that unidirectional elastic tensile stresses acting on a pit-geometry can create a complex stress field which may comprise of magnified tensile stresses, compressive and shear stresses in the pit-vicinity. On the other hand, the initiated pit on a cold-rolled sample possesses a geometry of an occluded cavity, which can relax the stress field in the vicinity of the pit. Hence, it was reasonable that such a stress field alleviated the effect of stress on the pit growth. That may distinguish between the synergistic effects of elastic tensile stresses on pit stability and growth from the plastic residual strain effect on a cold-rolled sample.

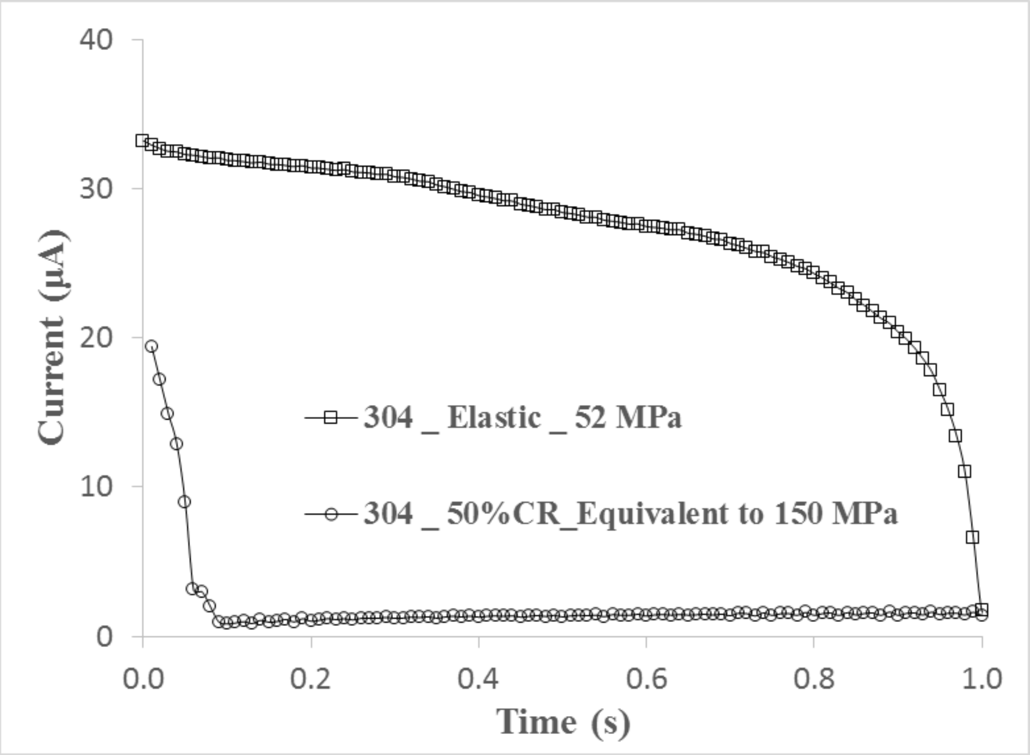

Figure 6-14. Pit-repassivation behavior at +250 mV$_{(SCE)}$ for SS 304 specimens at 52 MPa and at 50%CR level in 0.1 M NaCl solution at 50 ^{o}C.

All things considered, plastic deformation introduces surface defects and residual strain in form of structural defects in the materials. Since pitting corrosion is extremely sensitive to surface conditions of metals, it makes sense that surface defects appeared to be more prone to pitting attack. From the perspective of the driving force of a corrosion reaction, surface defects are localized high-energy concentrated areas. As a result, it is more likely for pits to grow rapidly in such localized surface areas. On the other hand, residual stresses can be greatly relaxed in the pit vicinity, so it did not decrease the pitting resistance of SS 304 significantly over the parameters investigated in this study. Re-polishing separated surface defects from residual strain in the materials, so it greatly recovered the pitting resistance of SS 304. Possible mitigation strategies can be inspired based on the results from this study, as described in the chapter 8.

6.5 Conclusions

The presence of strain, both elastic and plastic influence pitting resistance of SS 304 in the chloride-containing environment. Following conclusions can be drawn from these results:

- The negative effect of elastic stresses on cyclic polarization behavior of SS 304 reached a limit at the yield stress. Extending the strain into the plastic range did not further deteriorate the pitting resistance.
- SS 304 experienced different degrees of recovery in the pitting resistance as the applied plastic stress was unloaded until a certain amount of surface defects were accumulated at a high strain level.
- Surface defects were believed to cause the primary damage to pitting corrosion of SS 304.
- Plastic deformation in SS 304 induced martensitic transformation. The presence of martensite did not appear to alter the pitting resistance of SS 304 significantly over the test conditions investigated in this study.
- Pit-repassivation was hindered by the residual strain, but the effect was smaller than that for applied elastic stresses.
- Repolishing a plastically strained stainless steel can be used to minimize the negative effect of the residual plastic strain on its pitting susceptibility. However, this effect can still be revealed during the pit-repassivation process under proper conditions.

CHAPTER 7. EFFECT OF STRAIN ON REPASSIVATION

When metallic materials are in passivated state, the presence of the passive film provides a protective layer on the metal surface, passivating metals from corrosion. Localized breakdown of the passive films leads to localized corrosion like pitting corrosion. Therefore, we refer to the state where metallic materials can undergo localized corrosion as the unstable passivity. In present study, we have examined the effect of strain on pitting corrosion of stainless steel 304 in Chapter 5&6 and discussed the mechanism of the strain-assisted pitting phenomena. In contrast to the unstable passivity, metallic materials can passivate under a stable passivity condition. In such a situation, materials bear no risk of localized corrosion under corresponding environmental conditions. The only chance that the passive film can be damaged is from external impacts. For example, when hard particles are impinging on or grinding the metal surface, and the resultant physical impact ruptures the passive film on the metal surfaces. This happens often in chemical processes which flow in turbulent regime and carry hard media with a significant speed.

It becomes interesting to investigate the effect of strain on repassivation kinetics under the stable passivity condition. Traditionally, a scratch test is used to physically rupture the passive film. However, this technique cannot be applied here, since a physical scratch imparts additional strain into the metal surface. Mechanical staining the specimens into the plastic deformation range was also employed to study film rupture and its associated repassivation kinetics [84, 86, 88]. However, there are some interferences associated with mechanical straining, such as film thinning and potential crack initiations. In addition, the film rupture during plastic deformation was found to be extremely stochastic demonstrated in Fig. 5-2. It is not possible to have a precise control on the size and length of the rupture film by mechanical straining of the entire sample.

In this chapter, we used an electrochemical method to remove the native passive film on the surface, without introduction of additional mechanical strain at the surface, and perform the repassivation tests for differently strained steel samples.

7.1 Effect of Strain on Polarization Behavior of Carbon Steel in a Neutral Environment

To gain a fundamental knowledge of the polarization behavior of carbon steel A569 in a neutral environment, a set of potentiodynamic polarization tests was performed in a borate buffer solution containing 0.3 M boric acid and 0.075 M sodium tetraborate at room temperature. To avoid the interference of the native oxide film formed in the air, all the surfaces were re-polished and reduced at -1000 $mV_{(SCE)}$ for 3 hours in the same borate buffer solution before the potentiodynamic test. Fig. 1 showed polarization behavior of five differently cold-rolled specimens in the borate buffer solution. All five specimens showed passive region starting at roughly -300 $mV_{(SCE)}$, and the passive film on these samples broke down and the samples entered the transpassive region at roughly +900 $mV_{(SCE)}$. These results indicate that an increase in strain in these tests did not affect the passivation behavior of A569. The slight variation in passive current densities among these specimens was not consistent and did not show any trend. This indicated that the residual strain due to cold-rolling does not exhibit any effect on the polarization behavior of carbon steel in the borate buffer solution used in this study. The passive region of A569 in the borate buffer solution was clearly demonstrated in Fig. 7-1, roughly ranging from -500 $mV_{(SCE)}$ to +900 $mV_{(SCE)}$, so a potential within this range, +150 $mV_{(SCE)}$ was selected to performed stable-repassivation tests in the following experiment.

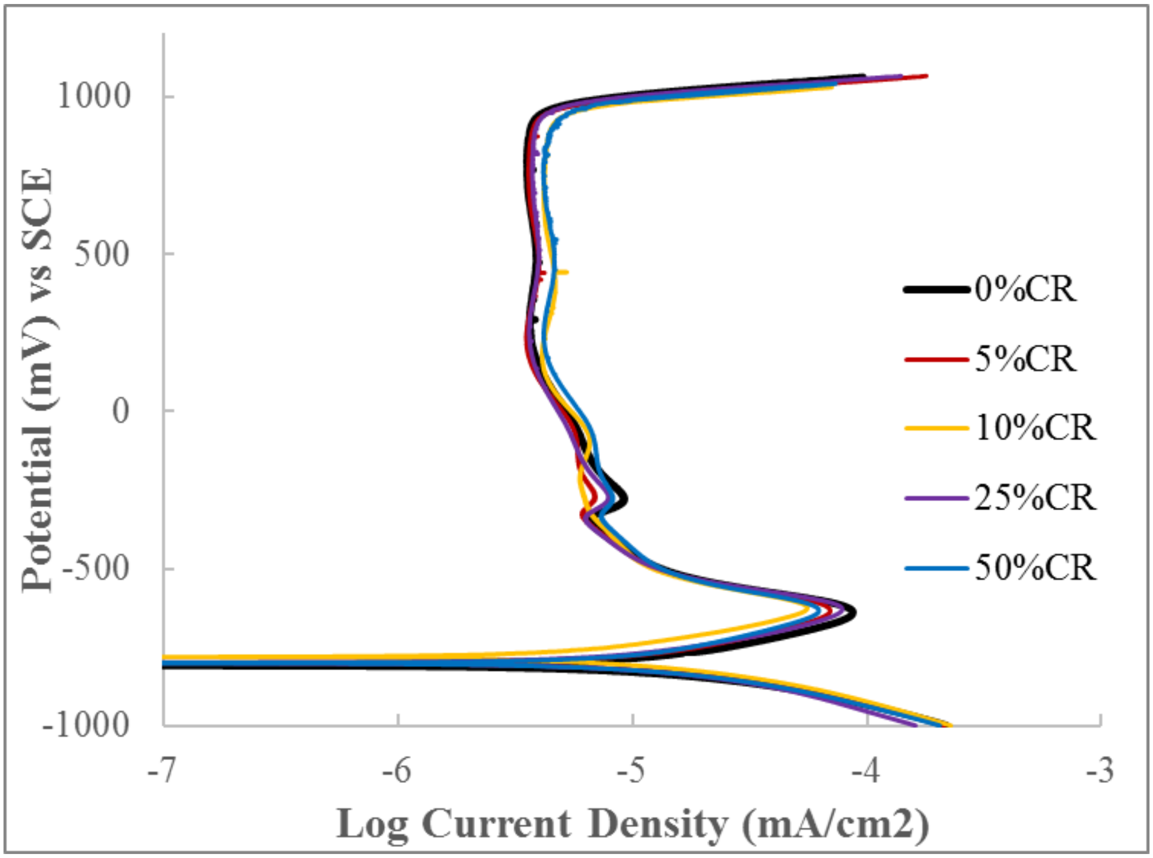

Figure 7-1. Polarization curves of 0% CR, 5% CR, 10% CR, 25% CR, and 50% CR specimens in borate buffer solution.

7.2 Effect of strain on stable repassivation of carbon steels

To study the repassivation behavior of carbon steels, chronoamperometry tests were performed in the boric buffer solution (pH = 8.4) at a potential at +150 $mV_{(SCE)}$ after reducing the sample surfaces at -1000 $mV_{(SCE)}$ to remove the native oxide film. Application of +150 $mV_{(SCE)}$ potential allowed the reduced metal surfaces to reform an oxide film on their surface. The repassivation currents were monitored as shown in Fig. 4. During potentiostatic repassivation the current densities at +150 $mV_{(SCE)}$ applied potential decayed with time very rapidly for the cold-rolled specimens, as shown in Fig. 2. The passive film was almost completely formed within the initial 1.2 seconds, indicated by the converging current density at the end of each curve. Faster repassivation kinetics, represented by the faster decay in current density, was noticed for the specimens with higher degrees of cold-rolling. Each of these repassivation tests was repeated at least five times and the results were consistent.

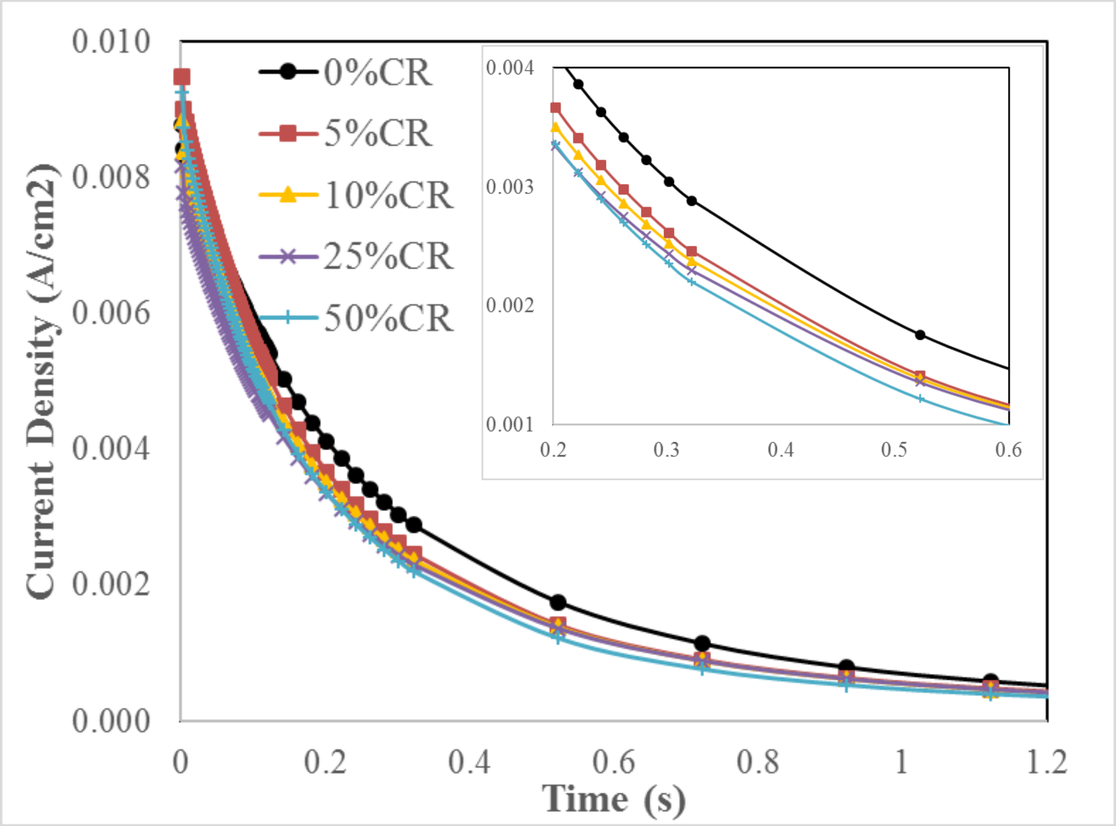

Figure 7-2. Repassivation Current Density at +0.15$V_{(SCE)}$ for 0%CR, 5%, 10%CR, 25%CR and 50%CR specimens in borate buffer solution.

To simulate the repassivation behavior, Ratzer–Sheibe and Buhl employed two terms to simulate the repassivation current [149]. This model treated repassivation as a film-thickening process. The first term represents the dissolution current, and it can be used to model monolayer growth at the early repassivation stage

$$I_{mono} = cvQ_{ox}(1-\theta) \qquad \text{7-1,}$$

where v is the scratch speed, Q_{ox} is the charge density to form a monolayer of oxide, and c is a constant. The second term reflects the thickening of the film by the addition of another monolayer

$$I_{film} = \theta A t^{-b} \qquad \text{7-2,}$$

where θ is a "covering coefficient" and A and b are empirical constants.

Similar to Beck's and Ratzer–Sheibe's models, Lillard's model was developed by Lillard, Vasquez, and Bahr [144], which splits the repassivation current I_{total} into the dissolution current I_{diss} and the film passive current I_{film}, as is given by Eq. 8:

$$I_{total} = I_{diss} + I_{film} = (1-\theta)\cdot I_{bare} + \theta \cdot A \cdot t^{-b} \qquad \text{7-3,}$$

where I_{bare} is the very initial dissolution current from the bare metal, roughly taken as the first current recorded; θ is the fraction of area covered by the passive film and is expressed by

$$\theta = 1 - \exp(-k \cdot t^{-n}) \qquad \text{7-4,}$$

where A, b, and n are constants that need to be computed accordingly.

A MATLAB code (MathWorks, Inc., Natick, MA) was written to fit the repassivation current data, and hence fraction of completion Θ vs time plot could be derived. Above 99.5% fitting was obtained for each curve. A representation of data fitting is demonstrated in Fig. 3 using an annealed

A569 specimen. Fraction of repassivation completion ϴ was extracted from the mathematical simulation and the ϴ is plotted with respect to time in Fig. 7-4. The resultant data in Fig. 4 indicates that the repassivation kinetics is accelerated due to the presence of strain, as shown in Fig. 4. This is likely due to the accelerated active dissolution rate of the bare metal surface because of the additional residual strain energy in the material. Several authors have demonstrated that strain increases metal active dissolution rate [13, 16]. Therefore, the higher dissolution rate at the early stable repassivation stage is very likely to provide more metal cations to accelerate the following oxide-film formation. These results indicated that the effect of strain was predominant before the large surface area is repassivated in the early stages of passive film formation. Stable repassivation only take place under environmental conditions where stable passivity is maintained, while unstable passivity is more often seen in industrial processes.

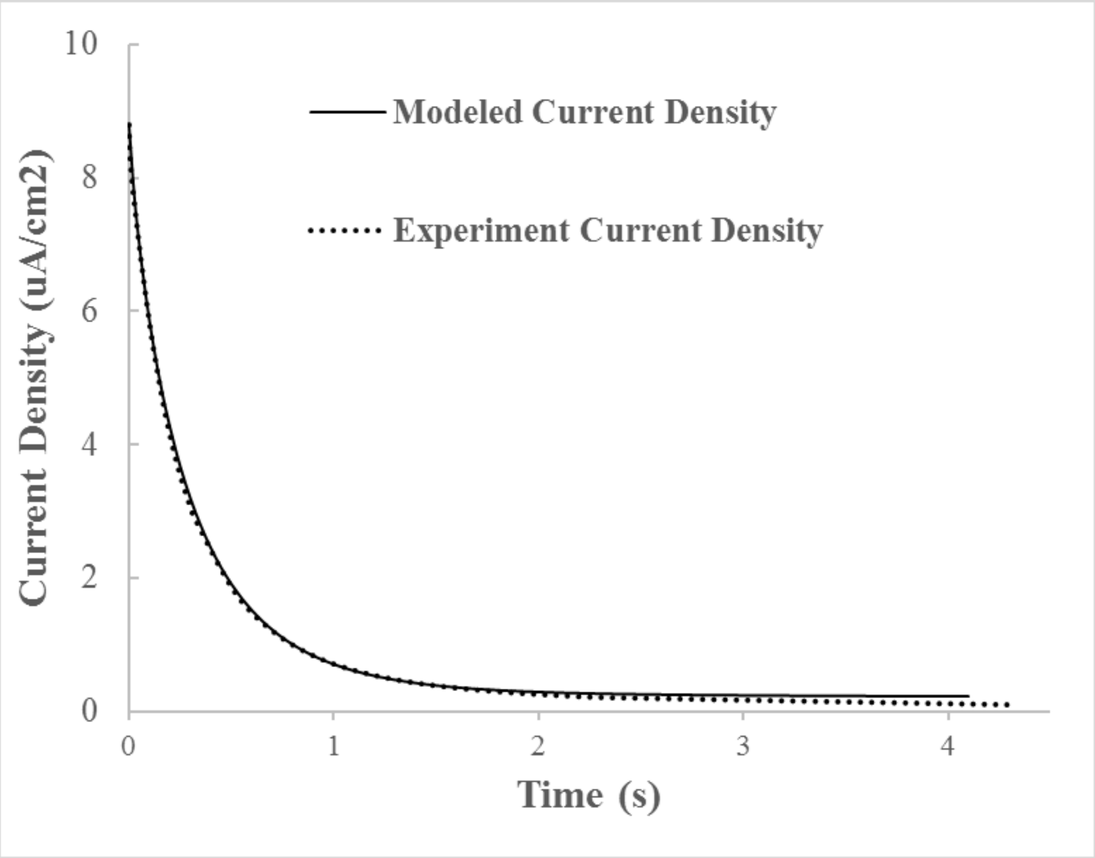

Figure 7-3. A comparison of the experimental current densities and the modeled current density using simulation during the repassivation process of an annealed A569 specimen.

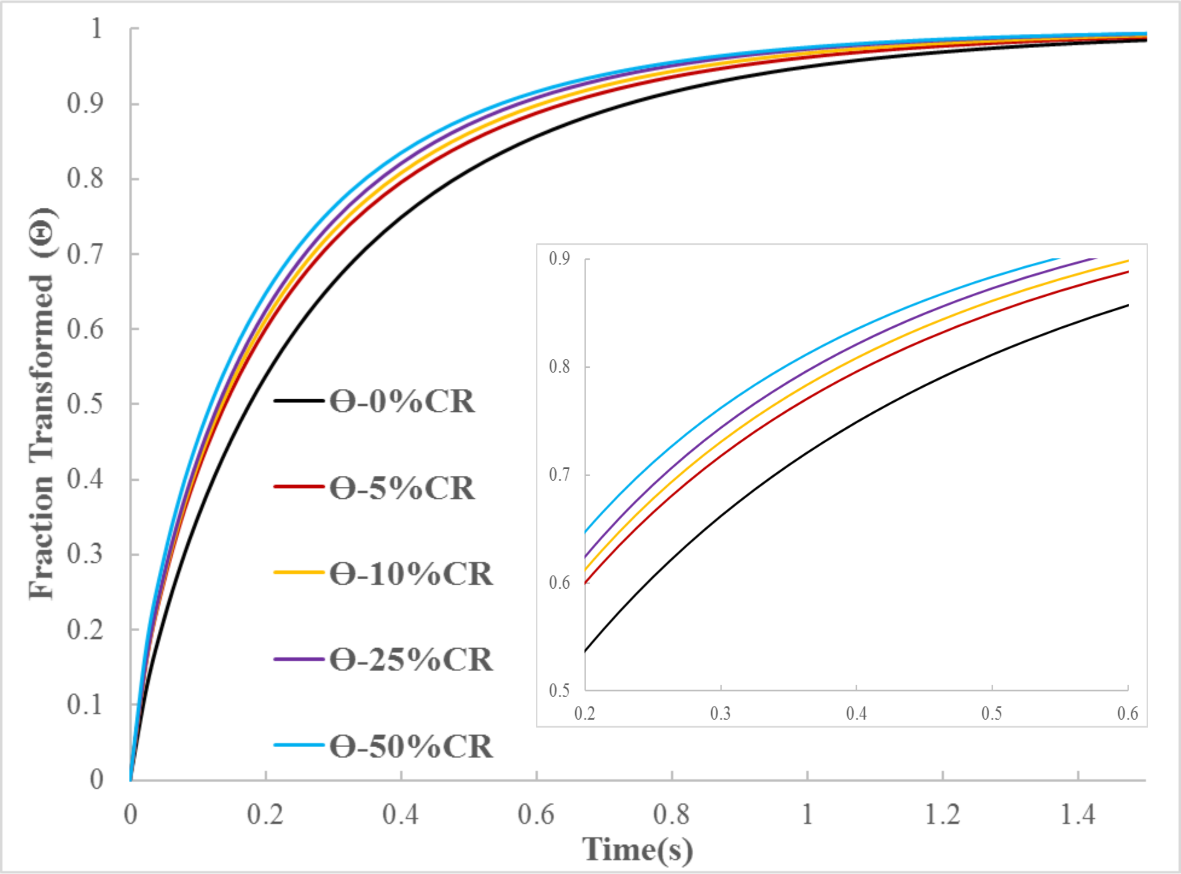

Figure 7-4. Fraction of Completion of Film Formation Θ as a function of time for 0%CR, 5%CR, 10%CR, 25%CR, and 50%CR specimens.

7.3 Conclusions

Under stable-passivation conditions, results indicate that the effect of strain does not affect the polarization behavior of carbon steels under passivating near-neutral pH conditions. However, strain due to cold-rolling under stable passivity facilitated the faster repassivation of exposed surface. This was likely because the strain accelerated the dissolution in the very early stage of repassivation. As a result, it improved the reaction kinetics of oxide-film formation.

CHAPTER 8. OVERALL SUMMARY AND RECOMMENDATIONS

8.1 Introduction

This chapter summarizes the effect of strain on the general corrosion, pitting corrosion, and stable-repassivation behavior of steels, as described in previous chapters. Strain applied in this study was either in the elastic range or in the plastic range using tensile deformation as well as cold-rolling. The resultant effect of strain on general corrosion kinetics, stable-repasssivation kinetics, and pit initiation and growth are discussed in unified manner.

8.2 Summary of Strain Effects on Different Types of Corrosion Behavior

The effect of strain on general corrosion of carbon steel A569 in an acidic environment was assessed qualitatively and quantitatively using different evaluation methods and different deformation techniques, as described in Chapter 4. An immersion test in a 3.75 M sulfuric acid solution at 50 ^{o}C was used to induce a very strong active dissolution on the metal surface, ensuring that the corrosion reaction was under activation control throughout the whole immersion test. Tensile strain, both elastic and plastic resulted in an accelerated general corrosion rate and a lowered open circuit potential (OCP). This confirmed the hypothesis in Chapter 2 that strain can provide an additional driving force to facilitate the corrosion reaction under activation control. The elastic tensile strain applied to the materials caused a lattice expansion and stored strain due to crystalline defects like dislocations. The resultant strain energy increase could be recovered after the onset elastic strain was released. Therefore, the effect of elastic strain on general corrosion is reversible. Based on the results from the weight loss measurements, the applied elastic stress increased the general corrosion rate monotonically, and the maximum corrosion rate increase for A569 was ~14.4% at the yield stress. The relative corrosion rate was also derived using the OCP evolutions and the Butler-Volmer equation, by setting the corrosion rate of the unstrained specimen as the baseline. The results were comparable to the results from the weight loss measurements. This also indicated that the OCP measurement could be used to detect the effect of elastic strain on the corrosion behavior for an actively corroding material.

However, when extending the strain into the plastic tensile deformation range, irreversible microstructural changes or defects occur in form such as dislocations, dislocation pile-ups and formation of low-angle grain boundaries. These microstructural features are not reversible after the applied stress is released. Hence, the residual strain due to the prior plastic deformation led to a permanent increase on the general corrosion rate of CS A569. Residual strain was obtained after cold-rolling or the stress of prior plastic tensile deformation was released. The maximum plastic deformation level applied through tensile loading was 9% engineering strain, which caused a corrosion rate increase of ~10%. However, cold-rolling was used to apply up to 50% thickness reduction to A569 samples. It led to a monotonically increasing corrosion rate as a function of percentage cold-rolling where the 50% cold-rolling caused the general corrosion rate to increase by ~29.8%. It was noticed that general corrosion was not very sensitive to the surface finish of the materials at such a high corrosion rate average above 5000 mpys (equivalent to ~14.5 μms per hour) resulted from the immersion test in a 3.75 M sulfuric acid solution at 50 ^{o}C. The surface layer under these conditions should be quickly dissolved during the corrosion reaction.

Under environmental conditions where the metallic material is under passivation control, a passive film formed on the surface provides a physical barrier for general corrosion. Yet, localized breakdown of the passive film can lead to localized corrosion, for example pitting corrosion.

Simply applying the test condition in 0.1 M NaCl at 50 ^{o}C caused a significant ductility loss of SS 304 in a tensile test. The susceptibility of pitting resistance of stainless steel (SS) 304 was studied by four different levels of elastic tensile stresses. It was found that an increase in elastic stresses decreased the pitting potential of SS 304. This indicated that the elastic stresses degraded the pitting resistance of SS 304. A surface pre-treatment by immersing SS 304 specimens in a 2 M HNO_3 solution was used to develop a Cr_2O_3-rich passive film on the surface. As a result, the pitting potential of SS304 increased significantly for all SS 304 specimens at all stress levels applied. However, the negative effect of elastic stresses was still observed, meaning the stress effect on the pitting resistance of SS 304 was independent of surface chemistry or the composition of oxide formed at the surface. It was further discovered that metastable pitting was dominant, with a relatively larger sized metastable pits, when a lower stress level was applied. On the contrary, stable pitting was frequently observed when a higher stress level was applied along with a very small size and number of metastable pits. Through a set of pit-repassivation tests, it was found that elastic stresses deteriorated the pit repassivation behavior of 304 SS. Consequentially, it facilitated metastable pitting to transit into stable pitting.

The pitting resistance of SS 304 was also studied under in-situ plastic deformation on tensile samples. Two permeant changes occurred upon plastic deformation: surface defects (slip-lines on the surface) and residual strain due to microstructural changes, such as dislocations, twinnings and martensitic transformation. The pitting potential of SS 304 decreased to a plateau beyond the yield stress. The pitting potential started to recover after the stress was removed. When a lower value of the residual plastic strain is applied, the larger degree of the pitting resistance could be recovered upon unloading of tensile sample. This recovery of pitting resistance upon unloading ceased at ~9% residual plastic tensile strain. It was often observed that the localized areas concentrated with surface defects were more prone to pitting attacks. This indicated that accumulating a certain amount of surface defects eventually led to the maximum damage to the pitting resistance of SS 304. The effect of strain on pitting corrosion was also investigated by using cold-rolled SS 304 samples, where higher plastic strains could be applied. Results on cold-rolled samples did not show a clear trend of pitting potential evolution as a function of percentage cold-rolling. This was likely because all cold-rolled SS 304 specimens were re-polished before electrochemical measurements. Re-polishing removed the surface defects which were detrimental to pitting resistance and introduced a similar surface strain on all samples due to the grinding and polishing operation. This hypothesis was confirmed using a comparison test in which 9% plastically deformed tensile specimen was re-polished and it had a near 100% recovery in the pitting potential. Yet, strain due to cold-rolling even after re-polishing still retarded pit-repassivation, but to a very minor degree.

Pitting corrosion occurred when unstable passivity was exhibited in appropriate alloy/environment systems. However, when the passivity was stable, it was found that strain could facilitate the re-formation of the passive film in a slightly basic borate buffer environment. Simulation was done to quantitatively assess the stable repassivation kinetics.

8.3 Unified Understanding of the Strain-Assisted Pit Growth under Strain

A pit-growth model assisted by elastic strain was proposed in Chapter 5. The discussion on the strain-facilitated pitting phenomena was extended into the plastic strain range in Chapter 6. The missing connection and comparison are bridged here.

Firstly, the geometry of any pit is an occluded cavity into material surfaces. When in-situ stresses are applied, regardless of whether they are in the elastic range or in the plastic range, it can create a stress concentration zone in the vicinity of the pit. Of course, the stress concentration around a pit depends on the geometry of the pit and the nature of the stress applied. For example, a representative 2-D stress field of a circular hole under a remote uni-directional tensile stress of S_∞ is demonstrated in Fig. 8-1. The maximum stress concentration factor occurs along the horizontal direction next to the hole, which magnifies the applied stress, S_∞ by three times. The presence of this magnified stress field can greatly enhance the effect of stresses on the pit-growth process by stabilizing the formation of the salt film as discussed in Chapter 5. That explains why no further decrease of pitting resistance of SS 304 was observed upon increasing the in-situ strain into the plastic range. The elastic portion of the in-situ plastic strain did the primary damage to the pitting resistance of SS 304 by effectively participating in this stress concentration zone.

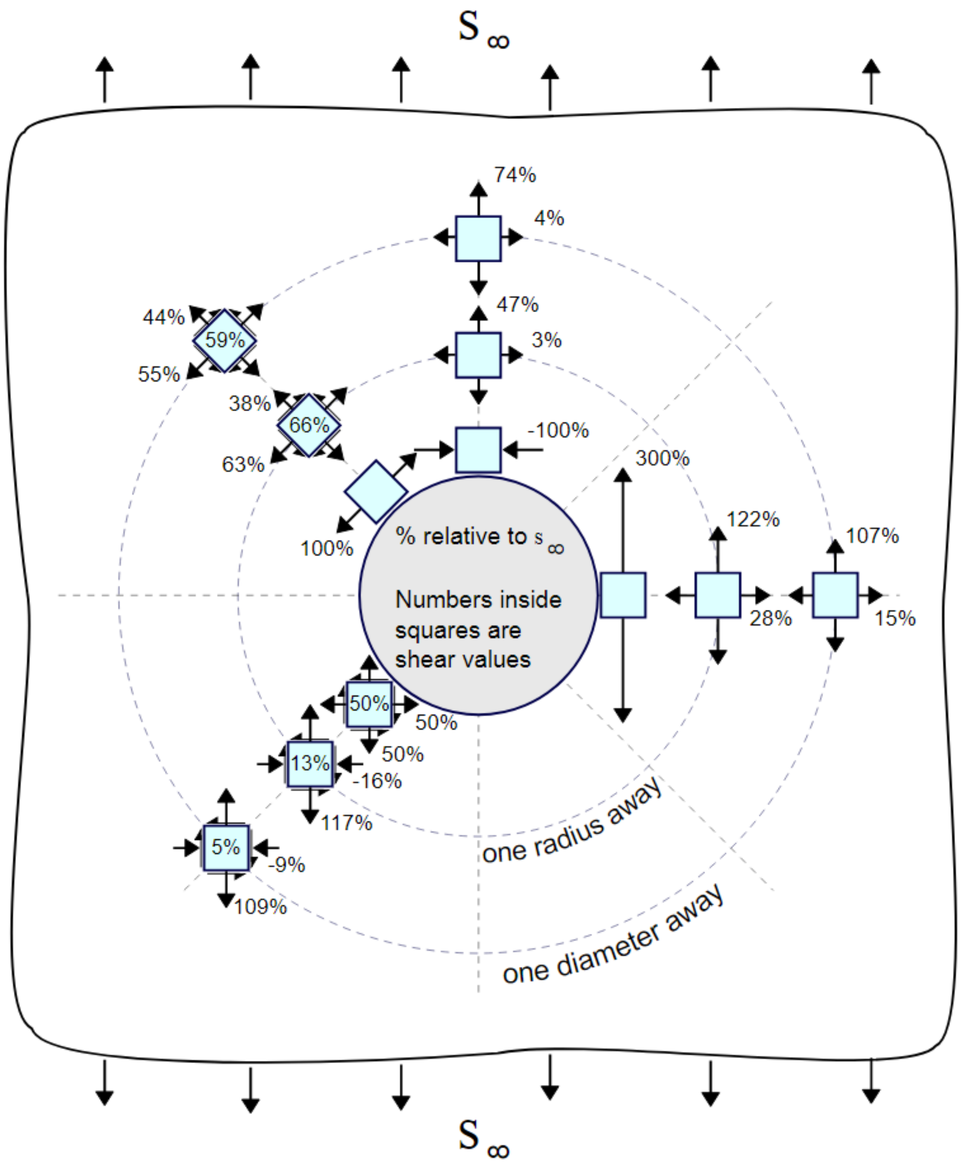

Figure 8-1. A 2-D stress field of a circular hole under a remote uni-directional tensile stress of S_∞ [150].

Residual strain due to prior plastic deformation introduces surface defects and residual strain into the materials. It was found that surface defects can be very prone to pitting attacks, likely because such localized high-energy concentrated features can provide a higher driving force for initiated pits to grow. It was found from the results of cyclic-polarization tests that the surface defects were more prone to pitting attack, as was also confirmed by the preferential pitting-attack observed under SEM, as described in Chapter 6. One may expect that the surface concentrated with surface defects may provide more vulnerable pitting-attack sites. Yet, cyclic-polarization tests only capture the first pitting event at its corresponding pitting potential. That is likely why we observed that accumulating a certain concentration of surface defects at a high residual strain level reached a maximum decrease of the pitting potential of SS 304. Repolishing was found to almost fully recover the pitting potential of SS 304, because the surface defects due to plastic straining were completely removed after repolishing.

The residual strain stored in the materials still facilitated pit growth. The pit-repassivation tests were utilized in Chapter 5 & 6 to monitor the growth of an initiated pit under strain. The pit was initiated until the current reached +40 μA. This can result into a pit depth around 10 μm as shown in Fig. 8-2. This indicated that the pit-repassivation test was performed at a microstructural depth significantly deeper than the surface. However, residual strain only facilitated pit growth to a very minor degree. This can be explained by the plane-stress elastic model [147] which expects no stress to exist perpendicular to the surface. A simplified 2-D plane-stress condition is demonstrated in Fig. 8-3, where the dash line indicates the disappeared stresses perpendicular to the surface and the solid line indicates the stresses on the tangent surface of the pit wall.

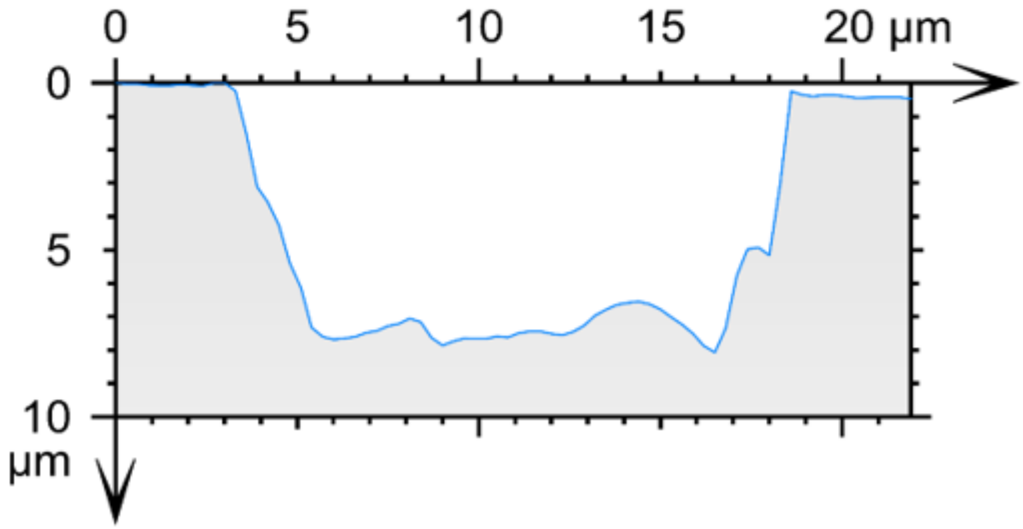

Figure 8-2. A 2-D cross-section of a pit initiated to +40 µA at +300 mV$_{(SCE)}$.

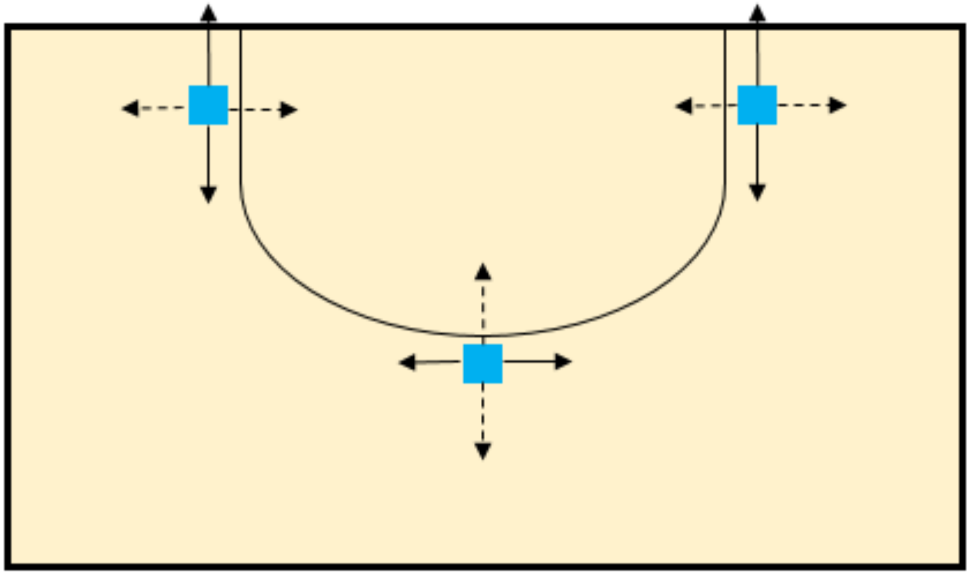

Figure 8-3. A simplified plane-stress stress field near a 2-D pit-geometry.

All things considered, a unified understanding can be summarized to explain the strain-assisted pit-growth process. When in-situ stresses are applied, the effect of stresses on pit growth is likely to be enhanced by the presence of stress concentration developed around the pit. The effect of strain can be greatly mitigated when a pit-geometry is developed as to relieve the stress field around the pit under residual strain. However, surface defects due to prior plastic deformation can provide preferential pitting attack sites.

8.4 Unified Understanding of Strain Effect on Corrosion Reactions

The governing principle of strain-influenced corrosion reaction is evidenced by the results from this study throughout the entire thesis. Strain is an additional source of energy, which increases the driving force for associated corrosion reactions. However, the kinetics of the reaction may vary from one corrosion state to another.

Under activation control, both elastic strain and plastic strain accelerate general corrosion. In the general corrosion process, the corrosion products typically dissolve into the exterior aqueous environment. No diffusion barrier is placed at the surface to limit the reaction to reach its full potential.

Under passivation control, general corrosion is inhibited by the presence of passive film. One special case studied in this thesis is the effect of strain on stable-repassivation of carbon steel A569. A stable passivity condition is implied in this case. This means that the passive film is stable, and no localized corrosion occurs. Strain energy could be utilized to accelerate the formation of the passive film on a bare metal surface, which is essentially another metal oxidation reaction. The products of this oxidation reaction form a stable passive film on the surface.

However, when the corrosion reaction is under unstable passivity, localized breakdown of the passive films leads to pitting corrosion. During pit growth, strain accelerates active dissolution inside the pit while the salt film is incomplete. This can happen during a repair process of the salt film or during a pit-repassivation process. As a result, strain stabilizes the salt film formation and retards the pit-repassivation. One can think of the effect of strain on the pit-growth process as general corrosion but regulated under different reaction mechanisms. The salt film is always under a dynamic process of partially dissolving into the environment and repairing from salts precipitated out from the pit solution. When the salt film regulates the diffusion process across the pit opening, the strain-enhanced active dissolution accelerates the salt film repair. When the salt film breaks down, the strain-enhanced active dissolution hinders pit-repassivation and promotes pit growth.

All corrosion reactions are associated with the electrochemical activities in the near-surface microstructure. Pitting corrosion is extremely sensitive to the as-manufactured surface conditions of materials, since a pit must initiate at the surface and penetrate at a localized site, instead of uniformly corroding the entire surface. That is why the surface defects appear to be extremely prone to pitting corrosion. On the other hand, general corrosion can rapidly corrode the microstructure preserved in the as-manufactured surfaces. As a result, the corrosion tendency possessed by the entire material is most important for the general corrosion.

8.5 Suggested Mitigating Strategies for Strain-Related Corrosion Failures

The results discussed in this thesis show many negative effects of strain on corrosion reactions under different reaction mechanisms. One way to eliminate these negative effects thoroughly is to remove the strain. Elastic stresses can be avoided by refining an engineering design so that the metallic components are exposed to lower stresses during service. Residual strain can be released by annealing the strained material at an appropriate temperature to relieve internal residual stresses. However, elastic stresses during the service life and residual plastic strain resulted from the manufacturing processes are sometimes inevitable. For example, cold-rolling or strain-hardening is often used to increase the strength of an alloy. Annealing releases residual strain at the cost of sacrificing the strength of the materials. This type of trade-off needs to be carefully considered before applying any mitigating strategies for the strain-related corrosion failures.

From results in chapter 5, we found that the elastic stresses degraded the pitting resistance of SS 304 by hindering the pit-repassivation process. Hence, it is recommended to use alloys with a higher repassivation capability, for example, stainless steels with a higher content of Mo or N. It was discussed at various places in this thesis that re-polishing can help to recover the pitting resistance of SS 304 greatly, because it helps to remove surface defects which are prone to pitting attacks. In other words, any technique that helps to remove surface defects can potentially improve the pitting resistance of stainless steels in an as-deformed condition. For example, electropolishing can be a good candidate to be utilized as potential final surface-finishing treatments.

There are also many corrosion prevention techniques, such as applying corrosion inhibitors and cathodic protection. These are beyond the scope of this thesis, so they are not particularly addressed.

8.6 Recommendations for Future Work along the Strain Theme

Both tensile deformation and cold-rolling were employed in this thesis as two important deformation techniques to apply strain/deformation to steels. Other deformation techniques, such as bending, shot peening, or compressive stresses can be explored to study the associated effects on different types of corrosion. For example, the stress field around a similar pit-geometry can be different under bending than under uni-directional tension. Hence, the resultant effect on pit-growth could also be different.

The effect of strain on general corrosion was theorized assuming that strain imparts no influence on the reduction or cathodic reaction on strained metal surfaces. Much related work has demonstrated the possibilities that strain can enhance or hinder the affiliated catalytic reactions according to different types of strain [30-32]. Hence, the acceleration of general corrosion due to strain may be caused by the synergy of both the oxidation reaction and the reduction reaction influenced under strain. Related efforts can be dedicated to resolve this ambiguity.

As for the influence of strain on pitting corrosion, it was discovered that surface defects lead to the first stable pitting event at a decreased pitting potential upon the cyclic-polarization. It remains a question whether surface defects due to prior plastic deformation increase the number of pit-initiation sites. The potential relationship between the number of pit-initiation sites and the concentration of surface defects needs to be explored. A stable pit creates an extremely small anode/cathode ratio, which makes the rest of the exposed surface act as a cathode. An experiment can be designed to maintain all pitting events metastable, so that individual pitting events can experience less interferences from others. Statistical analyses can be made based on geometry and density of the metastable pits.

Breakdown of the passive film occurs through generation of slip-lines or simply film rupture upon plastic deformation. The passive film would tend to reform, however pitting phenomena could be stimulated by this sudden exposure of bare metal into exterior aqueous environments. By applying an appropriate combination of potentials and environments, the competition between film-reformation and pit-initiation could be manifested. This set of hypothesized experiment can resemble a situation where the passive film constantly breaks down due to plastic straining and potentially leads to more severe pitting attacks.

Furthermore, micro-strain due to plastic deformation can cause localized galvanic polarization or facilitate localized anodic/cathodic reactions. Given appropriate conditions, it can cause local preferential dissolution or pre-mature localized corrosion. This will require mapping local electrochemical activities to some precisely designed microstructures with micro-strain features using micro-electrochemical techniques, such as scanning vibrating electrode technique (SVET) and Scanning electrochemical microscopy (SECM). In this way, the effect of micro-strain on different corrosion reactions can be studied.

APPEDIX A MATLAB PROGRAM FOR SIMULATING FILM-REPASSIVATION BEHAVIOR

```
function theta_n( file)

data = importdata (file);

t1=1;

t2=47;

t=data(t1:t2,1)';

%t_initial=t(1);

%t=t-t_initial.*ones(1,t2-t1+1);

%t(1)=10^(-80);

c_d=data(t1:t2,2)'/0.7854;

I_bare=c_d(1);

fun=@(a,t)exp(-a(1).*t.^a(4)).*I_bare+(ones(1,t2-t1+1)-exp(-a(1).*t.^a(4))).*a(2).*t.^(-a(3));

a0=[100.0000   0    0.484   1];

options = optimset('Display','off');
```

```
a=lsqcurvefit(fun,a0,t,c_d,[],[],options);%a1=k,a2=A,a3=b;

R_square=0;

previous_R=1;

d=1;

while d~=0%R_square<0.95

a0=a;

a=lsqcurvefit(fun,a0,t,c_d)

c_d_expect=exp(-a(1).*t.^a(4)).*I_bare+(ones(1,t2-t1+1)-exp(-a(1).*t.^a(4))).*a(2).*t.^(-a(3));

c_d_average=mean(c_d);

SST=sum((c_d-c_d_average).^2);

SSR=sum((c_d-c_d_expect).^2);

R_square=1-SSR/SST

d=R_square-previous_R;

previous_R=R_square;

end
```

REFERENCES

1. Peguet, L., B. Malki, and B. Baroux, *Effect of austenite stability on the pitting corrosion resistance of cold worked stainless steels.* Corrosion Science, 2009. **51**(3): p. 493-498.

2. Lv, J. and H. Luo, *Effects of strain and strain-induced α'-martensite on passive films in AISI 304 austenitic stainless steel.* Materials Science and Engineering: C, 2014. **34**: p. 484-490.

3. Ravi Kumar, B., B. Mahato, and R. Singh, *Influence of Cold-Worked Structure on Electrochemical Properties of Austenitic Stainless Steels.* Metallurgical and Materials Transactions A, 2007. **38**(9): p. 2085-2094.

4. *Green Source Energy LLC. Patent Issued for Inhibiting Corrosion and Scaling of Surfaces Contacted by Sulfur-Containing Materials*. 2012: Atlanta. p. 1412.

5. De Wit, F.M., et al., *The Influence of Chemical Pre-treatment and Magnesium Surface Enrichment on Bonding of Succinic Acid Molecules to Aluminium Alloy.* Journal of Adhesion Science and Technology, 2008. **22**(10-11): p. 1089-1104.

6. Feliu, S., et al., *The effect of low temperature heat treatment on surface chemistry and corrosion resistance of commercial magnesium alloys AZ31 and AZ61 in 0.6 M NaCl solution.* Corrosion Science, 2014. **80**(C): p. 461-472.

7. Ghali, E., *Corrosion resistance of aluminum and magnesium alloys understanding, performance, and testing*, ed. R.W. Revie. 2010, Hoboken, N.J.: Hoboken, N.J. : John Wiley.

8. Meinhardt, C.P., et al., *Hydrogen embrittlement under cathodic protection of friction stir welded UNS S32760 super duplex stainless steel.* Materials Science & Engineering A, 2017. **706**: p. 48-56.

9. da Silva, B.R.S., F. Salvio, and D.S.d. Santos, *Hydrogen induced stress cracking in UNS S32750 super duplex stainless steel tube weld joint.* International Journal of Hydrogen Energy, 2015. **40**(47): p. 17091-17101.

10. Chou, S.-L. and W.-T. Tsai, *Effect of grain size on the hydrogen-assisted cracking in duplex stainless steels.* Materials Science and Engineering: A, 1999. **270**(2): p. 219-224.

11. Turnbull, A. and R.B. Hutchings, *Analysis of hydrogen atom transport in a two-phase alloy.* Materials Science and Engineering: A, 1994. **177**(1): p. 161-171.

12. Olden, V., et al., *Influence of hydrogen from cathodic protection on the fracture susceptibility of 25%Cr duplex stainless steel – Constant load SENT testing and FE-modelling using hydrogen influenced cohesive zone elements.* Engineering Fracture Mechanics, 2009. **76**(7): p. 827-844.

13. Gutman, E.M., *Mechanochemistry of Materials*. 1998, Cambridge: Cambridge International Science Publishing.

14. Feliu, S. and G. Castro, *A method of obtaining etch spirals and their relation with dislocations in silicon iron.* Acta Metallurgica, 1962. **10**(5): p. 543-549.

15. Jones, D.A., *Principles and prevention of corrosion*. 2nd ed.. ed. Corrosion. 1996, Upper Saddle River, NJ: Upper Saddle River, NJ : Prentice Hall.

16. Johnston, H.A., *Effect of Strain on Corrosion Rates of Copper in Sulfuric Acid Solutions*, in *Chemical Engineering*. 1955, University of British Columbia.

17. Shen, Y., et al., *Twinning and martensite in a 304 austenitic stainless steel.* Materials Science and Engineering. A. Structural Materials: Properties, Microstructure and Processing, 2012. **552**(C).

18. Lee, W.-S. and C.-F. Lin, *Comparative study of the impact response and microstructure of 304L stainless steel with and without prestrain.* Metallurgical and Materials Transactions A, 2002. **33**(9): p. 2801-2810.

19. Staudhammer, K.P. and L.E. Murr, *The effect of prior deformation on the residual microstructure of explosively deformed stainless steels.* Materials Science and Engineering, 1980. **44**(1): p. 97-113.

20. Suzuki, T., et al., *An experimental study of the martensite nucleation and growth in 18/8 stainless steel.* Acta Metallurgica, 1977. **25**(10): p. 1151-1162.

21. Brooks, J.W., M.H. Loretto, and R.E. Smallman, *In situ observations of the formation of martensite in stainless steel.* Acta Metallurgica, 1979. **27**(12): p. 1829-1838.

22. Olson, G. and M. Cohen, *Kinetics of strain-induced martensitic nucleation.* Metallurgical Transactions A, 1975. **6**(4): p. 791-795.

23. Choi, J.-Y. and W. Jin, *Strain induced martensite formation and its effect on strain hardening behavior in the cold drawn 304 austenitic stainless steels.* Scripta Materialia, 1997. **36**(1): p. 99-104.

24. Beavers, J., *2013 Frank Newman Speller Award Lecture: Integrity Management of Natural Gas and Petroleum Pipelines Subject to Stress Corrosion Cracking.* Corrosion, 2014. **70**(1): p. 3-18.

25. Parkins, R.N., W.K. Blanchard, Jr., and B.S. Delanty, *Transgranular Stress Corrosion Cracking of High-Pressure Pipelines in Contact with Solutions of Near Neutral pH.* Corrosion, 1994. **50**(05): p. 17.

26. Huang, Y., et al., *Effects of hydrogen and surface dislocation on active dissolution of deformed 304 austenitic stainless steel in acid chloride solution.* Materials Science and Engineering: A, 2011. **528**(3): p. 1882-1888.

27. Tang, X. and Y.F. Cheng, *Quantitative characterization by micro-electrochemical measurements of the synergism of hydrogen, stress and dissolution on near-neutral pH stress corrosion cracking of pipelines.* Corrosion Science, 2011. **53**(9): p. 2927-2933.

28. Yang, Y. and Y. Cheng, *Stress Enhanced Corrosion at the Tip of Near-Neutral pH Stress Corrosion Cracks on Pipelines.* Corrosion, 2016. **72**(8): p. 1035-1043.

29. Yaguchi, S. and T. Yonezawa, *Intergranular Stress Corrosion Cracking growth perpendicular to fatigue pre-cracks in T–L oriented compact tension specimens in simulated Pressurized Water Reactor primary water.* Corrosion Science, 2014. **86**.

30. Kuo, C.H., et al., *The Effect of Lattice Strain on the Catalytic Properties of Pd Nanocrystals.* ChemSusChem, 2013. **6**(10): p. 1993-2000.

31. Mavrikakis, M., B. Hammer, and J.K. Nørskov, *Effect of Strain on the Reactivity of Metal Surfaces.* Physical Review Letters, 1998. **81**(13): p. 2819-2822.

32. Yan, K., et al., *The Influence of Elastic Strain on Catalytic Activity in the Hydrogen Evolution Reaction.* Angewandte Chemie International Edition, 2016. **55**(21): p. 6175-6181.

33. G. S. Frankel, T.L., and J. R. Scullyb, *Localized Corrosion: Passive Film Breakdown vs Pit Growth Stability.* The Electrochemical Society, 2017. **164**(4): p. 2.

34. Yang, W.P., D. Costa, and P. Marcus, *Resistance to pitting and chemical composition of passive films of a Fe-17%Cr alloy in chloride-containing acid solution.* Journal of the Electrochemical Society, 1994. **141**(10).

35. Wegrelius, L., F. Falkenberg, and I. Olefjord, *Passivation of stainless steels in hydrochloric acid.* Journal of the Electrochemical Society, 1999. **146**(4): p. 1397-1406.

36. Natishan, P.M., W.E. O`Grady, and E. McCafferty, *Chloride uptake by oxide covered aluminum as determined by X-ray photoelectron and X-ray absorption spectroscopy.* Journal of the Electrochemical Society, 1999. **146**(5): p. 1737-1740.

37. S. Y. Yu, W.E.O.G., D. E. Ramaker and P. M. Natishan, *Chloride Ingress into Aluminum Prior to Pitting Corrosion An Investigation by XANES and XPS.* The Electrochemical Society, 2000. **147**(8): p. 7.

38. Hazza, M.I. and M.E. El-Dahshan, *The effect of molybdenum on the corrosion behaviour of some steel alloys.* Desalination, 1994. **95**(2): p. 199-209.

39. Olsson, C.O.A. and D. Landolt, *Passive films on stainless steels—chemistry, structure and growth.* Electrochimica Acta, 2003. **48**(9): p. 1093-1104.

40. Jargelius-Pettersson, R.F.A., *Examination of the role of molybdenum in passivation of stainless steels using ac impedance spectroscopy.* Journal of the Electrochemical Society, 1998. **145**(5): p. 1462-1468.

41. Olsson, C.-O.A., *The influence of nitrogen and molybdenum on passive films formed on the austenoferritic stainless steel 2205 studied by AES and XPS.* Corrosion Science, 1995. **37**(3): p. 467-479.

42. Olsson, C.-O.A. and S.E. Hörnström, *An AES and XPS study of the high alloy austenitic stainless steel 254 SMO® tested in a ferric chloride solution.* Corrosion Science, 1994. **36**(1): p. 141-151.

43. Olsson, C.O.A., H.J. Mathieu, and D. Landolt, *Angle-resolved XPS analysis of molybdenum and tungsten in passive films on stainless steel PVD alloys.* Surface and Interface Analysis, 2002. **34**(1): p. 130-134.

44. Willenbruch, R.D., et al., *An XPS and electrochemical study of the influence of molybdenum and nitrogen on the passivity of austenitic stainless steel.* Corrosion Science, 1990. **31**: p. 179-190.

45. Clayton, C.R. and Y.C. Lu, *A bipolar model of the passivity of stainless steels—III. The mechanism of MoO 4 2− formation and incorporation.* Corrosion Science, 1989. **29**(7): p. 881-898.

46. Lu, Y.C., C.R. Clayton, and A.R. Brooks, *A bipolar model of the passivity of stainless steels—II. The influence of aqueous molybdate.* Corrosion Science, 1989. **29**(7): p. 863-880.

47. Lu, Y.C. and C.R. Clayton, *An XPS study of the passive and transpassive behavior of molybdenum in deaerated 0.1 M HCl.* Corrosion Science, 1989. **29**(8): p. 927-937.

48. Lu, Y.C., M.B. Ives, and C.R. Clayton, *Synergism of alloying elements and pitting corrosion resistance of stainless steels.* Corrosion Science, 1993. **35**(1): p. 89-96.

49. Halada, G.P., D. Kim, and C.R. Clayton, *Influence of nitrogen on electrochemical passivation of high-nickel stainless steels and thin molybdenum-nickel films.* Corrosion, 1996. **52**(1): p. 36-46.

50. Willenbruch, R.D., et al., *An XPS and electrochemical study of the influence of molybdenum and nitrogen on the passivity of austenitic stainless steel.* Corrosion Science, 1990. **31**(C): p. 179-190.

51. Bayoumi, F.M. and W.A. Ghanem, *Effect of nitrogen on the corrosion behavior of austenitic stainless steel in chloride solutions.* Materials Letters, 2005. **59**(26): p. 3311-3314.

52. Anwar, M.S., S. Prifiharni, and E. Mabruri, *The effect of tempering temperature on pitting corrosion resistance of 420 stainless steels*. 2016.

53. Li, J., et al., *Effect of microstructure on the corrosion resistance of 2205 duplex stainless steel. Part 1: Microstructure evolution during isothermal aging at 850 °C and evaluation of anticorrosion properties by methods of cyclic potentiodynamic polarization and*

electrochemical impedance tests. Construction and Building Materials, 2018. **189**: p. 1286-1293.

54. Yang, Y.H., et al., *The influence of solution treatment temperature on microstructure and corrosion behavior of high temperature ageing in 25% Cr duplex stainless steel.* Journal of Alloys and Compounds, 2011. **509**(36): p. 8870-8879.

55. Gao, J., et al., *Investigation of selective corrosion resistance of aged lean duplex stainless steel 2101 by non-destructive electrochemical techniques.* Electrochimica Acta, 2009. **54**(24): p. 5830-5835.

56. Deng, B., et al., *Evaluation of localized corrosion in duplex stainless steel aged at 850°C with critical pitting temperature measurement.* Electrochimica Acta, 2009. **54**(10): p. 2790-2794.

57. Raj, V., et al., *Pulse Anodizing—An Overview.* Transactions of the IMF, 2003. **81**(4): p. 114-121.

58. McBee, C.L. and J. Kruger, *Nature of passive films on iron-chromium alloys.* Electrochimica Acta, 1972. **17**(8): p. 1337-1341.

59. Ryan, M.P., R.C. Newman, and G.E. Thompson, *Atomically resolved STM of oxide film structures on Fe-Cr alloys during passivation in sulfuric acid solution.* Journal of the Electrochemical Society, 1994. **141**(12).

60. Ryan, M.P., R.C. Newman, and G.E. Thompson, *An STM study of the passive film formed on iron in borate buffer solution.* Journal of the Electrochemical Society, 1995. **142**(10).

61. Macdonald, D.D., *The history of the Point Defect Model for the passive state: A brief review of film growth aspects.* Electrochimica Acta, 2011. **56**(4): p. 1761-1772.

62. Macdonald, D., and George Englehardt, *The Point Defect Model for Bi-Layer Passive Films.* ECS Trans, 2010. **28**(24): p. 22.

63. Deyab, M.A. and S.T. Keera, *Cyclic voltammetric studies of carbon steel corrosion in chloride-formation water solution and effect of some inorganic salts.* Egyptian Journal of Petroleum, 2012. **21**(1): p. 31-36.

64. Wang, Y., et al., *Effects of strain on the corrosion behaviour of X80 steel.* Corrosion Science, 2011. **53**(9): p. 2761-2766.

65. Wang, X., et al., *Synergistic effect of stray current and stress on corrosion of API X65 steel.* Journal of Natural Gas Science and Engineering, 2014. **21**: p. 474-480.

66. Feng, X., et al., *The passive behaviour of 304 stainless steels in saturated calcium hydroxide solution under different deformation.* Corrosion Science, 2014. **82**(C): p. 347-355.

67. Takakuwa, O., and Hitoshi Soyama, *Effect of Residual Stress on the Corrosion Behavior of Austenitic Stainless Steel.* Advances in Chemical Engineering and Science, 2015. **5**(1): p. 10.

68. Lv, J., W. Guo, and T. Liang, *The effect of pre-deformation on corrosion resistance of the passive film formed on 2205 duplex stainless steel.* Journal of Alloys and Compounds, 2016. **686**: p. 176-183.

69. Lee, J.-B. and S.-I. Yoon, *Effect of nitrogen alloying on the semiconducting properties of passive films and metastable pitting susceptibility of 316L and 316LN stainless steels.* Materials Chemistry and Physics, 2010. **122**(1): p. 194-199.

70. Jinlong, L., et al., *The passive film characteristics of several plastic deformation 2099 Al–Li alloy.* Journal of Alloys and Compounds, 2016. **662**: p. 143-149.

71. Benoit, M., et al., *Comparison of different methods for measuring the passive film thickness on metals.* Electrochimica Acta, 2016. **201**: p. 340-347.

72. Mohammadi, F., et al., *EIS study of potentiostatically formed passive film on 304 stainless steel.* Electrochimica Acta, 2011. **56**(24): p. 8727-8733.

73. Lou, X., *Stress corrosion cracking and corrosion of carbon steel in simulated fuel-grade ethanol*, S. Materials and Engineering, Editors. 2011, Georgia Institute of Technology.

74. Vignal, V., H. Krawiec, and S. Manchet, *Influence of surface preparation and microstructure on the passivity and corrosion behaviour of duplex stainless steels.* Journal of Solid State Electrochemistry, 2014. **18**(11): p. 2947-2954.

75. Haupt, S. and H.H. Strehblow, *A combined surface analytical and electrochemical study of the formation of passive layers on Fe Cr alloys in 0.5 M H 2SO 4.* Corrosion Science, 1995. **37**(1): p. 43-54.

76. Tong E. Pou, O.J.M., Vaneica Young, John O'M. Bockris and Luis L. Tongson and *Passive Films on Iron: The Mechanism of Breakdown in Chloride Containing Solutions.* The Electrochemical Society, 1984. **131**(6): p. 9.

77. Evans, U.R., *CXL.—The passivity of metals. Part I. The isolation of the protective film.* Journal of the Chemical Society (Resumed), 1927. **0**(0): p. 1020-1040.

78. Hoar, T.P., D.C. Mears, and G.P. Rothwell, *The relationships between anodic passivity, brightening and pitting.* Corrosion Science, 1965. **5**(4): p. 279-289.

79. Blake, R.E. and L.M. Walter, *Kinetics of feldspar and quartz dissolution at 70–80°C and near-neutral pH: effects of organic acids and NaCl.* Geochimica et Cosmochimica Acta, 1999. **63**(13): p. 2043-2059.

80. K. E. Heusler, L.F., *Kinetics of Pit Initiation at the Alloy Fe5Cr.* Materials and Corrosion, 1976. **27**(11): p. 4.

81. Sazou, D., M. Pagitsas, and C. Georgolios, *The influence of chloride ions on the dynamic characteristics observed at the transition between corrosion and passivation states of an iron electrode in sulphuric acid solutions.* Electrochimica Acta, 1992. **37**(11): p. 2067-2076.

82. Haupt, S. and H.H. Strehblow, *The formation of the passive layer on Cr in 0.5 M H 2SO 4 A combined electrochemical and surface analytical study.* Journal of Electroanalytical Chemistry, 1987. **228**(1): p. 365-392.

83. Hoppe, H.W., S. Haupt, and H.H. Strehblow, *Combined surface analytical and electrochemical study of the formation of passive layers on Fe/Cr alloys in 1 M NaOH.* Surface and Interface Analysis, 1994. **21**(8): p. 514-525.

84. Keddam, M., et al., *Depassivation of iron by straining and by abrasion: an A.C. impedance study.* Corrosion Science, 1983. **23**(4): p. 441-451.

85. Raja, V.S., *Stress corrosion cracking theory and practice*. Woodhead Publishing Series in Metals and Surface Engineering, ed. V.S. Raja and T. Shoji. 2011, Oxford

Philadelphia: Oxford

Philadelphia : Woodhead Pub.

86. Engseth, P. and J.C. Scully, *Repassivation studies on an austenitic stainless steel in chloride solutions.* Corrosion Science, 1975. **15**(6): p. 505-519.

87. Kwon, H.S., E.A. Cho, and K.A. Yeom, *Prediction of stress corrosion cracking susceptibility of stainless steels based on repassivation kinetics.* Corrosion, 2000. **56**(1).

88. Ford, T.P.H.a.F.P., *Electrode Reaction Rates on Straining Aluminum-Magnesium Wires in Chloride and Sulfate Solutions.* The Electrochemical Society, 1973. **120**(8): p. 7.

89. Wang, Y., et al., *Effect of Thiosulfate on Metastable Pitting of 304L and S32101 in Chloride- and Thiosulfate-Containing Environment.* Corrosion (Houston), 2016. **72**(5): p. 628-628.

90. Wang, Y. and P. Singh, *Corrosion Behavior of Austenitic and Duplex Stainless Steels in Thiosulfate- and Chloride-Containing Environments.* Corrosion (Houston), 2015. **71**(8): p. 937-944.

91. Frankel, G.S., *Pitting corrosion of metals: A review of the critical factors.* Journal of the Electrochemical Society, 1998. **145**(6): p. 2186-2197.

92. Laycock, N.J., *Effects of temperature and thiosulfate on chloride pitting of austenitic stainless steels.* Corrosion, 1999. **55**(6).

93. Kolotyrkin, Y.M., *Pitting corrosion of metals.* Corrosion, 1963. **19**(8): p. 8.

94. Hoar, T.P. and W.R. Jacob, *Breakdown of Passivity of Stainless Steel by Halide Ions.* Nature, 1967. **216**(5122): p. 1299.

95. W. Khalil, S.H., H. Strehblow, *The thinning of the passive layer on iron by halides.* Materials and Corrosion, 1985. **36**(1): p. 6.

96. Hanninen, H., Cullen, W. and Kemppainen, M.Corrosion, *Effects of MnS inclusion dissolution on environmentally assisted cracking in low-alloy and carbon steels.* International Journal of Fatigue, 1991. **13**(2): p. 182-182.

97. Chiba, A., et al., *Effect of atmospheric aging on dissolution of MnS inclusions and pitting initiation process in type 304 stainless steel.* Corrosion Science, 2016. **106**: p. 25-34.

98. Soon-Hyeok Jeon, S.-T.K., Jun-Seob Lee, In-Sung Lee, Yong-Soo Park, *Effects of Sulfur Addition on the Formation of Inclusions and the Corrosion Behavior of Super Duplex Stainless Steels in Chloride Solutions of Different PH.* Materials Transactions, 2012. **52**(9): p. 10.

99. Jun, J., K. Holguin, and G.S. Frankel, *Pitting Corrosion of Very Clean Type 304 Stainless Steel.* Corrosion, 2014. **70**(2): p. 146-155.

100. Alexander Hincapie Ramirez, C.H.R.a.I.C., *Cold Rolling Effect on the Microstructure and Pitting Resistance of the NBR ISO 5832-1 Austenitic Stainless Steel.* ELECTROCHEMICAL SCIENCE, 2013. **8**(12): p. 12801-12815.

101. Yang, J., Q. Wang, and K. Guan, *Effect of stress and strain on corrosion resistance of duplex stainless steel.* International Journal of Pressure Vessels and Piping, 2013. **110**: p. 72-76.

102. Kim, K.M., et al., *Effect of plastic deformation on the corrosion resistance of ferritic stainless steel as a bipolar plate for polymer electrolyte membrane fuel cells.* International Journal of Hydrogen Energy, 2012. **37**(10): p. 8459-8464.

103. Liu, J., *Deformation induced martensitic transformation in 304 stainless steels*, D. Kaoumi and T. Besmann, Editors. 2016, ProQuest Dissertations Publishing.

104. Peguet, L., B. Malki, and B. Baroux, *Influence of cold working on the pitting corrosion resistance of stainless steels.* Corrosion Science, 2007. **49**(4): p. 1933-1948.

105. Nickerson, W.C., et al., *Modeling galvanic coupling and localized damage initiation in airframe structures.* Corrosion Reviews, 2017. **35**(4-5): p. 205-223.

106. I. M. GHAYAD, A.S.H., N.N. GIRGIS AND W. GHANEM, *Effect of cold working on the aging and corrosion behaviour of Fe-Mn-Al stainless steel.* Steel Grips, 2006. **4**(2): p. 133-137.

107. Ernst, P., et al., *The mechanism of lacy cover formation in pitting.* Corrosion Science, 1997. **39**(6): p. 1133-1136.

108. G.S. Frankel, L.S., F. Hunkeler and H. Böhni, *Metastable pitting of stainless steel.* Corrosion, 1987. **43**: p. 429-436.

109. D.E. Williams, J.S., P.H. Balkwill, in: G.S. Frankel, R.C. Newman (Eds.), *Critical Factors in Localized Corrosion.* The Electrochemical Society, 1992: p. 36-44.

110. Feng, X., et al., *The effect of deformation on metastable pitting of 304 stainless steel in chloride contaminated concrete pore solution.* Corrosion Science, 2016. **103**: p. 223-229.

111. Alkire, R.C. and K.P. Wong, *The corrosion of single pits on stainless steel in acidic chloride solution.* Corrosion Science, 1988. **28**(4): p. 411,415-413,421.

112. Pistorius, P.C. and G.T. Burstein, *Metastable Pitting Corrosion of Stainless Steel and the Transition to Stability.* Philosophical Transactions: Physical Sciences and Engineering, 1992. **341**(1662): p. 531-559.

113. Soltis, J., *Passivity breakdown, pit initiation and propagation of pits in metallic materials – Review.* Corrosion Science, 2015. **90**(C): p. 5-22.

114. Laycock, N.J. and R.C. Newman, *Localised dissolution kinetics, salt films and pitting potentials.* Corrosion Science, 1997. **39**(10): p. 1771-1790.

115. Hoar, T.P., *The corrosion of tin in nearly neutral solutions.* Transactions of the Faraday Society, 1937. **33**: p. 1152-1167.

116. Frankenthal, H.W.P.a.R.P., *On the Mechanism of Localized Corrosion of Iron and Stainless Steel: I . Electrochemical Studies.* The Electrochemical Society, 1972. **119**(10): p. 1297-1304

117. Pickering, R.P.F.a.H.W., *On the Mechanism of Localized Corrosion of Iron and Stainless Steel: II . Morphological Studies.* The Electrochemical Society, 1972. **199**(10): p. 1304-1310

118. Galvele, J.R., *Transport Processes and the Mechanism of Pitting of Metals.* The Electrochemical Society, 1976. **123**(4): p. 464-474.

119. Sehgal, A., et al., *Pit growth study in Al alloys by the foil penetration technique.* Journal of the Electrochemical Society, 2000. **147**(1).

120. Gaudet, G.T., et al., *Mass transfer and electrochemical kinetic interactions in localized pitting corrosion.* AIChE Journal, 1986. **32**(6): p. 949-958.

121. Isaacs, R.C.N.a.H.S., *Diffusion-Coupled Active Dissolution in the Localized Corrosion of Stainless Steels.* The Electrochemical Society, 1983. **130**(7): p. 1621-1624

122. Ramgopal, T. and G. Frankel, *Role of alloying additions on the dissolution kinetics of aluminum binary alloys using artificial crevice electrodes.* Corrosion, 2001. **57**(8): p. 702.

123. Newman, R.C., et al., *An experimental confirmation of the pitting potential model of galvele.* Corrosion Science, 1988. **28**(5): p. 471-477.

124. Hunkeler, F., et al, *Technical Note:On the Mechanism of Localized Corrosion.* Corrosion (Houston), 1987. **43**(7): p. 429–436.

125. Frankel, G.S., *The growth of 2-D pits in thin film aluminum.* Corrosion Science, 1990. **30**(12): p. 1203-1218.

126. Alkire, T.R.B.a.R.C., *Occurrence of Salt Films during Initiation and Growth of Corrosion Pits.* The Electrochemical Society, 1979. **126**(10): p. 1662-1666.

127. Rosenfeld, I.L. and I.S. Danilov, *Electrochemical aspects of pitting corrosion.* Corrosion Science, 1967. **7**(3): p. 129,IN1,133-132,IN3,142.

128. Ke, R. and R. Alkire, *Initiation of corrosion pits at inclusions on 304 stainless steel.* Journal of the Electrochemical Society, 1995. **142**(12): p. 4056-4062.

129. Williams, D., C. Westcott, and M. Fleishmann, *Stochastic models of pitting corrosion of stainless steels. I. Modeling of the initiation and growth of pits at constant potential.* Journal of the Electrochemical Society, 1985. **132**(8): p. 1796-1803.

130. P.H. Balkwill, C.W., D.E. Williams, *Stochastic approach to the initiation of pitting corrosion.* Materials and Corrosion Forum 44-45, 1989: p. 299–312.

131. T. SHIBATA, T.T., *Stochastic Theory of Pitting Corrosion.* Corrosion (Houston), 1977. **33**(7): p. 243-251.

132. Williams, D.E., J. Stewart, and P.H. Balkwill, *The nucleation, growth and stability of micropits in stainless steel.* Corrosion Science, 1994. **36**(7): p. 1213-1235.

133. Shibata, T., *Stochastic Approach to the Effect of Alloying Elements on the Pitting Resistance of Ferritic Stainless Steeles.* Transactions of the Iron and Steel Institute of Japan, 1983. **23**(9): p. 785-788.

134. Pistorius, P.C. and G.T. Burstein, *Aspects of the effects of electrolyte composition on the occurrence of metastable pitting on stainless steel.* Corrosion Science, 1994. **36**(3): p. 525-538.

135. Pride, S.T., J.R. Scully, and J.L. Hudson, *Metastable pitting of aluminum and criteria for the transition to stable pit growth.* Journal of the Electrochemical Society, 1994. **141**(11).

136. Burstein, G.T. and R.M. Souto, *Observations of localised instability of passive titanium in chloride solution.* Electrochimica Acta, 1995. **40**(12): p. 1881-1888.

137. Burstein, G.T., P.C. Pistorius, and S.P. Mattin, *The nucleation and growth of corrosion pits on stainless steel.* Corrosion Science, 1993. **35**(1): p. 57-62.

138. Tian, W., et al., *Metastable pitting corrosion of 304 stainless steel in 3.5% NaCl solution.* Corrosion Science, 2014. **85**(C): p. 372-379.

139. Barbucci, A., et al., *Electrochemical and corrosion behaviour of cold rolled AISI 301 in 1 M H 2SO 4.* Journal of Alloys and Compounds, 2001. **317**(318): p. 607-611.

140. Barbucci, A., G. Cerisola, and P.L. Cabot, *Effect of Cold-Working in the Passive Behavior of 304 Stainless Steel in Sulfate Media.* Journal of The Electrochemical Society, 2002. **149**(12): p. B534-B542.

141. Kamachi Mudali, U., et al., *On the pitting corrosion resistance of nitrogen alloyed cold worked austenitic stainless steels.* Corrosion Science, 2002. **44**(10): p. 2183-2198.

142. Krawczyk, B., et al., *Corrosion Behavior of Cold Rolled Type 316L Stainless Steel in HCl-Containing Environments.* Corrosion, 2017. **73**(11): p. 1346-1358.

143. Zhao, Y., et al., *Effects of plastic straining on the corrosion resistance of TRIP-aided lean duplex stainless steels.* Journal of Materials Science, 2018. **53**(12): p. 9258-9272.

144. Lillard, R.S., G. Vasquez, and D.F. Bahr, *The Kinetics of Anodic Dissolution and Repassivation on Stainless Steel 304L in Solutions Containing Nitrate.* Journal of The Electrochemical Society, 2011. **158**(6): p. C194-C201.

145. Wang, Y., *Effect of Thiosulfate on Passivity and Corrosion Properties of Stainless Steels*, S. Materials, et al., Editors. 2016, Georgia Institute of Technology.

146. Voort, G., *Color Metallography.* Industrial Heating, 2012. **80**(8): p. 53-56.

147. Prevéy, P.S., *X-RAY DIFFRACTION RESIDUAL STRESS TECHNIQUES.*

148. Jinlong, L. and L. Hongyun, *Electrochemical investigation of passive film in pre-deformation AISI 304 stainless steels.* Applied Surface Science, 2012. **263**: p. 29-37.

149. Ratzer-Scheibe, V.H.J., and Buhl, H, *Zum Repassivierungsverhalten Metallischer Werkstqffc, am Beispiel einer Titanlegierung.* Korros, 1979. **30**: p. 846-853.

150. *Stress Concentrations at Holes.* http://www.fracturemechanics.org/hole.html.